
DNA Nanorobots: Directed Molecular Transport and *In Silico* Studies of a Molecular Torsion Spring

Matthias Gouder

Master's thesis



Faculty of Physics

DNA Nanorobots: Directed Molecular Transport and *In Silico* Studies of a Molecular Torsion Spring

Master's thesis

submitted on

25 October 2021

by

Matthias Gouder

born on 26 March 1998 in Karlsruhe

supervised by

Prof. Dr. Joachim Rädler

Soft Condensed Matter

Faculty of Physics

Ludwig-Maximilian-University of Munich

and

Prof. Dr. Friedrich Simmel

Physics of Synthetic Biological Systems - E14

Department of Physics

Technical University of Munich

DNA Nanoroboter: Gerichteter, molekularer Transport und *in silico* Untersuchungen einer molekularen Torsionsfeder

Masterarbeit

vorgelegt am

25. Oktober 2021

von

Matthias Gouder

geboren am 26. März 1998 in Karlsruhe

betreut von

Prof. Dr. Joachim Rädler

Weiche kondensierte Materie

Fakultät für Physik

Ludwig-Maximilian-Universität München

und

Prof. Dr. Friedrich Simmel

Physik synthetischer Biosysteme - E14

Fakultät für Physik

Technische Universität München

Contents

Abstract	vii
1. Introduction	1
2. Biophysical Background	3
2.1. Deoxyribonucleic acid (DNA)	3
2.1.1. Molecular Structure	3
2.1.2. Buffers	5
2.2. Rupture of dsDNA	6
2.3. Transportation mechanism of Single-Molecule-Cargo	8
2.4. DNA nanotechnology	9
2.4.1. Elementary Structures	9
2.4.2. DNA-Origami	11
2.5. Roboarm	13
2.6. Fluorescence	15
2.7. Chemical kinetics	16
2.8. oxDNA - a coarse grained MD simulation engine	18
2.8.1. The Model	18
2.8.2. Thermostat	19
2.8.3. External forces	19
2.8.4. Relaxation in oxDNA	19
3. Simulation of Joint	21
3.1. Simulation Setup	21
3.1.1. Miniaturized Structure	21
3.1.2. Rotating Driving Forces	22
3.1.3. Overview of Joint Variations	25
3.1.4. Relaxation of Joint Variations	26
3.1.5. Theoretical Dynamics of Skipping	26
3.1.6. Simulation Parameters	26
3.1.7. Simulations Types	28
3.2. Results	28
3.2.1. Windup with constant rotating traps	28
3.2.2. Windup with different rate for 3nt joint	38
3.2.3. Unwind of 13nt joint	40

Contents

3.3. Discussion	41
3.3.1. Range of Motion	41
3.3.2. Comparing to real-world	42
3.3.3. First Skip Linearity	43
3.3.4. Skipping Phase	43
3.3.5. Forces/Distances	44
3.3.6. Energy Storage	45
3.4. Conclusion	45
4. Simulation of the Pickup-Process	47
4.1. Simulation Setup	47
4.1.1. Parent structure	47
4.1.2. Parallelization (single/multi class)	51
4.2. Results	52
4.2.1. Dynamics of single structure rupture	52
4.2.2. Force screening	53
4.2.3. Length Dependence	54
4.2.4. Isolated versus competing rupture comparison	56
4.3. Discussion	58
4.3.1. Delayed Rupture	58
4.3.2. Rupture Rates	58
4.4. Conclusion	59
5. Experimental Part	61
5.1. Experimental methods	61
5.1.1. DNA Origami Fabrication	61
5.1.2. Monitoring of molecular transport experiments with single molecular TIRF microscopy	63
5.1.3. PAINT image processing routine	67
5.2. Structural Design of the Cargo Transport System	68
5.2.1. Deposit- and Target-Handles	68
5.2.2. Pickup-Handle	70
5.2.3. Marker	70
5.3. Cargo Loading- and Transporting-Protocol	72
5.3.1. Post-Blocking-Cargo-Loading	74
5.3.2. Pre-Blocking-Cargo-Loading	75
5.3.3. Bulk loading	78
5.3.4. Visualization Domains	78
5.3.5. Cargo Transporting Protocol	79
5.4. Attempts of Cargo-Transport	80
5.4.1. Cargo transport experiments (pointer tracking)	80
5.4.2. Cargo transport experiments (cargo tracking)	84
5.5. Conclusion	87
5.6. Outlook	87

6. Conclusion	91
A. Appendix	93
A.1. Radial- and tangential component of rotating harmonic traps	93
A.2. Sample oxDNA Input File	94
A.3. Buffers	95
A.4. Sequences	95
Bibliography	97

List of Figures

1.1. Exemplary DNA-Origami Nanostructures	2
2.1. Chemical Structure of DNA	4
2.2. Representations of DNA	5
2.3. Rupture Overview	6
2.4. Free Energy at Rupture	7
2.5. Transport Mechanism	9
2.6. Toehold Mediated Strand Displacement	10
2.7. Holliday Junction	11
2.8. Folding Process	13
2.9. Roboarm Structure	14
2.10. Pointer Comparison	15
2.11. oxDNA2 Model	18
3.1. Miniaturized Roboarm Structure	22
3.2. Comparing driving forces	24
3.3. Different Joints	25
3.4. Skipping	27
3.5. Trajectories of Cumulative Angle	30
3.6. Phase at Skipping	31
3.7. Backbone Force in oxDNA	32
3.8. Internucleotide-interaction of Spring-Domain	35
3.9. Internal Energy	36
3.9. Internal Energy	37
3.10. Energy Storage	39
3.11. Twist at different rates	39
3.12. Trajectories of untwist simulation	40
3.13. Backbone forces for untwist simulation	41
4.1. Parent structure	48
4.2. Biased Random Walk	50
4.3. Isolated Rupture Structure	51
4.4. Multi-class parallelization	52
4.5. Dynamic inter-nucleotide distances during rupture	53
4.6. Fit Force Screening	55
4.7. Length Dependence	56

List of Figures

4.8. Isolated vs Competing Rupture	57
5.1. TIRFM	64
5.2. Paint Distribution Comparison	66
5.3. Workflow DNA-PAINT analyzation	68
5.4. Deposit- and Target-Handle	69
5.5. Pickup and Transportation	71
5.6. Marker Comparison	73
5.7. Loading Procedure Strand Overview	76
5.8. Loading Procedure Strand Overview	77
5.9. Bulk Cargo Loading	78
5.10. PWM Example	80
5.11. Cargo transport experiment (pointer tracking)	83
5.12. Cargo transport experiment (cargo tracking)	86

Abstract

DNA Nanorobots: Directed Molecular Transport and *In Silico* Studies of a Molecular Torsion Spring

In this work, we study a DNA-based, self-assembling nanorobot and enable its use for directed molecular transport. We use coarse-grained molecular dynamics simulations to study mechanical properties of the joint that connects the moving nanorobotic arm to an immobilized baseplate. Our results corroborate the experimental finding that the joint acts as a molecular torsion spring that is capable of storing mechanical energy. Our simulations give first insights to the mechanical and energetical details of this behavior. We conceived a strategy to use the nanorobot to pick up, transport and drop off individual DNA cargo strands. The intended pick-up mechanism was evaluated in another series of molecular dynamics simulations, which we massively parallelized for this purpose. Based on the obtained results, we designed sequences of DNA cargo strands and of the corresponding DNA handles to be attached to the nanorobotic arm and platform, respectively. In the last part of this thesis, we describe the first experimental realization of this transport mechanism, which is observed using fast super-resolution microscopy.

1. Introduction

Robots are machines that are capable to perform a series of complex tasks [1]. Recent advances in engineering and technology allowed such robots to be built ever smaller (e.g. tiny, agile aircrafts inspired by flies [2,3]). However, building robots on nanometer-scale that can interact with single-molecules remains a challenge.

One of the main difficulties to develop robots on nanoscale is the construction. One method in nanotechnology is based on the bottom-up approach, in which single molecules self-assemble based on their chemical properties into complex molecular structures. This approach is inspired by nature, as all living organisms rely on self-assembled structures [4, 5].

A straight-forward example for such structures in nature are proteins. Proteins are the molecular machines inside living cells [6, 7]. The spatial structure of proteins enables their unique functionalities. Some well-known proteins are for example able to

- replicate, translate and transcribe DNA (e.g. DNA/RNA polymerase, ribosome)
- bind to antigens and thereby neutralize them (e.g. antibodies)
- transmit intra- and intercellular signals to coordinate processes (e.g. growth-hormone)
- transport molecular cargo (e.g. kinesin)

...

Despite their great range of functionality, proteins fundamentally consist of a chain of amino acids. Their spatial structure is solely defined by the sequence of the amino acids. Under proper environmental conditions, the proteins fold (self-assemble) from a random coil into the desired shape, due to the interactions of the amino acids [6].

Based on a similar principle, DNA can fold into complex structures as well. In 2006, Rothemund et al. developed a method that was based on the folding mechanism of DNA, in which he used DNA as the construction material [8,9] to design almost arbitrary shapes [10]. These nanostructures are called DNA-origami.

During the last two decades, DNA-origami has led to many breakthroughs in the construction of nanostructures. Mechanical modules like hinges [11–14], sliders [15, 16] or rotary apparatuses [17] were realized on nanometer-scale. Two examples of such nanostructures are shown in Fig. 1.1. Furthermore, DNA-origami gave foundation to

1. Introduction

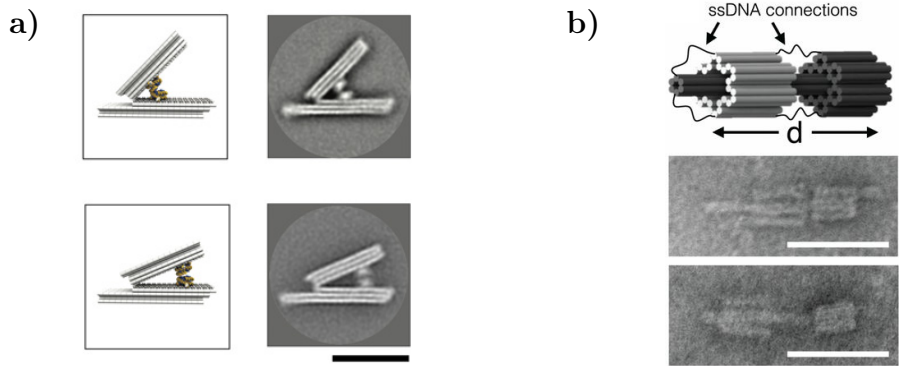


Figure 1.1. | Exemplary DNA-Origami Nanostructures. **a**, Schematic (left) and TEM images (right) of a molecular hinge. Source: [12]. Scalebar: 50 nm. **b**, Schematic (top) and TEM images of two variations of molecular sliders (bottom), Source: [16]. Scalebar: 100 nm.

nanorobots. DNA-based nanorobots have the potential to revolutionize healthcare. For example, recent development has led to the construction of DNA-based nanorobots, that function as therapeutic agents against cancer [18, 19].

In this work, we use a DNA-origami based nanorobot that was developed by Kopperger et al. [20], to develop a nanorobot that can transport molecular DNA-cargo (Chapter 5). Similarly to a crane, the nanorobot consists of a baseplate onto which a rotating arm is placed. The arm is controlled using an electric field. We modified the arm, so that it could pick up cargo, transport the cargo by rotating around its pivot with a radius of less than 25 nm and finally drop off the cargo at a designated site. Such a nanorobot is the fundamental building-block for a molecular assembler.

We developed methods so that we can simulate the most critical phase during the transport mechanism: the pickup of cargo (Chapter 4). The simulations were performed using oxDNA [21]. oxDNA is a coarse-grained molecular-dynamics simulation engine, that was optimized specifically for simulating DNA/RNA. The results of these simulations were used to tune the sequences for the cargo-strands.

Furthermore, we use oxDNA to study the physical and mechanical properties of our nanorobot (Chapter 3). Thereby we simulate the wind-up of the joint as caused by electric actuation of the nanorobotic arm. We find that the joint behaves similar to a torsional spring, that can store mechanical energy during wind-up. These insights were backed by experiments performed by Vogt et al. [22]. Molecular torsional springs are another important mechanical module that can be used for future nanodevices.

2. Biophysical Background

This chapter should give an overview over the physical and chemical background necessary for both, the simulation- and the experimental part of this thesis.

2.1. Deoxyribonucleic acid (DNA)

DNA is a macromolecule with the main purpose to act as an information storage in all living organisms. It encodes the genetic code as a linear sequence of monomers, similarly to binary information storage for computers. However, the monomers of DNA are elements of four different bases. This leads to much higher information density compared to plain binary format, but it also raises the questions: Why does DNA not have even more bases? And why was DNA necessary, when there are other ways to save information, for example in form of proteins or polysaccharides, which consist of many more bases? The limitation of four bases results in rigidity which in turn leads to less possible spatial structures.

However, DNA can also be used for purposes other than information storage. For example, DNA was used in this thesis as construction material for the roboarm-structure. Therefore, it is important to understand the molecular structure and mechanical properties of DNA.

2.1.1. Molecular Structure

The monomers of DNA are nucleotides and consist of three parts: a sugar, a nucleobase and a phosphate group. The backbone is constructed by alternating phosphate and sugar molecules, which bind covalently. If the backbone terminates with a phosphate, then this end is defined as the 5'-end; the other end is defined as the 3'-end (see Fig. 2.1), thereby specifying the direction of DNA. Each sugar has one of four possible nucleobases attached to: Adenine (A), Cytosine (C), Guanine (G) and Thymine (T). Thereby they can form H-bonding with their corresponding complement: Adenine with Thymine and Cytosine with Guanine. All other combinations are not stable in natural environment. Since the bond between $A \leftrightarrow T$ consists of two hydrogen bonds whereas $G \leftrightarrow C$ consists of three, the latter is more stable [23].

2. Biophysical Background

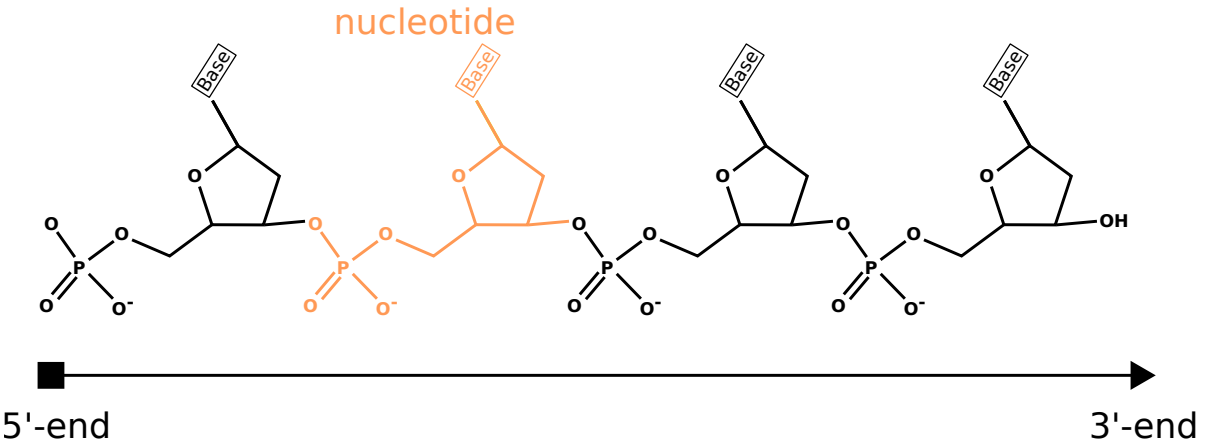


Figure 2.1. | Chemical Structure of DNA. ssDNA with 4 nucleotides is shown, in which the second nucleotide is colored orange. The base is unspecified for all 4 nucleotides and stands for either A, C, G, T. The first nucleotide (on the left side) specifies the 5'-end and the fourth nucleotide (on the right side) specifies the 3'-end.

Such a series of nucleotides is called single-stranded DNA (ssDNA) since it only has one strand. The reverse complement of a given ssDNA is made of all the complements of the original strand's nucleotides in reverse order. For example, the reverse complement of a ssDNA with sequence *AAACT* would be *AGTTT*. Note that in this thesis per convention the sequence of nucleotides is read from 5'-end (left) to the 3'-end (right). Combining the original ssDNA with its reverse complement strand results in a double-stranded DNA (dsDNA), which is the hybridization of both. Here each nucleotide has bonded with the complement, forming base-pairs, of the other strand. Both strands of the dsDNA will twist around each other forming a double-helix. This occurs in multiple forms, depending on the environmental conditions [24], though in nature it is most often found as B-DNA.

Systems with multiple DNA-strands become very complex depending on their length and sequence. For that reason, there are multiple levels to visualize the structure of DNA, as shown in Fig. 2.2:

1. **Primary structure:** The most abstract representation of DNA is delivered in the primary structure. Here, only the linear sequence of the monomers of the DNA is specified, regardless of any spatial structure. Per convention, the sequence is written from 5'-end to the 3'-end.
2. **Secondary structure:** The secondary structure is defined by the H-bond interaction between two complementary bases. Complementary segments can be easily visualized. The secondary structure is especially important for visualizing certain segments or formed structures (e.g. hairpins Sect. 2.4).
3. **Tertiary structure:** The tertiary structure deals with the spatial interactions which will be formed, based on the secondary structure. The tertiary structure is given as the result of every interaction of all nucleotides with each other. Here

2.1. Deoxyribonucleic acid (DNA)

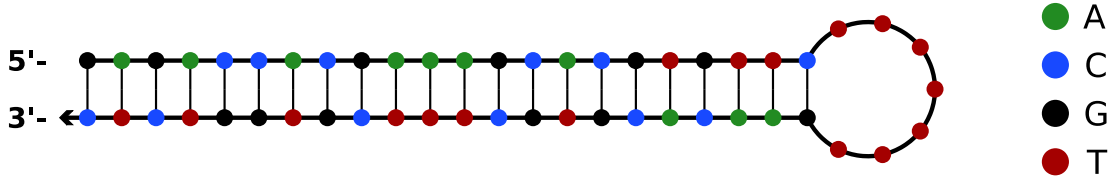
the spatial structure of simple systems (e.g. dsDNA-helix) as well as very complex systems (e.g. DNA-Origami) become apparent.

4. **Quaternary structure:** The quaternary structure is given by the interaction of different sections of DNA or even intramolecular interactions of different strands of the DNA.

a)

5'- GAGACCACGAAAGCACGTGTTCTTTTGAACACGTGCTTCGTGGTCTC -3'

b)



c)

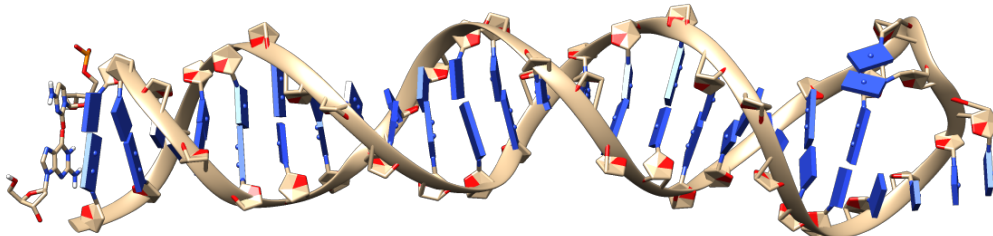


Figure 2.2. | Representations of DNA. a, primary structure of a DNA-strand that incorporates a hairpin. b, stable secondary structure calculated using NUPACK [25]. The hairpin can be observed. c, tertiary structure simulated using oxDNA [21]. The ribbon shows the backbone of the DNA. Ribose rings can be seen. Nucleobases are colored in blue. The hairpin and grooves become visible.

Stacking

Stacking interactions are formed between adjacent bases. They are responsible for excluding water and maximizing Van der Waals interactions. The structural stability of DNA is mainly caused by stacking interactions, rather than the hydrogen bonds [26].

2.1.2. Buffers

Buffers define the chemical environment for DNA, ensuring a stable pH, after addition of small volumes of aqueous liquid. The buffers used in this thesis are listed in the Appendix A.3.

2.2. Rupture of dsDNA

The stability of dsDNA depends on the GC-content, on sequence specific stacking interactions, on the length of the strands and finally on the chemical environment (see Sect. 2.1.2). This section introduces a mathematical approach to model the stability of dsDNA under influence of an external force, based on the work of Mosayeb et al. [27].

In the model, dsDNA in its duplex state is metastable, implying that the separation of dsDNA inevitably happens, given enough time. By applying external forces to the ends of dsDNA, one can speed up the process of separation.

There are multiple ways to do so, summarized in Fig. 2.3:

- **Shearing:** Here, two forces are applied at the opposing ends of both strands, either at both 3'- or both 5'-ends of the dsDNA, pulling apart along the duplex axis.
- **Unzipping:** Here, the two forces are applied on the opposing nucleotides at the end of a dsDNA, pulling the dsDNA apart orthogonally to the duplex axis.
- **Mixed:** While one force is applied to the 3'- or 5'-end of the dsDNA, the other force is applied to any nucleotide of the complementary strand. This results in both shearing and unzipping at the same time.

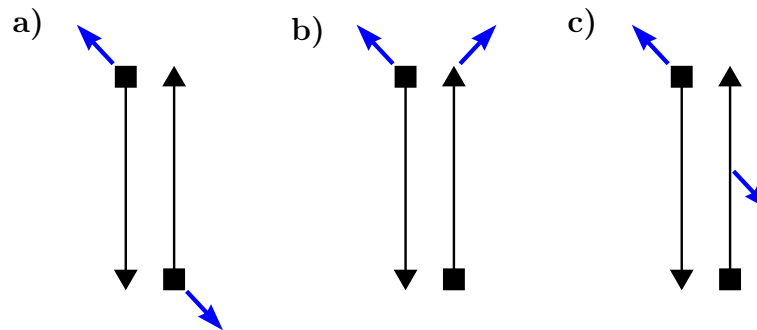


Figure 2.3. | Rupture Overview. Schematically shows different methods to rupture dsDNA. The blue arrows represents an externally applied force, the black arrow represents dsDNA in secondary structure. **a**, shearing. **b**, unzipping. **c**, mixed.

Starting from the metastable state, the dsDNA must first overcome a transition state before being completely separated. In this transition state, only few bases are still bound as a double helix. The transition state can be described by a free energy cost¹

$$\Delta G = N\Delta G_{bp} - \Delta G_0, \quad (2.1)$$

where ΔG_{bp} corresponds to the free energy being accumulated by N base-pairs and ΔG_0 acts as an offset.

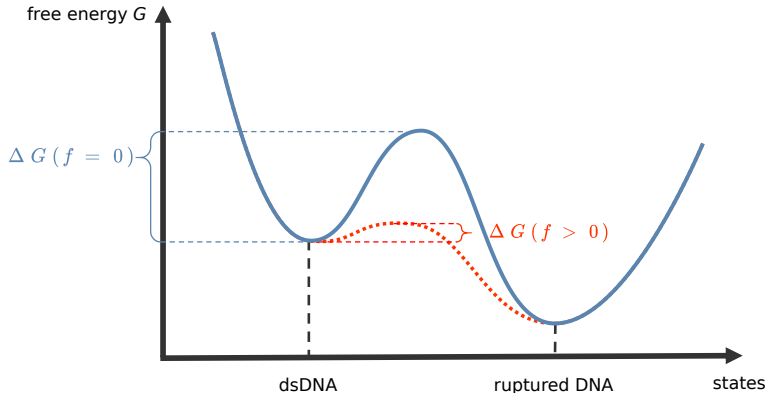


Figure 2.4. | Free Energy at Rupture. Free energy G sketched before (blue) and after (red) applying an external force f that causes the rupture of dsDNA. The activation energy ΔG decreases with applied force, so that $\Delta G(f > 0) < \Delta G(f = 0)$. Thus the rate from dsDNA-state to ruptured DNA state is higher.

When applying an electric force f and thereby pulling apart the strands, then the free-energy-landscape changes as a result of the work performed by the nucleotides:

$$\Delta G = N\Delta G_{bp} - \Delta G_0 - \int_0^f x(f')df'. \quad (2.2)$$

where x is the (absolute) difference in average extension of the original duplex and the transition state. Thus, ΔG decreases or even becomes negative with enough force f applied and therefore will make the transition from duplex state to ruptured state more probable. This change of ΔG is sketched in Fig. 2.4.

This model predicts an increase of the critical force f_c , defined as the force required to rupture strands with a 50%-probability in a predefined time, with an increased number of base pairs. This was verified in simulations and experiments. Simulations further showed, that f_c more than doubled for the shearing process, compared to the unzipping process. This was especially notable for larger duplex-lengths, starting at 12 base-pairs.

This difference in force required for rupturing dsDNA, either by shearing or by unzipping, is utilized for the cargo-transportation mechanism and will therefore be investigated in the following section.

¹The Gibbs free energy G describes the potential for a system to do work at constant temperature and pressure. If a system has negative free energy, then it will spontaneously react. If a system has positive free energy, then external energy (e.g. electrical work) must be added for the reaction to occur.

2. Biophysical Background

2.3. Transportation mechanism of Single-Molecule-Cargo

The cargo to be transported consists of single-stranded DNA. The goal was to transport such cargo from a deposit-area to a designated target-area, using the nanorobotic arm structure. The task of the arm was to pick up cargo that was stored at the deposit-area, transport the cargo and finally drop the cargo off at the target-area. For that, the sequence of the cargo required a \overline{PH}^* -domain and a \overline{C}^* -domain. The \overline{PH}^* -domain binds to the pickup-handle, which is a ssDNA attached to the arm, and the \overline{C}^* -domain binds to either a deposit- or a target-handle at the deposit- or target-area respectively. The starting-point for the transportation is given by the cargo-strand being hybridized to the deposit-handle and the pickup-handle. This configuration is shown in Fig. 2.5a).

Pickup cargo at deposit-area

Rupture of the cargo-strand is induced by applying a force to the pickup-handle, for example by trying to rotate the arm of the nanorobotic arm structure. Thereby a sequence with more bases or a higher GC-content was chosen for the deposit-handle \overline{C}^* compared to the pickup-handle \overline{PH}^* . However, unzipping of the cargo-strand from the deposit-handle is still more favorable compared to shearing of the cargo-strand from the pickup-handle (see Sect. 2.2). Thus, the cargo-strand can be picked-up using the pickup-handle (see Fig. 2.5b)). After pickup of the cargo-strand, the domain \overline{C}^* of the cargo-strand is single-stranded.

Drop cargo at target-area

The picked-up cargo-strand is then transported using the pickup-handle to the target-area, where the single-stranded \overline{C}^* -domain hybridizes to a designated target-handle (see Fig. 2.5c)). When now a force is exerted on the pickup-handle, shearing at either the pickup-handle or the target-handle is induced. As the binding of the cargo-strand to the target-handle is stronger compared to the binding of the cargo-strand with the pickup-handle, the cargo-strand shears from the pickup-handle with a higher probability than it would shear from the target-handle. Thus the pickup-handle ruptures from the cargo-strand, while the cargo-strand stays hybridized to the target-handle, as shown in Fig. 2.5d).

The concept of utilizing the difference in force required for shearing versus unzipping to transport single-molecular cargo-strands was inspired by the work done by Kufer et al. [28], where he used an atomic force microscope (AFM) for that purpose.

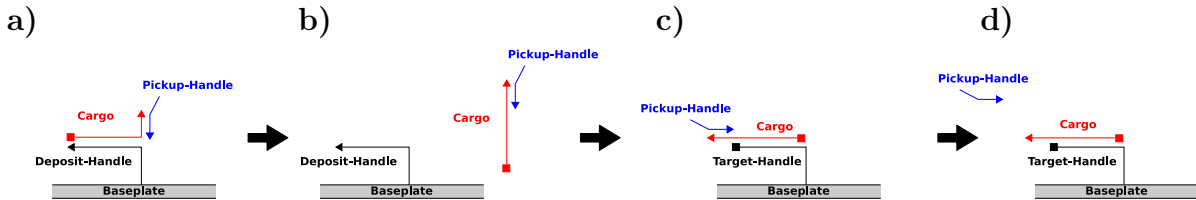


Figure 2.5. | Transport Mechanism. Schematics of the transportation mechanism of DNA-cargo, using the pickup-handle with sequence \overline{PH}^* and the deposit- and target-handle with sequence **C**. **a**, shows the starting-point, where the cargo is hybridized to both, a deposit-handle and the target-handle. **b**, shows the cargo being unzipped away from the deposit-handle, after a force was applied to the pickup-handle. At this point, the cargo is only hybridized to the pickup-handle. **c**, shows the cargo transported and hybridized to a target-handle. Note that the target-handle has the reversed sequence of the deposit-handle. **d**, shows the pickup-handle sheared away from the cargo-strand, after applying a force.

2.4. DNA nanotechnology

In this thesis, we use a nanorobot based on DNA to transport DNA-cargo. This section covers state-of-the-art nanotechnology based on DNA, used here as a construction material instead of a pure medium of information storage [8, 29].

2.4.1. Elementary Structures

Hairpins

A hairpin is the result of ssDNA forming a loop with a stem. The strand consists of three segments, where the first and third segments are complementary to each other, forming a duplex stem, while the segment inbetween is orthogonal, forming the loop.

The stability of hairpins depends on the size and sequence of the stem and loop: Generally a longer/smaller stem results in a more stable/less stable hairpin. The loop however has an optimal size of 4 to 8 nucleotides; shorter loops will not form a hairpin, longer loops will often form other secondary structures.

Toehold mediated strand displacement (TMSD)

TMSD is the exchange of two strands, a protector strand and an invader strand, sharing and competing over a common domain, the substrate [30, 31]. Eventually the invader strand fully displaces the protector strand and forms a duplex with the substrate. This process is schematically shown in Fig. 2.6.

The substrate is a ssDNA with two segments S1 and S2, the protector strand is the complementary to S1. At first, the protector strand is fully bound to the substrate, leaving only the segment S2 exposed. After adding the invader strand, which is fully

2. Biophysical Background

complementary to the substrate, the invader hybridizes to S2 of the substrate, the toehold. Since Watson-Crick base-pairing of a single base-pair is not thermally stable, the ends of the protector strand can open [23] from the substrate, giving opportunity for the invader strand to hybridize even more to the substrate. Though the opposite can happen as well, the invader strand stays hybridized to the toehold. Given enough time, the invader strand completely displaces the protector strand forming a new duplex. Kinetics were investigated in detail by Zhang et al. [32].

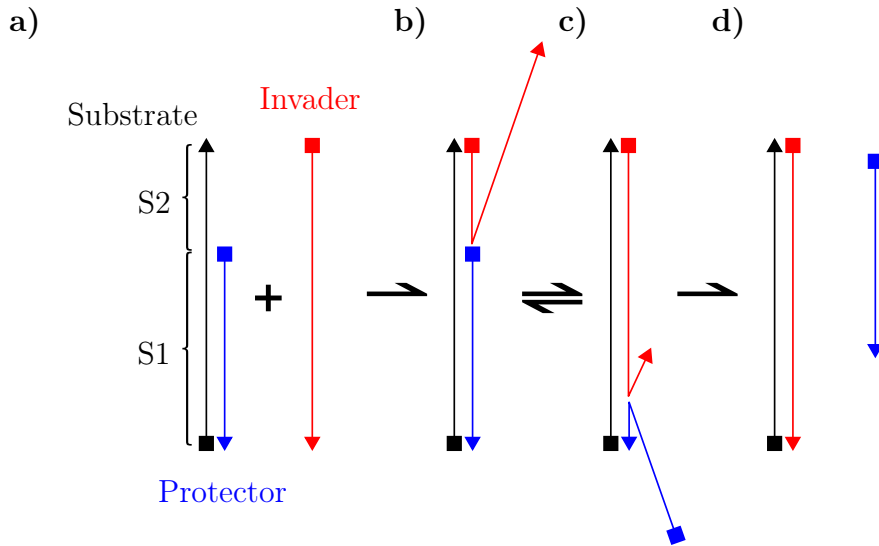


Figure 2.6. | Toehold Mediated Strand Displacement. Schematically shows a simplified model of TMSD. **a**, defines the starting-point. A protector-strand has hybridized to the substrate, so that only **S2** remains single-stranded. In **b**, an invader-strand hybridized to the substrate. Similar to a random walk, the invader-strand displaces the protector-strand and vice versa. In **c**, only few bases remain bound to the substrate. Finally, in **d**, the protector-strand has fully dissociated from the substrate. Since the invader-strand fully binds to the substrate, the protector-strand stays dissociated.

Holliday junction

The immobile holliday junction is the fundamental building block for DNA-Origami, as it enables a stable connection of multiple DNA-strands. The immobility comes from an asymmetrical sequence, as first developed by Seeman et al. [29], shown in Fig. 2.7a).

A holliday junction is a DNA-structure consisting of four DNA-strands contributing to duplex arms, which are interconnected with each other. There are two main conformations for this structure [33]:

- unstacked form: This is the preferred conformation in absence of metal ions. The junction is fully extended resulting in four separate duplex arms.
- stacked form: The presence of metal ions shields electrostatic repulsion which leads to a stacked junction with only two straight arms. An example is shown in Fig. 2.7b).

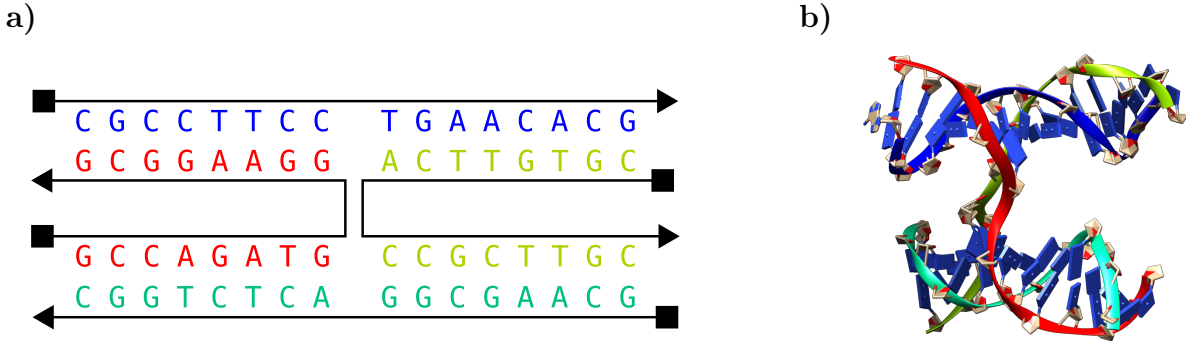


Figure 2.7. | Holliday Junction. **a**, secondary structure of immobilized holliday junction developed by Seeman et al. [29]. **b**, tertiary structure of a holliday junction in stacked form, obtained from an oxDNA-simulation, simulated at 1 M salt concentration.

2.4.2. DNA-Origami

DNA-Origami is a method to use DNA as construction material to build self-assembling nanostructures from the bottom up. The general concept was developed by Rothemund in 2006 [10], but new nanostructures are being designed ever since. The nanorobot used in this thesis (see ref 2.5) is based on DNA-Origami, but there are also many other functional structures like crank-sliders [16], hinges [12] or viral-like shells [34].

Concept

In DNA-Origami, one long ssDNA-strand acts as the scaffold for the nanostructure. The scaffold-strand is held in the desired shape by many staples, which are short oligonucleotides (typically 32bp long [35]), complementary to the scaffold. Their sequence is uniquely designed, so that they only bond at specific positions and form immobilized holliday junctions.

For the scaffold, any sequence can be used. Rothemund utilized the circular genome of the M13 bacteriophage which has 7249 nucleotides. This scaffold is still commonly used, though often in slight modifications, either extending or shortening the sequence [36].

Even though theoretically the scaffold could be folded into almost any shape, the DNA-Origami used in this thesis is based on a common design pattern, where the routing of the scaffold lies in a lattice of helices that are antiparallel and adjacent to each other. Antiparallel crossovers [37], either by the scaffold or the staples, form the connection between neighboring helices. This design-pattern can be implemented using the square-lattice or the honeycomb-lattice.

However, the square- and honeycomb-lattice restricts DNA-origami designs to be 2D only. In order to design 3D DNA-origami, one can design the nanostructures modularly, where each module follows the the square- or honeycomb-lattice design pattern.

2. Biophysical Background

Afterwards, the modules can be combined. This was for example done for the roboarm-structure, where the pointer and the baseplate were designed separately.

Computer aided design: **caDNAno**

The software **caDNAno** was developed to help designing DNA-origami, using either the square- or the honeycomb-lattice [38]. **caDNAno** can be used to design staples at specific positions of the scaffold, so that the scaffold folds in the desired shape. **caDNAno** was used in this thesis to develop the various structures used, for example the Marker-structure or the pickup-handle of the arm.

Design considerations

The design of stable, yet functional DNA-Origami poses many challenges on behalf of staple choice. The following should summarize some of the most important design choices and act as a guideline, not as a rigorous rule set, based on [35, 39]:

- Choose staples with a length of 32 bases, routed in three helices each, where the first 8, the middle 16, the last 8 bases belong to the first, the intermediate, the third helix respectively.
- Design the edges with poly(T) hairpins standing out of the structure. This prevents the nanostructures from sticking together and thus eliminates cluttering.
- Regularly introduce a gap between adjacent staples, to relax strain caused by twisting which results from the difference of a helical turn (10.67 nucleotides per turn) compared to a duplex turn (10 to 10.4 nucleotides per turn [40]) How often these gaps need to occur depends on the lattice used (e.g. for square-lattice: one base-pair every 48 nucleotides [41]).

Folding

After completing the design, the origami is ready to be folded, which is done by mixing the staples together with the scaffold.

The folding itself is highly cooperative [42, 43]. This means that after few staples have hybridized to the scaffold, the hybridization of other staples in near vicinity becomes easier and thus faster. Because of that, simple structures tend to only require one specific temperature to fold, while more complex structures still require multiple temperatures.

To ensure that the folding-process takes place, the temperatures required for cooperative folding has to be set. This is done by a thermocycler that slowly (e.g. $0.05\text{ }^{\circ}\text{C min}^{-1}$) regulates the temperature from high (e.g. $70\text{ }^{\circ}\text{C}$) to low (e.g. $20\text{ }^{\circ}\text{C}$). This is visualized in Fig. 2.8

To make sure that every origami-structure contains all staples, one can add a surplus of staples to the folding process. One discards the leftover staples by performing purification methods (see Section 5.1.1).

For folding it is important to use a buffer with a relatively high ion concentration to prevent electrostatic repulsion of the backbone of staples and scaffold. In this thesis, FOB20 (see A.3) was used, but variations are possible.

Temperature

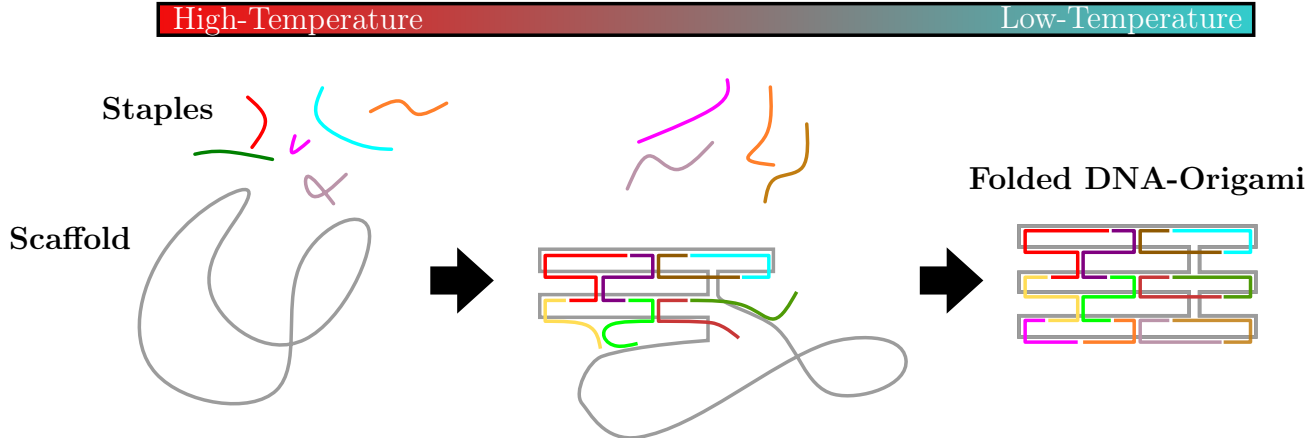


Figure 2.8. | Folding Process. Sketched folding process in thermocycler. The left side shows the starting point in thermocycler at a high temperature, where no staples are bound to the circular scaffold-strand (grey) yet. As temperature decreases, cooperative folding begins, shown in the middle. When the end-temperature is reached, all staples are bound to the scaffold and the scaffold-strand is folded in desired shape, shown on the right side.

2.5. Roboarm

The roboarm, shown in Fig. 2.9, is the main DNA-origami nanorobot used in this thesis and was developed by Kopperger et al. [20]. The structure consists of a baseplate, to which a freely rotating arm is attached to. The arm can be extended by a pointer structure. By fixating the baseplate, one can control the rotation of the arm on a millisecond timescale using electric fields, giving it a great advantage over previous, much slower biochemical approaches [20]. The pointer acts as a leverage activated by the electric fields that generally increase torque on the arm.

Baseplate

The baseplate is made of two $55\text{nm} \times 55\text{nm}$ origami plates stacked on top and twisted by 90° against each other. This ensures more stability and thus allows for more torque to be applied. The baseplate has six biotin-anchors sticking out of the bottom, which

2. Biophysical Background

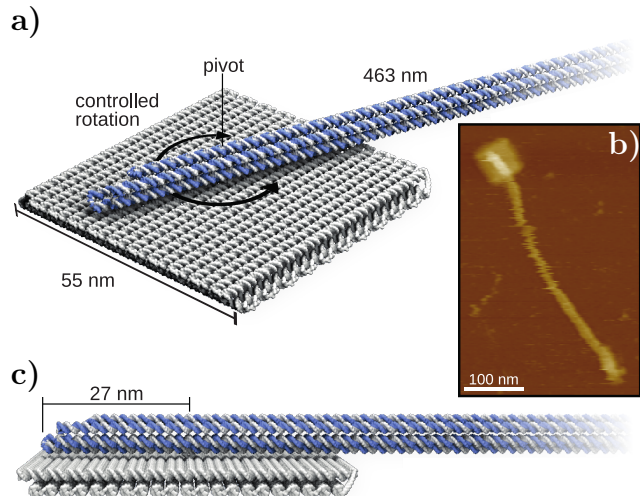


Figure 2.9. | Roboarm Structure. Roboarm-structure with the High-Aspect-Ratio-Pointer implemented. **a**, 3D-view of roboarm structure that was used in the experiments. The pointer was controlled with an electric field that rotated around the pivot. **b**, AFM-image of roboarm structure **c** side-view of the roboarm structure. Source: [22]

can be used to fixate the roboarm via neutravidin on glassslides that are coated with biotin-polyethylene glycol-silane (Biotin-PEG-Silane).

The sequence of the scaffold used for the baseplate is the p7249, though in combination with the arm, the extended scaffold with sequence p7704 was used.

Arm, Joint and Pointer

The design of the arm varies with the pointer being used. The arm still belongs to the same scaffold as the baseplate, while the pointer is a separate origami-structure. Therefore the arm forms the connection with the baseplate via the joint to the pointer. Furthermore, the arm provides possible extensions to be used for the pickup-handle to transport the cargo.

There are multiple variations for pointers that can be used. In general, they are cylindrical nanostructures which can be aligned using an external electric field. The alignment is caused by electrophoresis, electro-osmosis and electro-static interaction with the negatively charged backbone of the pointer [44]. A constantly rotating electric field, like $\vec{E} = E_0(\cos(\omega t), \sin(\omega t))^\top$, will cause the pointer to rotate accordingly, resulting in the wind-up of the joint.

The joint is the connection of the baseplates and the arm. It is usually part of the scaffold and consists of two sections of ssDNA. Since both sections are not hybridized together, they are very flexible and thus allow for rotation of the arm. The specific structure of the

joint will be introduced and discussed in 3.1.3. Detailed molecular-dynamic simulations were performed to study the mechanical properties of the joint (see Chapter 3).

Pointers used in this thesis were the High-Aspect-Ratio-Pointer, the Low-Aspect-Ratio-Pointer and the Tapered-Pointer (see Fig. 2.10). They differ from each other by their shape. The High-Aspect-Ratio-Pointer is the longest, having its electro-static center most distant from the joint which should in principle lead to the highest torque. However, bending of the pointer and other effects limit the effective torque.

On the contrary, the Low-Aspect-Ratio-Pointer is shorter, but therefore thicker in diameter and hence more rigid.

The Tapered-Pointer is a compromise of both, having a cone-like shape with decreasing diameter towards the tip.

All pointer have a fluorophore attached at the end, so that they can be detected using a microscope.

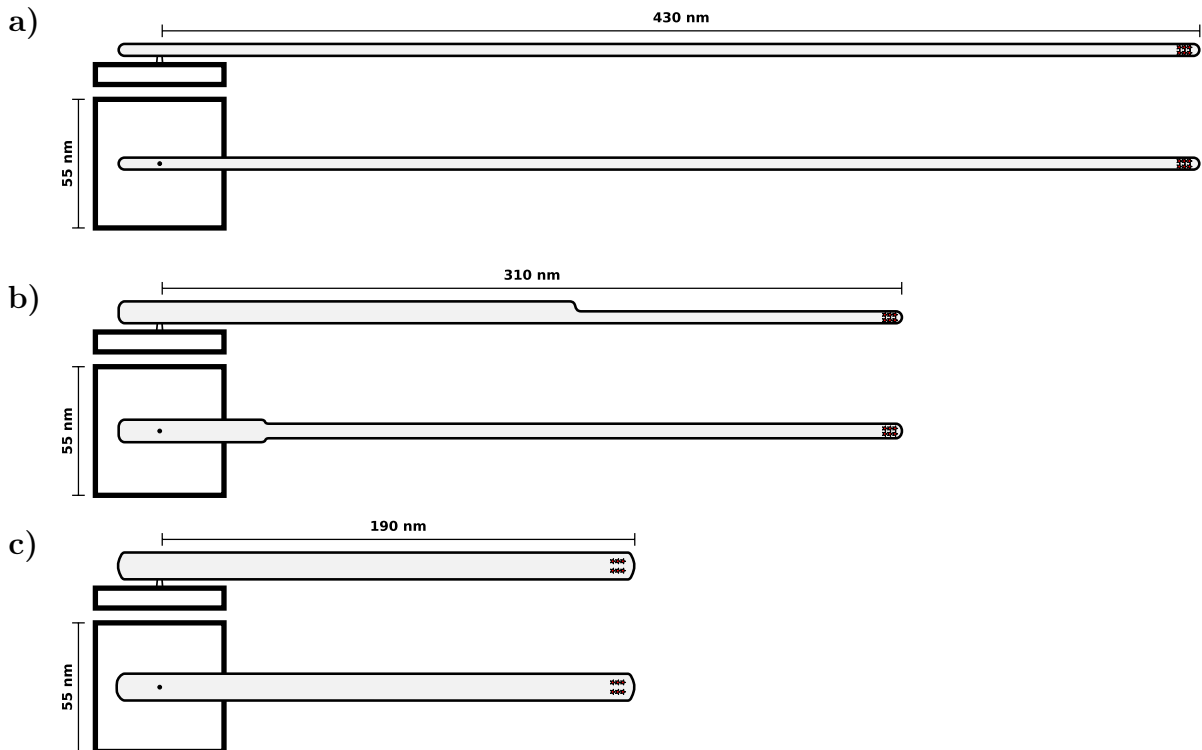


Figure 2.10. | Pointer Comparison. Overview of different pointers that could be implemented for the nanorobot. **a**, High-Aspect-Ratio-Pointer. **b**, Tapered-Pointer. **c**, Low-Aspect-Ratio-Pointer.

2.6. Fluorescence

Fluorescence is the process for material to absorb photons of high energy, thereby transitioning to an excited state, and then emit photons usually with longer wavelength

2. Biophysical Background

(smaller energy), to relax back to its ground state [45]. In fluorescence, the emission happens immediately after absorption. This must not be confused with phosphorescence where emission is delayed minutes or even hours.

After absorption of a photon, part of the energy can get lost for example to collisions with nearby molecules [46]. This lowers the energy level in a non-radiative manner before finally emitting a photon with the leftover energy. Another reason for the lower energy of emitted photons can be caused by excitation of higher vibrational energy levels. Since the energy of a photon is $E = hf$ with h being Planck's constant and f the photon's frequency, emitted photons have lower frequency and thus longer wavelength.

When the molecule is in excited state, interactions with other molecules can induce permanent covalent changes leading to inability to fluoresce anymore. This phenomenon is known as photobleaching. To reduce photobleaching, one can reduce the intensity of excitation, though this leads also to lower intensity of fluorescence. The absence of oxygen also delays photobleaching [47]. One can achieve this by mixing enzymes into the buffer, that use oxygen for their enzymatic action.

In this thesis, the two fluorophores Atto655 (A655) and A532 were used. Note that A532 showed much faster bleaching. The use of antibleach-buffer was therefore necessary (see Appendix A.3).

2.7. Chemical kinetics

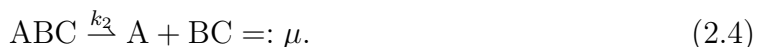
Rates mathematically describe chemical kinetics, that is the speed at which chemical reactions take place. The order of a reaction is given by the sum of the exponents given in the rate equation. This section should only cover chemical reactions important for this thesis.

Cargo Pickup Process

Let ABC describe the initial state, where the cargo B is attached to both, the cargo-handle A and the pickup-handle C. During the process of pick-up, two events can happen (see more details in 2.3):

- The cargo is being successfully picked up by the pickup-handle.
- The cargo ruptures away from the pickup-handle and thus stays attached to the cargo-handle.

This defines two reactions of first order:



This can be solved to

$$c_{ABC}(t) = c_{ABC}(0) \cdot e^{-kt} \quad (2.5)$$

$$c_{\lambda/\mu}(t) = 1 - \frac{k_{1/2} \cdot c_{ABC}(0)}{k} e^{-kt} \quad (2.6)$$

with $c_{\lambda/\mu/ABC}$ being the concentration of λ , μ or ABC and $k := k_1 + k_2$.

Hybridization and melting of a duplex

This reaction explains the assembly process during folding. It will also become important for characterizing methods used later. The reaction where two ssDNA-strands A and B with concentrations c_A and c_B hybridize together, forming as dsDNA-strand AB



lead to the reaction rate

$$\frac{dc_{AB}}{dt} = k_{on}c_A(t)c_B(t) - k_{off}c_{AB}(t). \quad (2.8)$$

Conservation of matter states as

$$\frac{dc_A}{dt} = \frac{dc_B}{dt} = -\frac{dc_{AB}}{dt}. \quad (2.9)$$

One can solve the Eq. 2.8 using Eq. 2.9 for the case that a huge excess of strand A exists, so that the concentration $c_A(t) = c_A = \text{const}$, and furthermore that the hybridized dsDNA is stable, so that $k_{off} = 0$, as

$$c_A(t) = c_A \quad (2.10)$$

$$c_B(t) = c_B(0)e^{-c_A k_{on} t} \quad (2.11)$$

$$c_{AB}(t) = c_B(0) \left(1 - e^{-c_A k_{on} t}\right) + c_{AB}(0). \quad (2.12)$$

This could for example be used to find the fraction of blocked deposit-handles in the *post-blocking-cargo-loading* protocol (see Sect. 5.3.1). In this case, strand A resembles the blocker-strands, the unblocked deposit-handles are described by strand B and the blocked deposit-handles by strand AB.

In the case of equilibrium, the reaction rate vanishes $\frac{dc_{AB}}{dt} = 0$. The equilibrium coefficient K is then defined by the ratio

$$K = \frac{c_{AB}(t)}{c_A(t)c_B(t)} \stackrel{(2.8)}{=} \frac{k_{on}}{k_{off}} \quad (2.13)$$

2. Biophysical Background

This ratio could for example be used to describe the contrast of PAINT-imager, using the ratio of on-time (eq. 5.1) and off-time (eq. 5.2) of the imager.

2.8. oxDNA - a coarse grained MD simulation engine

Molecular dynamics (MD) simulations aim to give insight on the time evolution of molecules, based on realistic models describing their interactions. These insights are often experimentally very difficult or even impossible to obtain.

However, complex models lead to an increase of computing power as well. All-atom simulations, respecting intra-molecular interactions, thus being very realistic, are yet not practical for simulations of large molecules (e.g. DNA-Origami) on longer time-scales (up to $20\mu\text{s}$). This led to the choice of a coarse grained simulator.

2.8.1. The Model

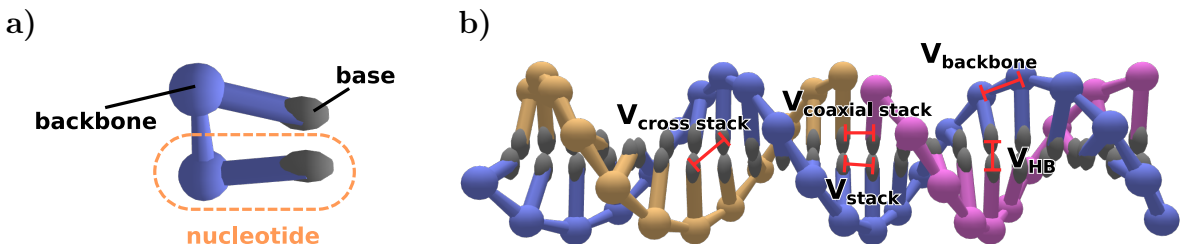


Figure 2.11. | oxDNA2 Model. **a**, shows balls-and-sticks representation of nucleotides in oxDNA, in which the atomar structure is coarse-grained on nucleotide-level. **b**, shows most interactions implemented in oxDNA. Note that the term for volume-exclusion V_{exc} and the Debye-Huckel-like term V_{DH}^* are not shown.

xDNA is a coarse grained simulator developed by Ouldridge et al. [21] specially designed for simulations of DNA structures. Besides MD-simulations, oxDNA is also capable of running Monte-Carlo simulations. However, Monte-Carlo simulations were not used in this thesis and will not be discussed further.

The model of oxDNA is coarse graining on the level of nucleotides, that means that only interactions between nucleotides are modelled. Any intra-nucleotide interactions are disregarded. The dynamics of the nucleotides are calculated by one of several thermostats (see 2.8.2). For that, the pairwise interactions were modeled by potentials for backbone connectivity V_{backbone} , stacking V_{stack} , excluded volume V_{exc} , hydrogen-bonding V_{HB} , cross-stacking $V_{\text{cross_stack}}$, coaxial stacking $V_{\text{coax_stack}}$ and electrostatic interactions via Debye-Huckel-like term V_{DH}^* [48, 49]. Thus the total potential is given by

$$V = \sum_{\text{nearestneighbours}} (V_{\text{backbone}} + V_{\text{stack}} + V'_{\text{exc}}) + \sum_{\text{otherpairs}} (V_{\text{HB}} + V_{\text{cross_stack}} + V_{\text{coax_stack}} + V_{\text{exc}} + V_{\text{DH}}^*) \quad (2.14)$$

which is evaluated in every simulation step.

2.8.2. Thermostat

Thermostats control the temperature of in the system that is simulated. Thermostats used in this thesis were:

- Bussi: velocities of nucleotides are drawn from the canonical distribution and are rescaled by a properly chosen random factor [50].
- John: in every simulation step, the velocity of nucleotides gets randomly altered with a defined probability, following the Maxwell-Boltzmann velocity distribution.

2.8.3. External forces

External forces can be used to influence the simulations. They are as well implemented using different potentials. Forces used in this thesis are

- Mutual trap: harmonic force between two nucleotides.
- String: Force that is independent of the positions of the nucleotides.
- Harmonic trap: harmonic force between a particle and a reference point. The reference point can move during the simulation in a straight direction.
- Rotating harmonic trap: Like the harmonic trap, but the reference point can move on a circular path around a defined origin.
- Repulsion plane: Harmonic repulsion when nucleotide is behind the defined plane.

With exception of the string-force, all other force types depend on a distance r between the nucleotides and a reference point. These forces have a quadratic potential, thus scale linearly with distance: $F = k r$, where k is the stiffness (proportionality constant). One can compare these forces to linear springs following Hooke's law, where k would be the spring constant. For more details, please refer to the official documentation [51].

2.8.4. Relaxation in oxDNA

Before starting the simulation, it is often necessary to first "pre-relax" the DNA-structures. This is necessary, to prevent unrealistic extensions of the backbone or overlapping nucleotides, which is a common artifact when using CAD software like caDNAno. Ignoring them would lead to enormous forces that would cause the simulation to fail.

Summarized there are few main differences to the simulation:

2. Biophysical Background

- Thermostat: For relaxation, the Bussi-thermostat is used, instead of the John-thermostat.
- Mutual traps: Defining mutual traps between every base-pair ensures that the bond will not break.
- (Optional;) Maximal backbone stretch: Since V_{backbone} diverges when the backbone is too far stretched ($r > 0.873\text{nm}$) [52], one can artificially limit the maximal force that the backbone can exert, preventing the relaxation to fail.

3. Simulation of Joint

In this chapter, we show oxDNA studies that focus on the joint of our nanorobotic arm structure. Using oxDNA simulations, we investigate molecular and mechanical properties of the joint. Furthermore, we study how variations of the joint change these properties. The results of the simulations performed are well in agreement with experiments performed by Vogt et al. [22]. The results of this chapter were used in [22].

The findings are also important for the mechanism of cargo-transportation, as the joint has major influence on the dynamics of the roboarm. A more flexible joint leads to less resistance when rotating the roboarm, thus results in potentially higher torque, which makes pickup-procedure more probable. On the other hand, a more flexible joint also reduces stability.

Furthermore, we treat the simulated joint as a torsional spring with Hooke's characteristics. Thereby we show that mechanical energy can be stored and released in the joint. This concept was experimentally verified by Vogt et al. [22].

This chapter is divided into three sections: first explaining the setup and methods used for simulating the rotating roboarm, then presenting the results and finally an in-depth discussion comparing the results with proposed theoretical models and assessing the reliability for comparison with the real-world roboarm.

3.1. Simulation Setup

3.1.1. Miniaturized Structure

When replicating the experimental setup in MD-simulations, the high complexity of the roboarm ($\approx 15\,000$ nucleotides) would be too computationally intensive for simulating on microsecond-timescale in oxDNA with current hardware.

To solve this, we used a miniaturized version of the roboarm for the simulations (see Fig. 3.1). Here the two-layer baseplate is only $35\text{ nm} \times 35\text{ nm}$ large (compared to $55\text{ nm} \times 55\text{ nm}$ from the experiment). Furthermore, the pointer used for actuation via an electric field and visualization using TIRF-microscopy was not implemented in the simulation. Instead, the joint is only attached to a shorter, symmetric 6hb-arm, to which the High-Aspect-Ratio-Pointer could be attached to. Therefore, the miniaturized roboarm consists of approximately half the number of nucleotides as the roboarm used in experiments.

3. Simulation of Joint

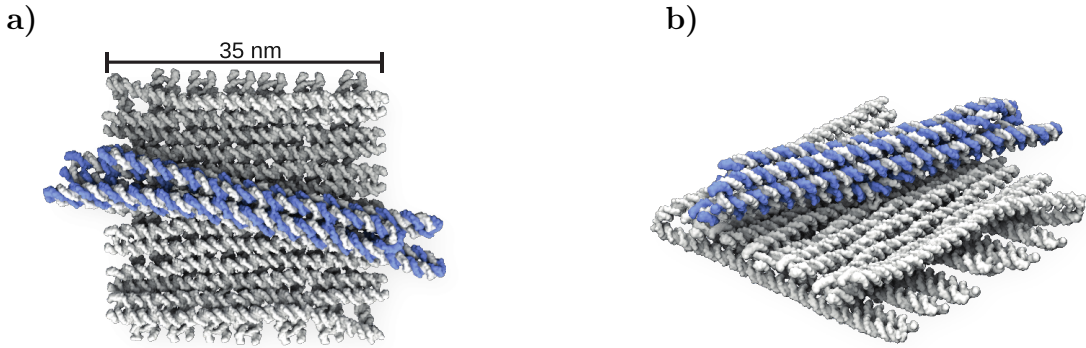


Figure 3.1. | Miniaturized Roboarm Structure. **a**, top-view of the miniaturized structure that was used for simulations in this chapter. Colored in blue is the arm that is being rotated by rotating-harmonic-traps. **b**, 3D-view

However, to achieve most realistic results, an identical design choice for the joint was implemented consisting of the same lengths and sequences that could be used for the real-world roboarm.

Since the physical properties of the joint are purely local, the down-scaling of the baseplates and the absence of the pointer are not expected to impact the joint. By downscaling the structure, simulations on timescales of microseconds become feasible.

To resemble the six biotin-anchors used to fixate the structure on Biotin-PEG-Silane-coated glassslides, harmonic-traps were defined for six staple-extensions on the bottom-side of the baseplate. Each harmonic-trap had a stiffness of 73 pN nm^{-1} . They were placed in a similar manner as the biotin-anchors for the real-world roboarm. However, due to downscaling of the baseplates, distances from the traps to the joint became smaller.

3.1.2. Rotating Driving Forces

In the real-world, the roboarm (with pointer attached to) aligns to an external electric field. A rotating electric field thus causes the continuous rotation of the roboarm. In oxDNA, the closest resembling force would be a string-force, emulating an electric field as the magnitude of the force applied is independent of the position of the nucleotides. However, the orientation of the string-force must be constant which makes it unsuitable for the purpose of rotating the roboarm.

The approach used in this thesis was to use six rotating-harmonic-traps, attached to one outer nucleotide at the end of each helix (distance to pivot: $R = 16.3 \text{ nm}$) of the 6hb-arm (see Fig 3.2a)). The origin, around which the traps rotate, was defined at the position of the joint. The starting positions for time $t = 0$ of the rotating traps coincide with the positions of the corresponding nucleotides in the start-configuration, so that

3.1. Simulation Setup

the exerted force would gradually increase as the traps start rotating in the beginning of the simulation. Using this method, one can successfully simulate the rotation and thus the wind-up of the joint in oxDNA.

However, this implementation differs from the expected angle dependency of an electric field in some aspects. To illustrate the differences, one can split the forces exerted by the rotating traps in a radial and a tangential component. The radial component F_{\parallel} is directed towards the center of the joint whereas the tangential component F_{\perp} is perpendicular to the roboarm and applies torque, thereby accelerating or decelerating the rotation of the arm.

Suppose the roboarm is fixated and thus cannot rotate. This could for example be the case during cargo-pickup when the roboarm is attached to cargo which in turn is attached to the baseplate (see 2.3). Let us choose a coordinate system, in which the roboarm is aligned on the x-axis.

When using an electric field $\vec{E} = E_0(\cos(\alpha), \sin(\alpha))^{\top}$ to apply a torque on the real-world roboarm, the roboarm experiences

$$F_{\parallel}^{\text{exp}}(\alpha) = E_0 Q_{\text{eff}} \cos(\alpha) \propto \cos(\alpha) \quad (3.1)$$

$$F_{\perp}^{\text{exp}}(\alpha) = E_0 Q_{\text{eff}} \sin(\alpha) \propto \sin(\alpha) \quad (3.2)$$

, where Q_{eff} denotes the effective charge of the pointer and α is expresses the angle of the electric field. For $\alpha = 0$, the electric field is aligned on the x-axis, pointing in the same direction as the roboarm, exerting maximal force in radial direction. For $-\pi/2 < \alpha < \pi/2$, the radial force stays positive, as visualized in Fig. 3.2c) for the case of $\alpha \approx 45^\circ$

When using the rotating traps in the simulation, let $\vec{x}_{\text{trap}} = R(\cos(\gamma), \sin(\gamma))^{\top}$ be the position-vector of the traps and $\vec{x}_{\text{nucl}} = R(1, 0)^{\top}$ the current mean position-vector of the nucleotides, the traps are assigned to. This implies that the roboarm is still aligned on the x-axis. Note that here R denotes the radius of the rotating-harmonic-traps, which is equal to the distance between the pivot and the nucleotides the traps are assigned to. Here γ is the angle of the traps with respect to the x-axis. Then the resulting force of the traps is given by $\vec{F}^{\text{sim}} = k(\vec{x}_{\text{trap}} - \vec{x}_{\text{nucl}})$, where k is the stiffness of the rotating-harmonic-traps. As derived in appendix A.1, the force then splits as

$$F_{\parallel}^{\text{sim}}(\gamma) = kR(\cos \gamma - 1) \propto \cos(\gamma) - 1 \quad (3.3)$$

$$F_{\perp}^{\text{sim}}(\gamma) = kR \sin(\gamma) \propto \sin(\gamma). \quad (3.4)$$

Note that $F_{\parallel}^{\text{sim}}(\gamma) \leq 0$ for any $\gamma \in [0, 2\pi]$, as visualized in Fig. 3.2b) for the case of $\gamma \approx 45^\circ$.

Comparing the forces acting on the real-world roboarm with the simulated forces, the differences for the radial component become apparent: when $\alpha = \gamma = 0$, then the electric field exerts force in radial direction while the rotating traps in the simulation do not

3. Simulation of Joint

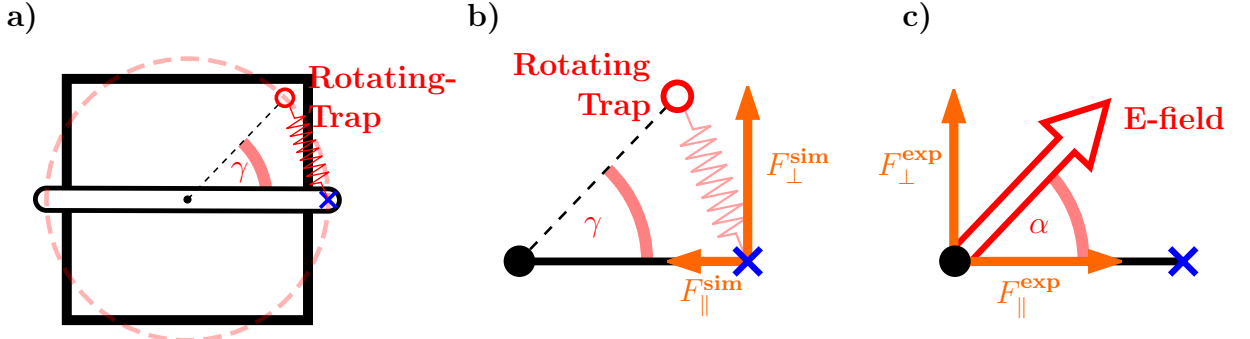


Figure 3.2. | Comparing driving forces. **a**, depicts an overview of the simulated roboarm. The rotating traps are shown summarized as the red, solid circle, that rotates around the pivot on the red dashed circle. The rotating traps are assigned to nucleotides at the tip of the arm, that are visualized by the blue X. **b**, shows the resolution of force exerted by the rotating trap. **c**, shows the resolution of force exerted by a homogenous electric field at the same angle, so that $\gamma = \alpha$. The magnitude of the electric field was chosen, so that $F_{\perp}^{\text{sim}}(\gamma) = F_{\perp}^{\text{exp}}(\alpha)$. Note, that here $F_{\parallel}^{\text{exp}}(\alpha)$ points in the opposite direction compared to $F_{\perp}^{\text{sim}}(\gamma)$.

exert a force at all. For the other extremum, when $\alpha = \gamma = \pi$, the traps in the simulation exert twice the radial force towards the joint compared with the radial forces caused by the electric field, with respect to the maximum tangential force.

However, when choosing the appropriate stiffness k , then the tangential force from the simulation is equal to the tangential force caused by the electric field for the real-world roboarm: $F_{\perp}^{\text{sim}}(\gamma) = F_{\perp}^{\text{exp}}(\gamma)$. Since the resulting torque is directly proportional to the tangential force, the simulation realistically mirrors the torque that would be applied by the electric field.

All rotating-harmonic-traps combined had a total stiffness of $k = 0.30 \text{ pN nm}^{-1}$. This value was defined empirically. Though this value could further be fine-tuned to represent more realistically the real-world roboarm, the goal of this simulation was to qualitatively investigate the differences between the different variants of joints, not to represent the real-world roboarm as realistically as possible. Furthermore, regarding the tangential forces, the stiffness linearly depends on the magnitude of the electric field: $k \propto E_0$. When varying the electric fields used in the experimental setup, one would need to adjust the stiffness for the simulations accordingly.

The rotating traps performed mechanical work to rotate the roboarm. This work directly follows from the tangential component F_{\perp}^{sim} , as the radial component does not contribute to the motion of the roboarm.

To formulate the work, let the roboarm be aligned with angle φ with respect to the x-axis and let the phase difference of the roboarm be $\theta = \varphi - \gamma$. Let the simulation run

3.1. Simulation Setup

from t_{start} to t_{stop} . Then the work specifies as

$$\begin{aligned} W &= \int F_{\perp}^{\text{sim}} dr = R \int F_{\perp}^{\text{sim}} d\varphi = R \int_{t_{\text{start}}}^{t_{\text{stop}}} F_{\perp}^{\text{sim}}(\theta(t')) \frac{d\varphi}{dt} \Big|_{t=t'} dt' \\ &= kR^2 \int_{t_{\text{start}}}^{t_{\text{stop}}} \sin(\theta(t')) \dot{\varphi}(t') dt' \end{aligned} \quad (3.5)$$

Note that the integrand only depends on the change of angle $\dot{\varphi}$. The starting alignment $\varphi(t = t_{\text{start}})$ can be set arbitrarily. After rotation, the work W done by the traps is then absorbed by the roboarm as energy $U = -W$.

3.1.3. Overview of Joint Variations

The joint consists of two ssDNA sections of the scaffold, the spring domain and the pivot domain, and is placed in the middle of the baseplates (see Fig. 3.3a)). The rotation of the roboarm results in winding-up of the joint, as the spring domain rotates around the pivot domain. The pivot domain has a fixed length of 3 nucleotides, whereas the length of the spring domain was varied to be either 3, 7, 13 or 23 nucleotides long (see Fig. 3.3b)). Note that the sequence of the 23nt spring domain contained a hairpin, which could effectively shorten the spring down to the 13nt spring domain.

The range of the nanorobotic arm motion is defined as the maximal cumulative angle from stop to stop. Since a longer spring domain could wrap more often around the pivot domain, it is expected that the range of motion increases with spring length.

From now on, the pivot domain will not explicitly be mentioned when referring to a specific joint, since its length stayed constant throughout all simulations (e.g. the 7nt-joint refers to the joint with a 3nt long pivot domain and a 7nt long spring domain).

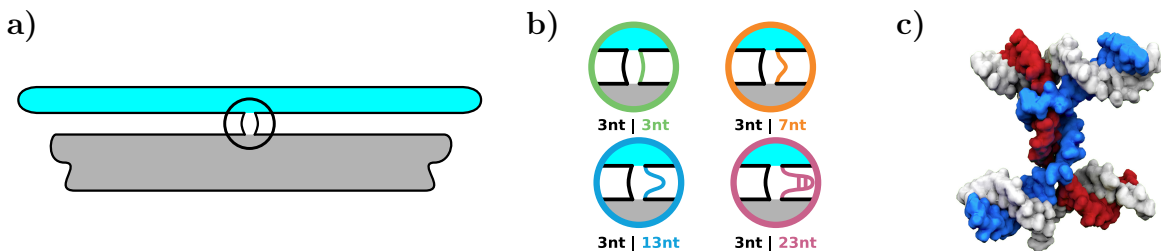


Figure 3.3. | Different Joints. **a**, sideview of simulated roboarm-structure, with the arm colored in blue and the baseplate colored in grey. The joint is encircled. **b**, overview of all joints that were simulated. The pivot-domain is colored in black. Note that the pictogram for the 23nt-joint should emphasize the hairpin that has formed. **c**, molemap of the 13nt-joint when wound-up, with the spring-domain colored in blue and the pivot-domain colored in red.

3. Simulation of Joint

3.1.4. Relaxation of Joint Variations

For the simulation we use a fully relaxed and unwound joint as starting configuration. For comparability, the starting configuration of all different joints should be as similar as possible. To do so, the relaxed starting configuration of the 3nt-joint was copied for the 7nt-, 13nt- and 23nt-joint. Their spring lengths were updated accordingly by inserting the corresponding number of nucleotides using oxDNA-Viewer [53], without changing the topology or configuration of the baseplate and roboarm. After insertion, the structure again was relaxed. During this relaxation, the rotating-harmonic-traps were already implemented, but with rate $\dot{\gamma} = 0$ and an increased total stiffness of $k = 3.4 \times 10^3 \text{ pN nm}^{-1}$. Implementing these static traps relaxation guarantees that the roboarms for all joints will stay aligned in the same direction, regardless on whether they were relaxed independently of each other. It also ensures that the joint will not spontaneously wind up during relaxation.

3.1.5. Theoretical Dynamics of Skipping

Running the simulation with rotating-harmonic-traps with non-zero rates, the traps cause the roboarm to rotate. Constant rotation will result in the spring domain to wind up around the pivot domain. A resetting torque builds up, as the spring domain has finite length and can therefore only wind around a limited number of times. The roboarm starts lagging behind as the phase-difference δ between the roboarm and the trap increases; the roboarm stalls, as the resetting torque increases and thereby cancelling out the torque exerted by the trap. Eventually the roboarm can no longer follow the trap: back-skipping occurs. Here the roboarm unwinds again, by rotating one full revolution in the opposite direction until it can follow the trap again. This happens when the torque applied by the traps reaches its maximum and starts declining with increasing phase difference. Eq. 3.4 implies, that the maximal torque that can be applied occurs at a phase-difference $\theta = \pi/2$. Without any diffusive motion (e.g. at temperature $T = 0 \text{ K}$), skipping is then expected to occur at a phase-difference of $\pi/2$. The skipping event is schematically shown in Fig. 3.4.

3.1.6. Simulation Parameters

All simulations were done using oxDNA2 running on CUDA [54]. The temperatures in the simulations was set to $T = 20 \text{ }^\circ\text{C}$ using the *john*-thermostat (see 2.8.2). The timestep was set to $dt = 0.005$ which corresponds to 15.2 fs per simulation step. Larger values for dt resulted in the simulation to diverge, smaller values were unpractical as the simulation would run too slow. In the simulation, the current configuration was printed out and appended to the trajectory every 100 000 steps which corresponds to every 1.52 ns. Salt-concentration was set to 1 M. The random-seed was defined to the same value for all simulations.

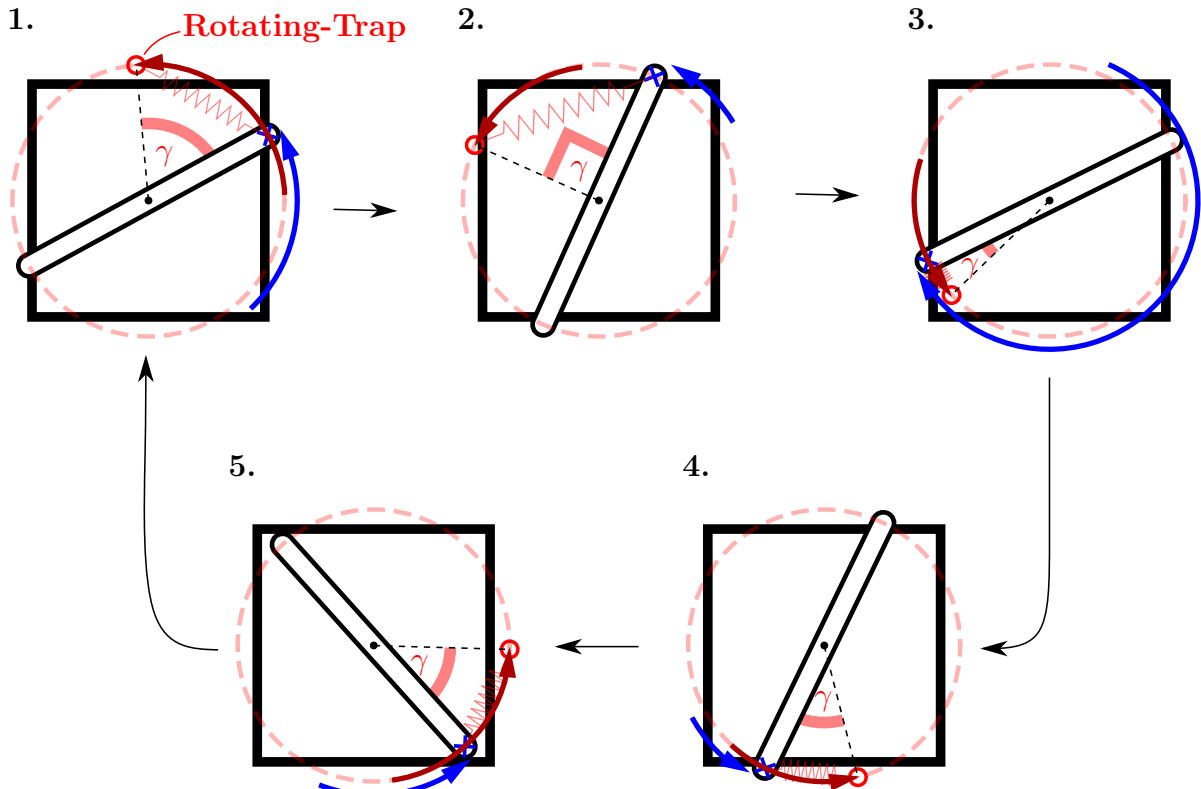


Figure 3.4. | Skipping. Dynamics of skipping is shown. As the trap keeps rotating in counter-clockwise (CCW) direction, but the joint is wound up to its limit. The arrows show the change of angle relative to the previous shown step, for the rotating trap (red) and the angle of the arm (blue). In 1, the arm still follows the rotating trap, but the resetting torque increases as the joint is being wound up, thereby slowing down the rotation of the arm. In 2, the trap is perpendicular to the arm. Thus, the exerted torque of the trap is maximized. However, as the angle between the trap and the arm continues to rotate, the exerted torque of the trap decreases and becomes smaller than the resetting torque of the joint. Thus, the arm unwinds again (in clock-wise direction), until the resetting force equals the exerted torque of the rotating trap. This event is called *backskipping* and is shown in 3. In 4 and 5, the phase difference between the angles of the arm and the rotating trap increases, as the joint is again being wound up in counter-clockwise direction, until the configuration in 1 is again present.

3. Simulation of Joint

3.1.7. Simulations Types

In the scope of this thesis, there were three types of simulations performed:

- **Twist:** Here the rotating-harmonic-traps with $k = 0.30 \text{ pN nm}^{-1}$ were rotating in counter-clockwise (CCW) direction with a rate of $\dot{\gamma} = 6.6 \text{ rad } \mu\text{s}^{-1}$ (1 revolution $\cong 0.95 \mu\text{s}$). This type simulates the constant rotation of the electric field.
- **Hold:** Here the rotating-harmonic-traps with $k = 0.30 \text{ pN nm}^{-1}$ are stationary, so that $\dot{\gamma} = 0$. This simulation becomes important to verify that the rotating traps from the twist-simulation follow quasi-static motion with respect to diffusion of the roboarm and thus do not impact the dynamics of the joint.
- **Untwist:** Here the simulation was started from a wound-up configuration with the rotating traps deactivated ($k = 0$), so the roboarm could freely rotate and the joint could relax, without the influence of external fields. This is not to be confused with the relaxation done prior the simulation, as here the roboarm is still simulated with the physically most accurate model of oxDNA.

3.2. Results

This section presents the results obtained by the simulations. The results are subdivided in three categories:

- Comparing the windup process of all joints at fixed rotation speed of the traps
- Comparing the windup process of the 3nt-joint with one slow, and one fast rotating trap
- Comparing the unwind process with the windup process of the 13nt joint

3.2.1. Windup with constant rotating traps

Range of Motion

The range of motion (RoM) indicates how far the roboarm can rotate. As already stated in Subsection 3.1.3, a longer spring domain is expected to enable a greater range of motion. To verify this hypothesis, twist-simulations were run for all four joints. The cumulative angle of the roboarm from these simulations is plotted in Fig. 3.5a). Note that the absolute angle of the roboarm is composed by the averaged angle of all 6 nucleotides to which traps were attached to, with respect to the pivot point of the rotating traps. Since only the cumulative angle is of interest, the reference absolute angle can be set arbitrarily. For comparability, all cumulative angle trajectories were aligned so that the absolute angle of the roboarm in the start-configuration at $t = 0$ was the same for all four

3.2. Results

joints. Furthermore, the rotating-harmonic-traps coincide at $t = 0$ with their associated nucleotides on the tip of the roboarm.

As can be seen in Fig. 3.5a), the cumulative angle does not constantly increase, but reaches a maximum. This is the case for all 4 joints, however, already from the trajectories it becomes apparent, that a longer spring-domain generally also implies a greater maximum of the cumulative angle, as for example the 23nt-joint rotates further ($\approx 12\pi$) than the 3nt-joint ($\approx 6\pi$). The trajectories also show, that the first-skip event as well increases with spring-length. Finally, the trajectories for all 4 joints show the high stochastic nature of the skipping events. Before the first-skipping event, the cumulative angle shows little fluctuations while following the traps. However, once skipping occurs, larger variations of cumulative angle emerge. This can be seen for the 23nt-joint, as here a decreasing trend in the cumulative angle of $\approx -5\pi$ (between 7.5 μ s – 12.5 μ s) is present, whereas an increasing trend of $\approx +5\pi$ appears towards the end of the simulation (between 23 μ s – 26 μ s).

In Fig. 3.5b), the RoM for all joints is plotted in a swarmplot. Note, that the RoM is defined as double the maximum cumulative angle from the trajectories. This is because in the simulations, the roboarm was only rotated in CCW-direction, starting from a relaxed position with the joint unwound. It is assumed that a rotation in CW-direction results in the same magnitude of cumulative angle as in CCW-direction. Thus, when starting from neutral position, the maximum cumulative angle in either direction only yields half of the actual RoM.

Fig. 3.5b) indeed visualized the trend, that an increase of spring-length correlates with an increase of RoM as well. However, this trend is not as steady as expected, since the 7nt-joint shows similar RoM compared with the 13nt joint. A standard deviation of 2.0π averaged over all joints again demonstrates the strong fluctuations of the RoM, as already pointed out for the trajectories.

Note also, that the first skipping event is highlighted for every joint in Fig. 3.5b). The data points suggest a linear relation between the time of the first skipping event and the joint length, however, the simulation must be repeated multiple times to get more data points to verify this relation.

There were snapshots of the joint taken at positions $\varphi \in \{3.4\pi, 5.1\pi, 7.8\pi\}$, shown in Fig. 3.5c). They show the multidimensional-scaling-mean (MDS) [53] taken from all hold-simulations. These snapshots were only shown for the joints before the first skip-event occurred, which is the reason why the 3nt- and 7nt-joint do not have snapshots starting from $\varphi = 5.1\pi$ and $\varphi = 7.8\pi$ respectively. The snapshots show an extension of the pivot-domain, as multiple bases from the baseplate and the roboarm are pulled into the joint. This extension can already be seen for $\varphi = 3.4\pi$ for the 23nt-joint. Furthermore, the topologies for the 7nt-joint at $\varphi = 5.1\pi$ and for the 13nt-joint at $\varphi = 7.8\pi$ have changed, as the spring-domain seems to miss one winding around the pivot domain, compared with other snapshots at the same positions, but longer spring-domains.

3. Simulation of Joint

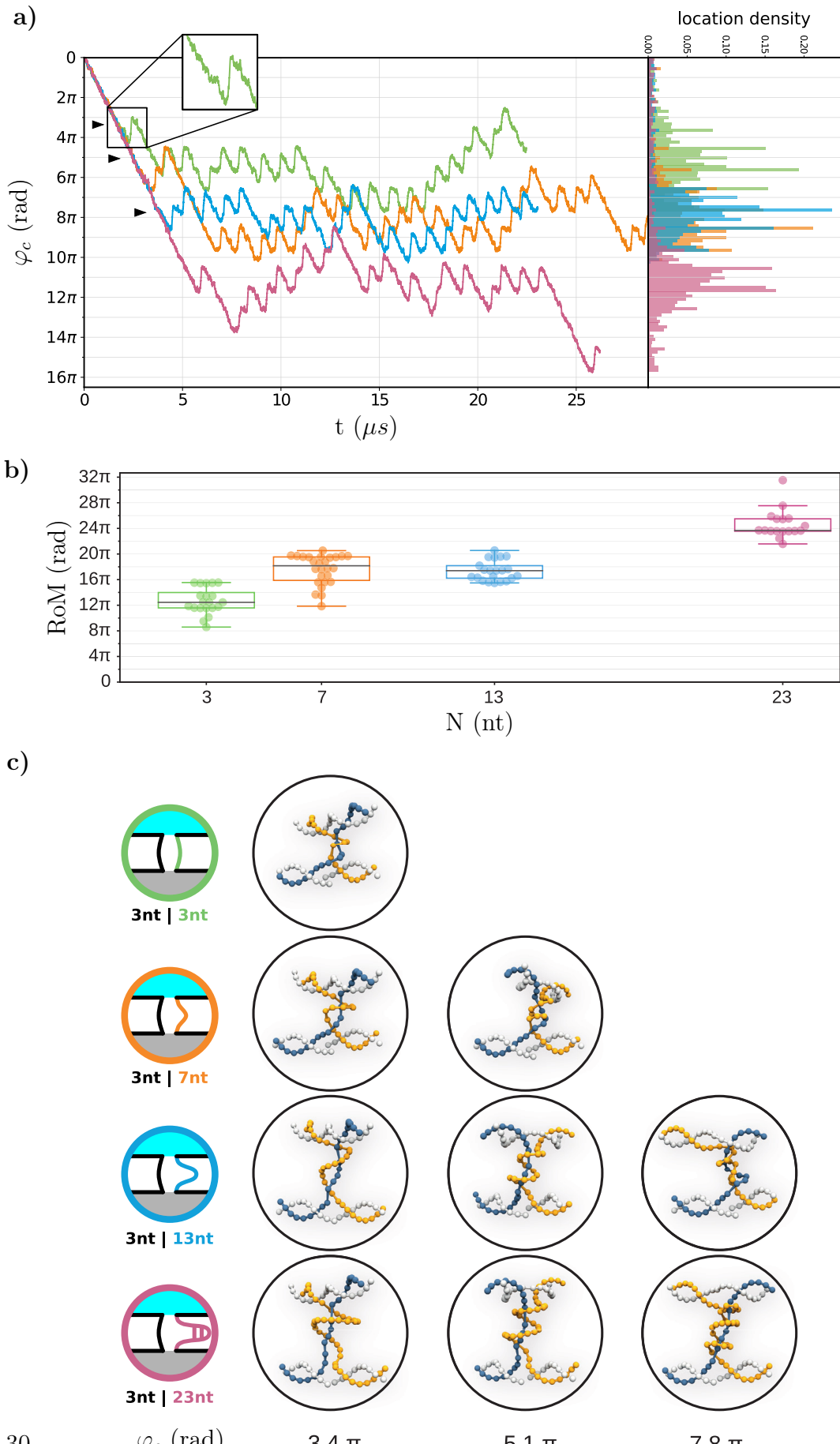


Figure 3.5. | Trajectories of Cumulative Angle. **a**, cumulative angle during wind-up simulation in counter-clockwise direction for all four joint variants. On the right side is the histogram shown, for the cumulative angle during simulations. **b**, shows the range of motion for all four joints with respect to the spring-length. **c**, MDS-mean from last 1000 configurations of hold-simulations that were performed at the angles marked as triangles in the plots shown in **a**.

Skipping

As a skipping event occurs, the phase difference between the cumulative angle of the roboarm and the cumulative angle of the force increases by a full revolution (2π rad). This cumulative phase difference is shown in Fig. 3.6a). For the 23nt-joint, one can see the cumulative phase difference gradually increasing in the first 6.1 μ s of the simulation before skipping eventually occurs.

The skipping events are defined as the local maxima of the trajectories from Fig. 3.5a). The absolute phase difference at the skipping events is then given by the cumulative phase difference modulo 2π rad and is shown in Fig. 3.6b). Note the phase difference at skipping never exceeded $\pi/2$ rad as the maximum phase difference is given by the 3nt- and 7nt-joint with 0.495π rad $\cong 89.1^\circ$. The mean phase difference at skipping averaged over all joints is $\overline{\varphi_a}(t_{\text{skip}}) = 0.37\pi$ rad $\cong 67.0^\circ$, with standard deviation of 0.06π rad $\cong 10.2^\circ$.

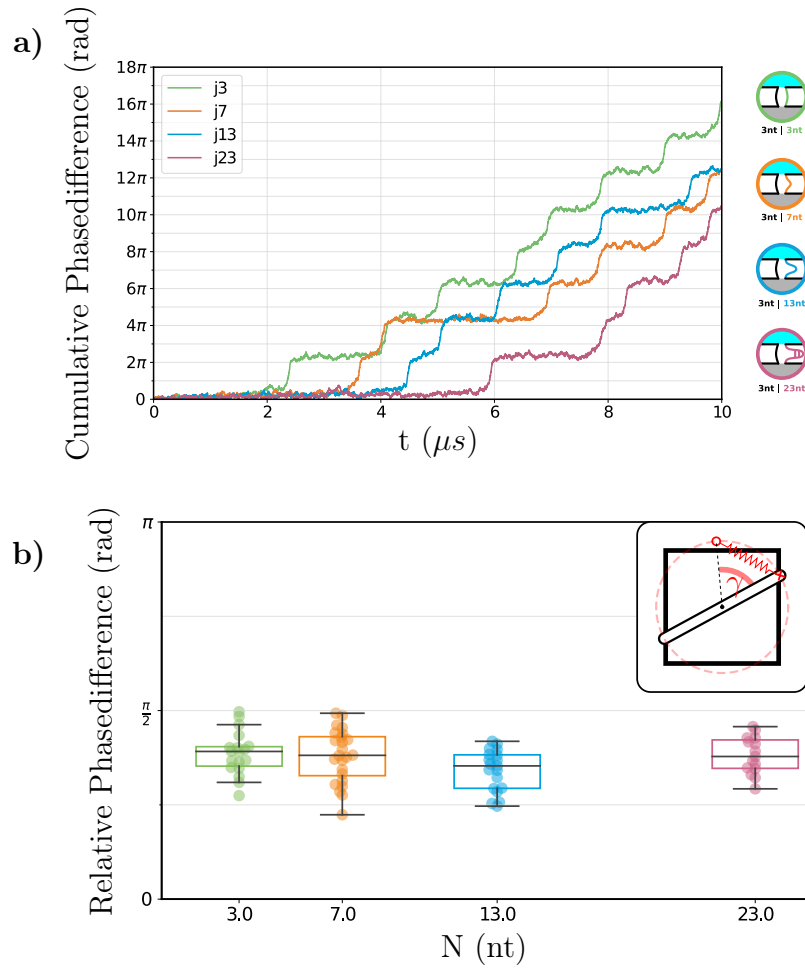


Figure 3.6. | Phase at Skipping. a, cumulative phase difference of the arm relative to the rotating trap for the first 10 μ s. b, relative phase difference at skipping events for all recorded skipping-events from the trajectory.

3. Simulation of Joint

Backbone force

This section analyzes the stress applied on the spring-domain, specifically the interactions between neighboring nucleotides. As introduced in Section 2.8.1, there are three force-types that model interactions between neighboring nucleotides in oxDNA: backbone-force, stacking-interactions and excluded-volume-interactions. In this thesis, only the backbone force for the spring-domain was analyzed.

The backbone force depends on the distances of the backbone positions of the neighboring nucleotides. It is evaluated by the derivative of the FENE-potential. The FENE-potential ensures an equilibrium distance between neighboring nucleotides so that the backbone connectivity is maintained [49]. In the oxDNA2 version used in this thesis, the FENE-potential was defined as

$$V_{\text{FENE}}(r, \epsilon, r^0, \Delta) = -\frac{\epsilon}{2} \ln \left(1 - \frac{(r - r^0)^2}{\Delta^2} \right) \quad (3.6)$$

and was parametrized with

$$\begin{aligned} \epsilon &= 2 \cdot 41.42 \text{ pN nm} = 82.84 \text{ pN nm} \\ \Delta &= 0.25 \cdot 0.8518 \text{ nm} = 0.213 \text{ nm} \\ r^0 &= 0.7564 \cdot 0.8518 \text{ nm} = 0.644 \text{ nm}. \end{aligned} \quad (3.7)$$

The FENE-potential and corresponding backbone force are shown in Fig. 3.7.

In Fig. 3.8a), the mean distance of neighboring nucleotides in the spring domain of all joints $\bar{R}_{\text{BB}}(\varphi_c)$ is plotted over the cumulative angle φ_c , up until the first skip event of the corresponding joint. The mean distance was averaged over all neighboring nucleotides of the spring domain. Hence, the mean distances for the 3nt-joint were averaged only over two bonds, whereas the 23nt-joint was averaged over 22 bonds.

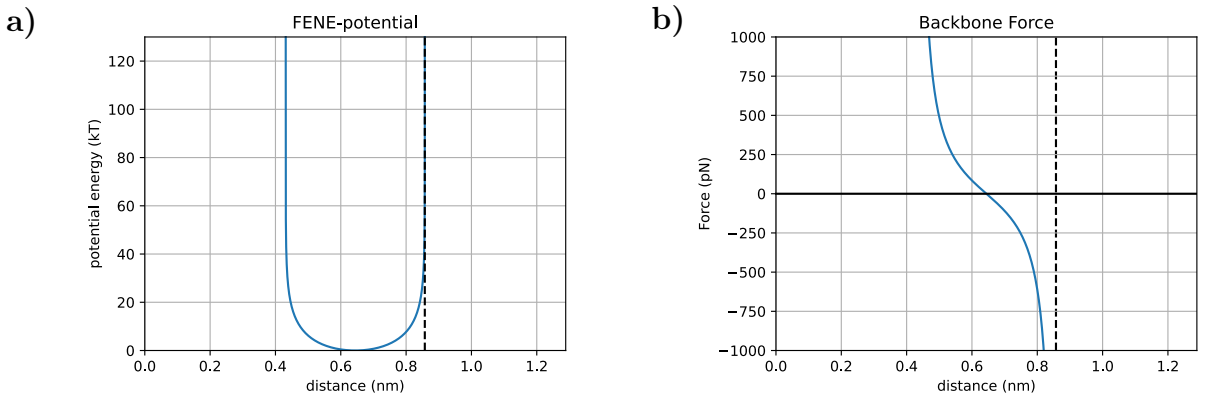


Figure 3.7. | Backbone Force in oxDNA. a, FENE-potential that models the backbone interaction. b, resulting backbone force between neighboring nucleotides. The dashed line represents the asymptote at $r^0 + \Delta = 0.857 \text{ nm}$.

3.2. Results

All spring-domains start with a mean backbone distance between 0.640 nm – 660 nm at beginning of the simulation at $\varphi_c = 0$. After wind-up, the mean backbone distance converges to ≈ 0.800 nm.

Regardless the joint, the mean backbone distances between the nucleotides show two distinct sections: The first section is defined for small cumulative angles. Here the backbone is not being stretched and fluctuates around ≈ 650 nm. The second section follows, in which the mean backbone distance increases first linearly with increased angle, until it saturates while approaching the first skipping-event.

An increase in of spring length correlates with an increase in duration for the first section as well: The first section for the 3nt-, 7nt-, 13nt-, 23nt-joint terminates at 2 rad, 6 rad, 8 rad, 15 rad respectively.

Up to now, only twist-simulations were analyzed. However, the dynamics of the winding-up could have influenced the backbone-distances. To support the backbone distances obtained from the twist-simulations, hold-simulations were performed for $\varphi_c \in \{3.4\pi, 5.1\pi, 7.8\pi\}$ for all joints, which are plotted in Fig. 3.8b). The hold-simulations run for at least 2000 configurations. Analyzation was performed over the last 1000 configurations of the trajectory.

The backbone force F_{BB} as shown in Fig. 3.8c) is then evaluated as

$$F_{\text{BB}}(\varphi_c) = (F_{\text{FENE}} \circ \bar{R}_{\text{BB}})(\varphi_c). \quad (3.8)$$

As for the distances, only forces up to the first skip-event were taken into consideration.

Similarly to the backbone distances, the backbone forces for the twist- and hold-simulations comply with each other. All joints experience neglectable backbone force at $\varphi_c = 0$. With increasing φ_c , the backbone force increases as well, until it saturates at ≈ 600 pN.

Errorbands for the backbone force were calculated using the same method as for the backbone distances, combined with gaussian propagation of uncertainty:

$$\Delta F_{\text{BB}}(\varphi_c) = \frac{dF_{\text{FENE}}(\bar{R}_{\text{BB}})}{d\bar{R}_{\text{BB}}} \Delta \bar{R}_{\text{BB}}(\varphi_c), \quad (3.9)$$

where $\Delta \bar{R}_{\text{BB}}$ is the error of backbone distance.

Comparing the backbone forces with the backbone distances, here also two sections become visible. In the first section, the backbone forces stay relatively constant with respect to φ_c . In the second section, the backbone forces are steadily increasing, until reaching the maximum backbone force. The second region starts for the 3nt-, 7nt-, 13nt-, 23nt-joint at approximately π , 2π , 4π , 6π respectively. Saturation as for the backbone distances could not be seen near the first skip-event of the backbone forces.

3. Simulation of Joint

Compared with the other joints, the 3nt-joint shows particular fluctuations in the trend: At first, the backbone force steadily increases, until it abruptly declines between $2\pi - 2.8\pi$, after which it rises again. All other joints show rather monotone increase of backbone-force.

Energies

Using the analyzation tool DNAAnalysis that comes along with the installation of oxDNA, the energies of the joint-only trajectory during the twist-simulation was analyzed and splitted up into its elementary parts. A sample input-file that uses was used for simulation with oxDNA and analyzation with DNAAnalysis can be found in Appendix A.2.

The energies are shown for all four joints separately in Fig. 3.9. Each energy contribution increases as the joint is being wound up. Sudden step-like changes are observed for energy-contributions for coaxial-stacking, hydrogen-bonding, crossstacking. These changes are caused by breaking of base-pairs.

The energy term for nonbonded excluded volume and for the backbone-interactions gradually increase for all joints. This is caused as the spring-domain continuously winds tightly around the pivot-domain and thereby generating a repulsive interaction and stretching the backbone.

Note that the energies in Fig. 3.9 refer to the partial structures that are shown in Fig. 3.5c), not for the pivot- and spring-domain only. Interactions in the joint are therefore averaged over the remaining nucleotides of the partial structure. This gives insights into the stability of the staples that are in the local environment of the joint.

3.2. Results

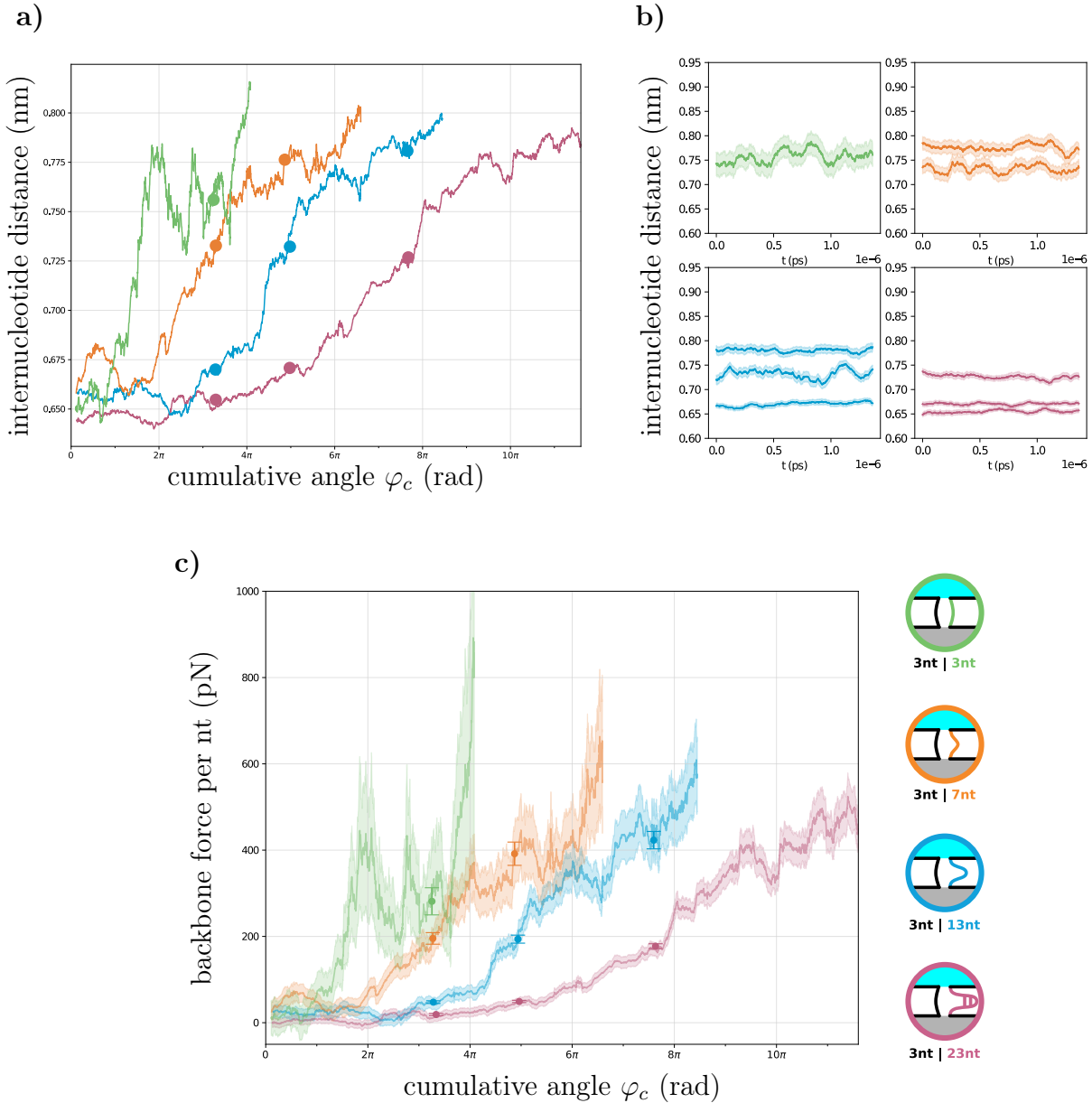


Figure 3.8. | Internucleotide-interaction of Spring-Domain. **a**, distance between two adjacent nucleotides in the spring-domain during wind-up, smoothed with a rolling window over the last 100 configurations, averaged over every nucleotide in the spring. The scatter-points show the mean of hold-simulations, that were started separately at corresponding time-points. **b**, distance between two adjacent nucleotides in the spring-domain during hold-simulations, smoothed with a rolling window over the last 100 configurations and averaged over every nucleotide in the spring. The error-bands show the standard error of the rolling window. **c**, backbone forces between two adjacent nucleotides in spring-domain, obtained by applying the force-function, which is the gradient of the FENE-potential, to the backbone-distances from **a**. The error-bands show the standard-error that follow from error propagation of the standard-error of the rolling window from the backbone-distances. The scatter-points show the backbone-forces for the hold-simulations. The error-bars show the double standard-error of the hold-simulations.

3. Simulation of Joint

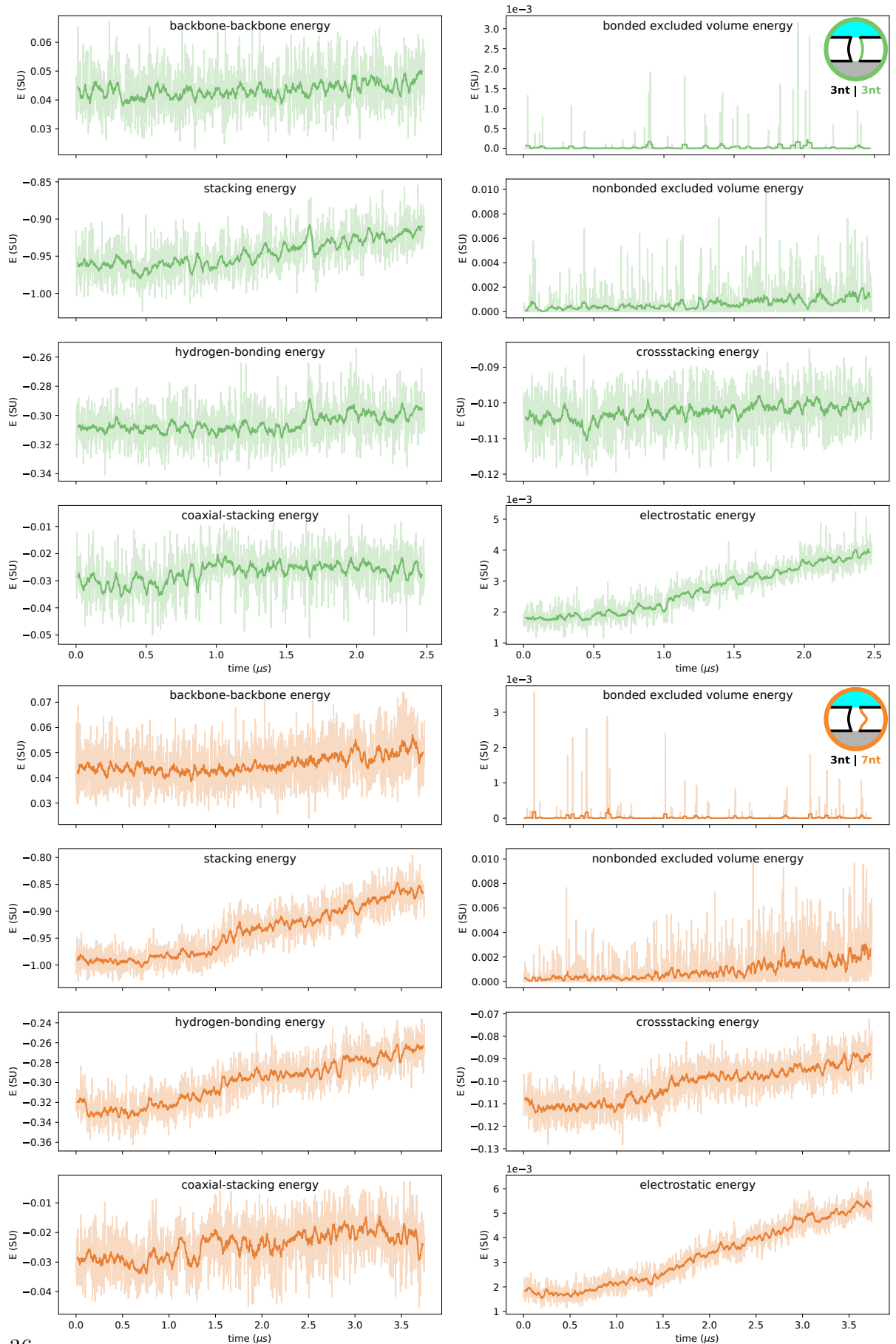


Figure 3.9. | Internal Energy. Energy contributions obtained from the tool DNAAnalysis. Solid line shows moving average over 20 data points. Raw data is shown by shaded region. Energy is given in oxDNA simulation units.

3.2. Results

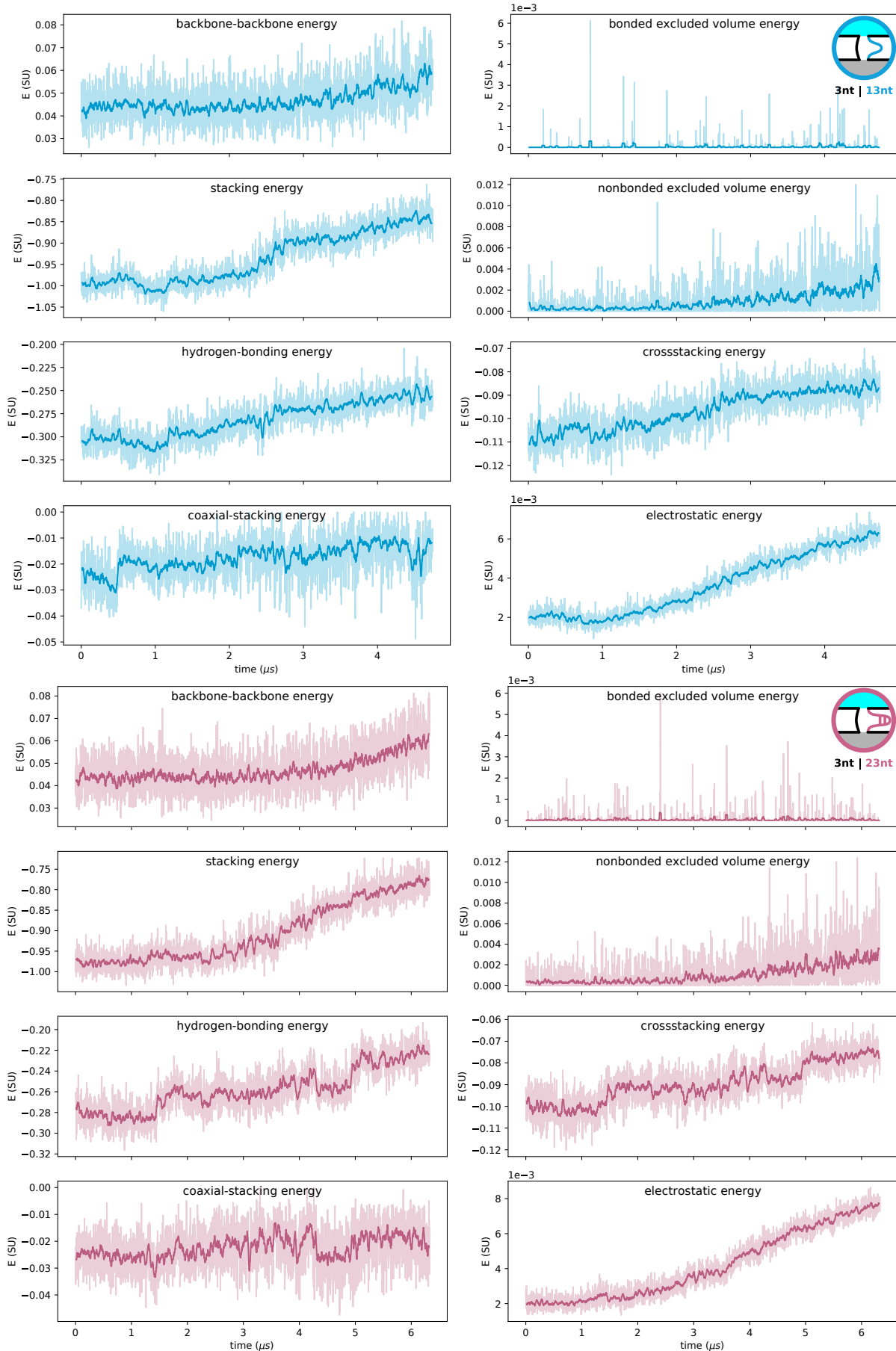


Figure 3.9. | Internal Energy. Energy contributions obtained from the tool DNAAnalysis. Solid line shows moving average over 20 data points. Raw data is shown by shaded region. Energy is given in oxDNA simulation units.

3. Simulation of Joint

Besides the internal representation of all energy contributions to the joint, the energy stored in the joint was compared to the energy stored in a torsional spring. A torsional spring applies a resetting torque M proportional to the angle of twist φ_c . The linear dependence is described by the torsion coefficient κ . The torsional spring stores potential energy U when twisted. It follows that

$$M = -\kappa\varphi_c \quad (3.10)$$

$$U = \frac{1}{2}\kappa\varphi_c^2 \quad (3.11)$$

It is expected that a more flexible joint leads to lower κ and thus stores less energy.

The energy stored in the joint was inferred by the work performed by the rotating traps. The mechanical work $U(\varphi)$ performed by the trap was evaluated using Eq. 3.5 and can be seen in Fig. 3.10. Again, datapoints only up to the first skip event were taken into consideration.

All energy profiles show parabolic character and were fitted by

$$U^*(\varphi) = \frac{1}{2}C_1\varphi^2 + C_2\varphi. \quad (3.12)$$

The function $U^*(\varphi)$ resembles the energy stored in a torsional spring (see eq. 3.10) in addition with a linear factor C_2 , that includes drag-related work. The fitted functions are plotted as dotted lines in Fig. 3.10. The fitting parameters are listed as follows:

Spring Length (nt)	C_1 (pN nm rad $^{-2}$)	C_2 (pN nm)
3	5.1	4.0
7	2.8	18.0
13	2.2	16.6
23	1.6	14.5

3.2.2. Windup with different rate for 3nt joint

The twist-simulation was also done with a 5-times faster rotating trap with a frequency of ≈ 5 MHz. As can be seen in Fig. 3.11, the maximal cumulative angle for the faster rotating roboarm (33 rad μ s $^{-1}$) is decreased down to 4π . Thus, rotating the roboarm at a slower frequency (6.6 rad μ s $^{-1}$) returns one more winding. Also note, that the slope of the cumulative angle, when following the trap, is 5-times as steep. Thus, the first skip-event is reached at an earlier point in time.

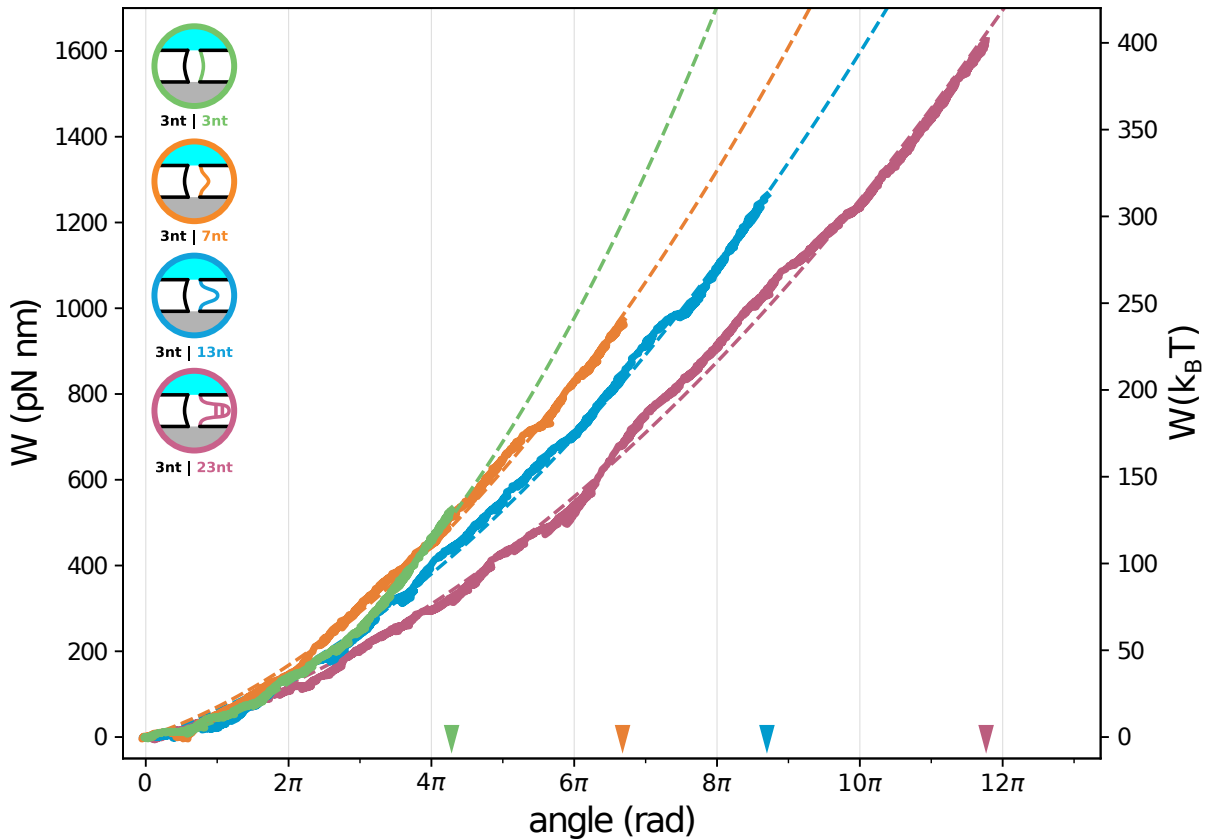


Figure 3.10. | Energy Storage. Work performed by the traps, thereby storing energy in the joint. Solid lines correspond to raw values of the work, dashed lines correspond to the fit-function form Eq. 3.12. The plots are only shown for angles the first skip-event occurred. The first skip-event is depicted as triangles.

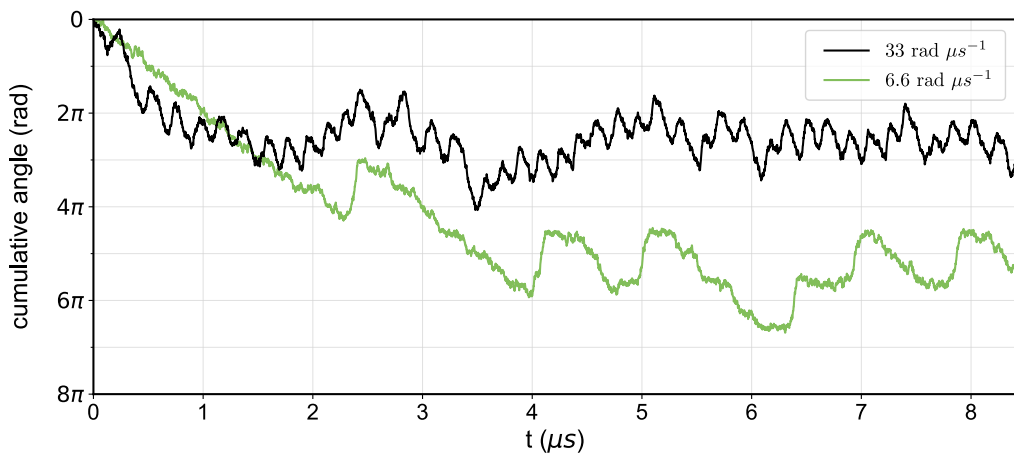


Figure 3.11. | Twist at different rates. Trace of the wind-up simulation for the 3nt-joint with the trap rotating at $6.6 \text{ rad } \mu\text{s}^{-1}$ in black and, unlike the other twist-simulations showed in this thesis, at $33 \text{ rad } \mu\text{s}^{-1}$ in green.

3. Simulation of Joint

3.2.3. Unwind of 13nt joint

The unwinding of the wound-up 13nt-joint in absence of external forces was also simulated. For that, the last configuration of the trajectory from the twist-simulation defined the starting point for the untwist-simulation. Finally, the trajectory of the untwist-simulation was appended to the twist-simulation and can be seen in Fig. 3.12.

At the start, a constant rate of unwinding can be seen from 23 rad down to 8 rad with a slope of $-15 \text{ rad } \mu\text{s}^{-1}$. From this follows that unwinding happened ≈ 2.3 times faster than the simulated wind-up.

Furthermore, it can be seen that the joint was fully unwound at $t = 36 \mu\text{s}$, but then spontaneously winds up again up to 1 revolution.

In Fig. 3.13 the backbone forces for the spring domain is plotted for both, the twist- and the untwist-simulation. A hysteresis was not seen, as both simulations showed a similar backbone force with respect to the angle. Note that only datapoints up to the first skip-event were regarded for the twist-simulation.

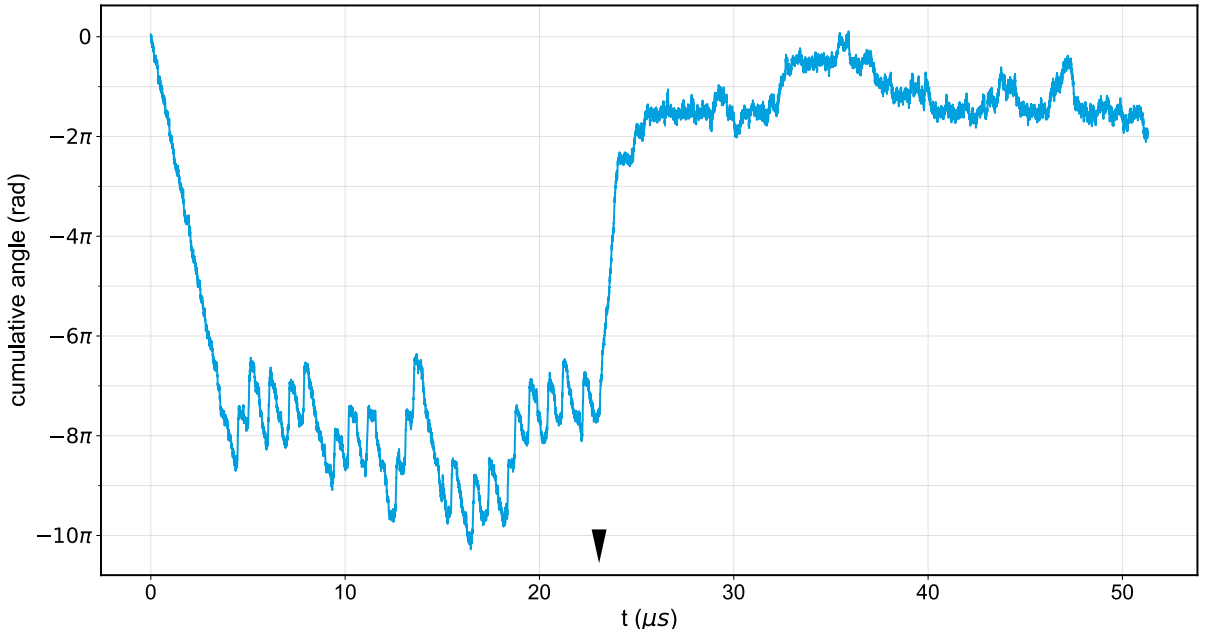


Figure 3.12. | Trajectories of untwist simulation. The combined trace of a twist simulation, followed by an untwist simulation, performed on the 13nt-joint roboarm structure. The black triangle shows the point in time when the untwist simulation was started.

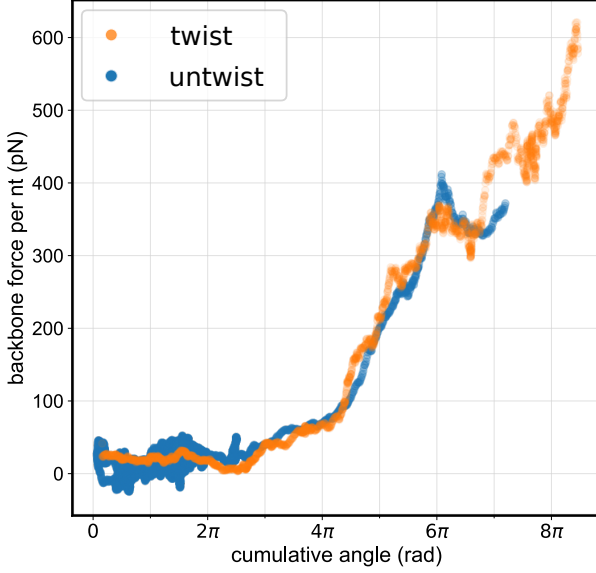


Figure 3.13. | Backbone forces for untwist simulation. The backbone forces during twist- and untwist-simulations performed on the 13nt-joint structure were evaluated by the backbone distances that were averaged over 100 data points. The backbone forces for the twist simulation are only shown for the datapoints up to the first skip-event.

3.3. Discussion

3.3.1. Range of Motion

An increase of spring-length correlates with an increase of RoM, as shown in Fig. 3.5b). A longer spring-domain is able to wrap more times around the pivot domain, thus increasing the RoM. This intuitive concept is verified when observing the snapshots from Fig. 3.5c). However, the spring-length, which was assumed to stay constant, changes under stress of the joint: the length of the pivot domain increases. Since the snapshots are based on the MDS taken from the hold-simulations, the extension of the pivot-domain cannot be explained as a result of the high dynamics of the twist-simulation, and nor is a rare event. As the extended pivot domain can already be observed for the 23nt-joint at $\varphi_c = 3.4\pi$, where the joint did not experience much stress since the backbone forces are neglectable (Fig. 3.8c)), the extension can be explained by an unstable staple choice around the joint. On the other hand, the 3nt-joint did not show an extension of the pivot domain, despite being under more stress. This can be explained by the equally sized spring domain, which gives additional support to the joint.

The topological changes seen in the snapshots in Fig. 3.5c) for the 7nt-joint at $\varphi_c = 5.1\pi$ and the 13nt-joint at $\varphi_c = 7.8\pi$, which become apparent due to the missing turn of spring domain, result from an artifact by the MDS-mean. The artifact is caused by the strong fluctuations of the trajectory of the joint. Other methods, e.g. computing the mean structure, did not improve the snapshots.

3. Simulation of Joint

The trend of an increasing spring domain resulting in an increased RoM does not hold true for the 7nt-joint and the 13nt-joint. This is probably due to poor statistics. This assumption is supported by the disproportionately high standard deviation of the RoM of the 7nt-joint. A more obvious trend is expected if running the simulations for a larger timescale and/or repeating the simulations multiple times.

Notice that the RoM strongly depends on the angular velocity of the rotating traps $\dot{\gamma}$ (Fig. 3.11). When the traps are rotating slower, the roboarm can more easily follow the traps and hence rotate for longer, increasing the RoM. Without inertia and diffusion, $\dot{\gamma}$ should not have influence on the RoM. As can be seen by the short-term fluctuations of the trajectories in Fig. 3.5a), diffusion overweights inertia.

When simulating with traps rotating at extraordinary high frequencies, their high-speed motion did not impact the characteristics of the joint itself. The mean backbone distances for the hold-simulations (Fig. 3.8b)) comply with the mean backbone distances from the twist-simulations (Fig. 3.8a)). Furthermore, the mean backbone forces obtained for the purely diffusion-driven unwinding-process (Fig. 3.13) superpose with the mean backbone forces for the winding-up process. This suggests that for the twist simulations the joint region itself may be treated as quasi-static. This also implies, that the structure of the joint itself is independent of motion.

However, as long-distance interactions are not realistically resembled in oxDNA, quasi-static motion of the whole arm cannot be assumed. The slope-ratio $\frac{\Delta\varphi_c^{\text{untwist}}}{\Delta\varphi_c^{\text{twist}}}$ = 2.6 of the cumulative angle during untwisting, relative to the cumulative angle of twisting, determined from Fig 3.12, suggests that the angular velocity of the traps are of same order as diffusive motion. Thus, quasi-static rotation cannot be assumed for the whole roboarm structure.

3.3.2. Comparing to real-world

Even though the simulations run on a timescale of microseconds, they do give insight into characteristics of the joint on a much larger timescale up to seconds for the real-world roboarm as well. For that, the diffusion of the roboarm in the real-world must be comparable to the diffusion in the simulations. When using electric fields for alignment, the real-world roboarm usually has a pointer attached to. This pointer significantly slows down the motion of the roboarm due to its stiffness and thereby resulting drag. Furthermore, one can use buffers with much higher viscosity to even further reduce diffusion of the real-world roboarm. When doing so, diffusion in real-world experiments is expected to be at least 3 orders of magnitude smaller and the simulations realistically predict the dynamics of the joint.

3.3.3. First Skip Linearity

Later emerging fluctuations of the cumulative angle during twist-simulations as pointed out for the 23nt-joint (see Sect. 3.2.1) arise, as the structure of the joint adapts to the stress of the wound-up joint, which leads to breaking of base-pairs. This effect accounts less up until to the first skip-event, as here the structure of the joint around the joint has not significantly changed (Fig. 3.5c)). Still, the cumulative angle approaching towards the angle of first skip leads to increasing stress to the joint.

When ignoring fluctuations of the RoM by only focussing on the datapoints up until the first skip-event, the RoM shows great linearity with respect to the spring-length (see fit in Fig. 3.5b). This leads to an oversimplified model of the joint, in which the spring-domain rotates with constant radius of $\approx 5.7 \text{ \AA}$ around the pivot axis, defined by the pivot domain which is assumed to be rigid with. This radius is smaller than the allowed minimal distance defined by the excluded volume interactions and can only be explained by the pivot domain not being rigid. Although oversimplified, this model shows compactness of the spring domain around the pivot domain. It should be stressed, that more twist-simulations up to the first skip-event of all joints are required for a more accurate spring-domain radius.

3.3.4. Skipping Phase

As proposed in Sect. 3.1.5, skipping is expected to occur at phase difference of $\pi/2$. This was not observed in the twist-simulations, as here skipping occurred before the theoretical maximum torque was reached (see Fig. 3.6b)).

This could be the result of arm-bending, The angle of roboarm is measured using the same nucleotides to which the traps are attached to. High torque could bend the arm, leading to a supposedly smaller phase difference than actually is the case and would explain the smaller phase at skipping. However, arm-bending is highly unprobable, as will be explained in Sect. 3.3.5.

Another reason could be the thermally driven diffusive motion of the roboarm. Suppose the roboarm has wound a number of times, so the spring domain exerts a resetting torque $M^{\text{joint}} = -k\varphi_c$, relatively constant against small variations of angle φ_c . With a phase difference increasing to the theoretical limit of $\pi/2$, diffusive motion leads to random fluctuations changing the angle and therefore the phase difference θ of the roboarm by $\pm\delta$. In the case the phase difference shrank by $-\delta$, the trap keeps rotating and the cumulative angle increases. However, when the phase difference increases by $+\delta$, the exerted torque of the traps declines by $\Delta M^{\text{trap}} = kR(\sin(\theta) - \sin(\delta))$, whereas the resetting torque of the joint stays constant. Depending on the number of windings, the resetting torque can now be greater than the torque exerted by the traps, so that $M^{\text{trap}} + M^{\text{joint}} < 0$, leading to skipping.

3. Simulation of Joint

This also explains, why smaller spring domains have a broader distribution with outliers closer to $\pi/2$, as here the fluctuations in angle have more influence on the resetting torque. In case a fluctuation causes an increase of phase difference $+\delta$, then the resetting force for smaller spring domains significantly decreases and skipping is not guaranteed to happen.

3.3.5. Forces/Distances

Stretching or even breaking of covalent bonds between neighboring bases requires very much energy, which is modelled by asymptotes of the FENE potential and is therefore not possible in oxDNA simulations. However, the backbone distances of neighboring bases can increase under stress, as the inter-atomar torsion angles of the nucleotides align for extension. A change of backbone distances therefore implies larger stress present. This was seen during the wind-up of the joint.

At the beginning, both the backbone forces and the backbone distances had a constant first section (see Fig. 3.8), in which their magnitude is invariant under the rotation of the roboarm. In this section, the joints are still relatively relaxed and the spring domain has not wound many times, if any, around the pivot domain. Thus, the spring domain still contains much slack, allowing the bases of the spring domain to stay in their resting position. Hence, the distances to their neighbors does not increase.

This also shows that the preparation (see Sect. 3.1.4) done before starting the twist-simulations was successful. If the joint would need to be further relaxed after updating the joint, an instant change of backbone distances at the beginning of the twist-simulations would be expected.

Note that the high fluctuations from smaller spring domains emerge, because the backbone distances between neighboring nucleotides was averaged over the spring domain; a longer spring domain provides more neighboring nucleotides to average over, and therefore is more robust against fluctuations of the individual nucleotides. Structural changes around the joint therefore also have higher influence on the average of the backbone distances for joints with smaller spring domains.

The linearity of the backbone forces in the second section confirms the assumption of the joint acting like a torsional spring, as latter is defined by a resetting torque directly proportional to the excursion. Flatter slopes correspond to lower torsion coefficients. Therefore, the measured backbone forces suggest a decline of the torsion coefficient κ with increasing spring length.

The linearity of backbone forces near the angle of first skip suggests that arm bending is not present. Otherwise, a saturation of backbone force would be expected, as the angle of the roboarm falsely increases, while the windings of the joint remain unchanged and thus also the backbone force.

However, the backbone distances close to the angle of first skip do flatten for all joints. This is a result from the non-linearity of the FENE-potential for neighboring distances close the asymptote.

It should be pointed out, that in this thesis only the backbone force resulting from the FENE-potential was studied. However, other interactions, e.g. volume excluding interactions of nucleotides, were ignored. Though the backbone forces between nucleotides are believed to have most influence on the resetting torque exerted by the joint, further analyzation of other interactions need to follow up for a more complete image on the joint.

3.3.6. Energy Storage

As shown with the untwist simulations, winding up the joint does not result in permanent structural changes. One can therefore store potential energy by winding up the joint. This energy can then be released in the form of kinetic energy by eliminating the driving forces. This was experimentally tested and verified by Vogt et al. [22].

The model in which the joint acts as a torsional spring is again confirmed when observing the energy profiles (see Fig. 3.10). Quadratic dependence C_1 on the stored energy U with respect to the cumulative angle φ_c complies with the theoretical expected energy profile (see Eq. 3.10)i. The energy profiles provide direct insight into the torsional spring coefficient $\kappa \equiv C_1$. As expected, an increase of spring domain leads to a weaker joint and thus a lower κ .

The linear dependency incorporated by C_2 suggests, that the arm is experiencing drag when being wound up. Given more simulation runs, the factor C_2 is expected to converge to the same value, regardless which joint is used. However, the factor C_2 does not influence the torsion coefficient.

However, an increase in stored energy with a larger spring domain was not expected. This is caused by two independent effects as a result of increased spring domain taking place simultaneously:

- The torsion coefficient κ decreases, suggesting lower stored energy.
- The RoM increases, so the joint can store more energy by doing more windings.

As it turns out, the second effect overweights the lower κ .

3.4. Conclusion

In this chapter, we used oxDNA to simulate multiple joint variations for our nanorobotic arm structure. Thereby we chose a constant pivot-length (3nt long) and varied the spring-length from 3nt – 23nt. Using the simulations, we investigate the limitations of

3. Simulation of Joint

these joints. We found that the range of motion of the joint scales with joint-length. When winding-up the joint, we observed structural changes in the joint as a response of increasing stress. We investigated the characteristics of skipping events that occur when the joint has completely wound up and the rotating trap keeps rotating. Furthermore, we investigated the dynamics of the joint when winding-up. Thereby we analyzed the backbone-forces between neighboring nucleotides in the joint as well as all potential energies contributing to the joint. We found that the increased backbone-forces are limiting the range of motion. Finally, we studied the energy stored in the joint during wind-up. For that we analyzed the work performed by the traps. We found that the energy stored in the joint agrees well with the energy stored in a torsional spring.

4. Simulation of the Pickup-Process

This chapter investigates the cargo transportation mechanism, introduced in Sect. 2.3, using massively paralyzed simulations in oxDNA. Since especially the pickup is critical for the successful cargo transportation, the main objective of the simulations performed in this chapter was to optimize the sequence dependency of the involved DNA-strands, so that successful pickup later in the experiments would be more probable.

Using simulations to optimize the strands has the advantage to focus on the dynamics of the pickup-process only, suppressing any other side-effects that may have had an influence and ignoring the challenges posed in the experimental implementation.

Although there exist simplified models describing the rates of rupture [27, 55, 56], there are yet no models describing multi-strand systems competing over rupture with each other under the influence of dynamics. Thus, using MD-simulations in oxDNA provide a straightforward and physically accurate approach.

For this thesis, three key factors influencing the dynamics of rupture were of interest:

- The dependence on applied force
- The dependence on different strand lengths
- Comparing competing rupture of multi-strand systems versus isolated rupture

The structures used for the simulations in this chapter represent the deposit- and pickup-handle that were used for the real-world roboarm in the experiments. The deposit-handle is a staple extension protruding from the baseplates. The pickup-handle is a staple extension located at the end of the arm. The experimental implementation will be described in more detail in Sect. 5.2.

4.1. Simulation Setup

4.1.1. Parent structure

The starting point of the simulation is defined by a parent structure, which represents the fundamentally relevant elements to simulate the cargo-transporting mechanism.

4. Simulation of the Pickup-Process

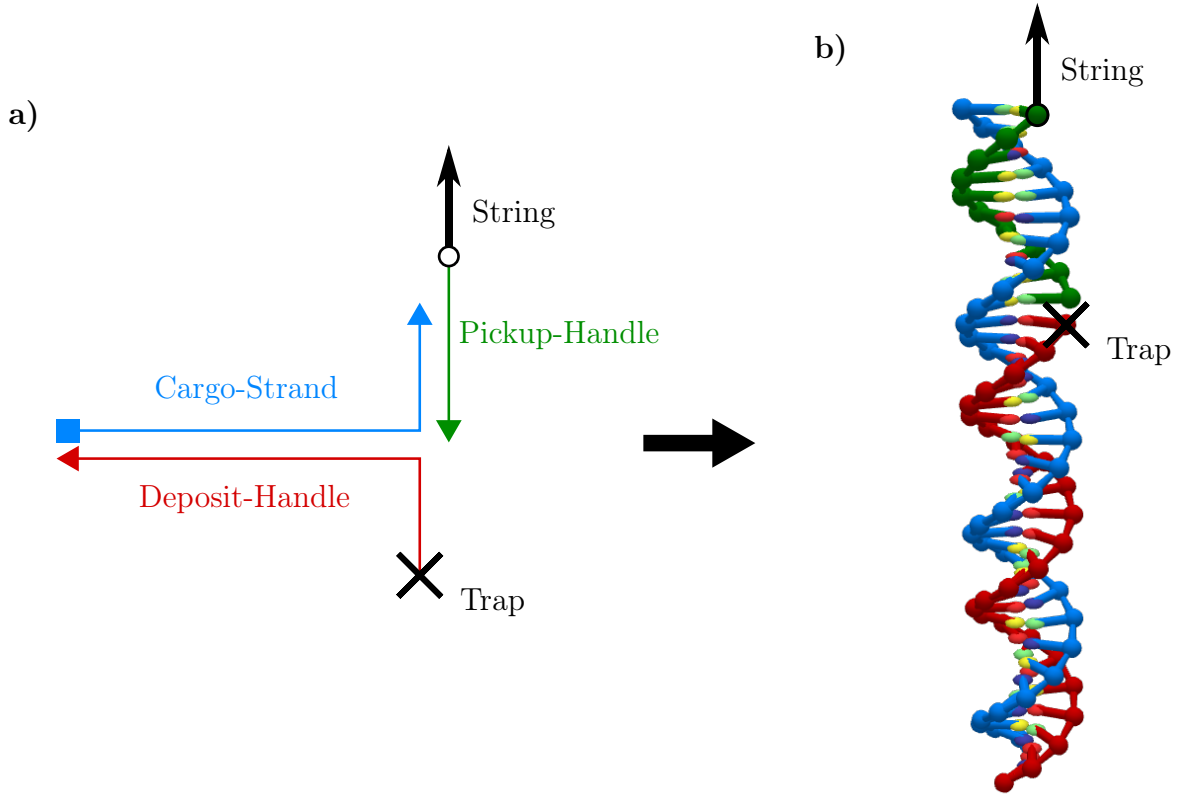


Figure 4.1. | Parent structure. All simulations were based on this structure. **a**, shows the secondary structure, where the 5'-end of the deposit-handle is fixated. In the experiments, this would be a staple extension from the baseplates. A string-force was assigned to the 5'-end of the pickup-handle, encouraging rupture. **b**, shows the same structure in the balls-and-sticks representation in oxDNA.

All simulations are based upon the same parent-structure, consisting of a three-strand-system arranged in a single double-helix. The longest strand should resemble the cargo-strand to be picked up. The cargo-strand is up to 35 bases long with intentional choice of high/low GC-content on specific regimes of the sequence. The cargo-strand has two segments to which at first both reverse-complementary strands are bound to: the deposit-handle and the pickup-handle.

Forces assignments (Trap, String, Repulsion plane)

The deposit-handle is fixated by using a harmonic-trap (see Sect. 2.8.3) assigned to one base at either the 3'- or 5'-end of the deposit-handle. Choosing one end defines whether unzipping or shearing will occur when the cargo-strand ruptures from the deposit-handle. When fixating the deposit-handle at the end which coincides with the end of the cargo-strand, then shearing would occur. For the purpose of this thesis however, the deposit-handle was fixated at the other end, in the middle of the cargo-strand (see Fig. 4.1), so that unzipping occurs when the cargo ruptures away, as would be the case in the

4.1. Simulation Setup

experiments later. The stiffness of the harmonic trap was set to $k = 4.86 \text{ nN nm}^{-1}$.

Similarly, a force was assigned to the end nucleotide of the pickup-handle, which coincides with the end of the cargo-strand, so shearing would occur upon rupture. Here, a string-force was used for the pickup-handle, which causes a constant force, regardless of the current position. The magnitude of force used in the simulations varied from $16.5 \text{ pN} - 20 \text{ pN}$.

With this setup, the cargo-strand is now being pulled apart: on one side the pickup-handle is constantly pulling in one direction while on the other side the deposit-handle is holding the cargo-strand back in place. Depending on the force with which the pickup-handle is pulling at, three scenarios can happen:

- **Cargo unzips from deposit-handle:** Here the bonding between the cargo-strand and the pickup-handle is stronger than the bonding between the cargo-strand and the deposit-handle. The cargo-strand unzips and moves away from the deposit-handle, staying attached and following the pickup-handle; This scenario corresponds to successful pickup. In experiments, this would be the desired outcome.
- **Cargo shears away from pickup-handle:** Here the bonding between the cargo-strand and the pickup-handle is too weak to cause the pickup-handle to shear away from the cargo-strand. This scenario corresponds to unsuccessful pickup and should be avoided in the experiments.
- **Cargo stays attached to both:** If the pickup-handle pulls with too little force, the cargo-strand will neither rupture away from the deposit-handle, nor from the pickup-handle. The pickup-process would be again unsuccessful and should also be avoided in experiments.

Besides the trap-force of the deposit-handle and the string-force for the pickup-handle, all remaining nucleotides could freely move under influence of dynamics/rupture.

When the external pulling force is exerted on the pickup-handle, two independent effects are expected to lead to the delay before full rupture occurs:

- **DNA-stretching:** Before any base-pairs of the cargo-strand rupture under the constant pulling force of the pickup-handle, the helix for the pickup-handle is first stretched [57].
- **Biased random walk delays rupture:** All base-pairs between the cargo-strand and the deposit-handle must break before the cargo-strand is fully ruptured. This does not happen in a consecutive order, but rather as a random walk, similarly to toehold mediated strand displacement [58]. The random walk is biased depending on the force applied to the pickup-handle, since a stronger force implies a higher probability of base-pairs to break, thus implying a shorter delay. The dynamics of a cargo-strand unzipping from the deposit-handle is shown in Fig. 4.2.

4. Simulation of the Pickup-Process

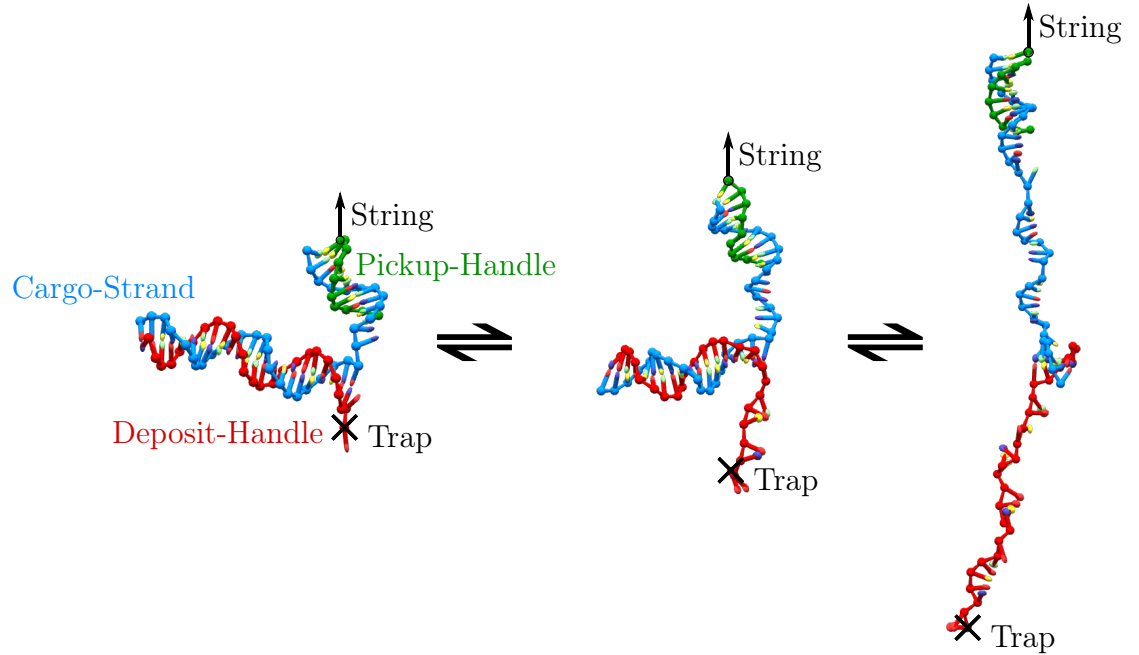


Figure 4.2. | Biased Random Walk. Snapshots taken at different stages of unzipping, visualizing the process of unzipping.

Virtual ceiling

Once rupture has occurred, the string-force applied to the pickup-handle would constantly accelerate the strand, leading the simulation to fail. To solve this issue, a repulsion plane was implemented, acting as an infinite potential barrier, preventing nucleotides to move beyond the limits of simulation space.

Criterion of Rupture

A successful rupture event is detected once the inter-nucleotide distance between the two strands exceeds a certain distance threshold. The distances were measured between the last three nucleotides that were expected to rupture. This method is robust against rehybridization of the two strands after being partially ruptured.

Substructures for Isolated Rupture Comparison

To compare the competing rupture of the cargo-strand with the rates of both shearing and unzipping, isolated rupture-simulations were performed. Here the parent-structure (see Sect. 4) was divided into two substructures

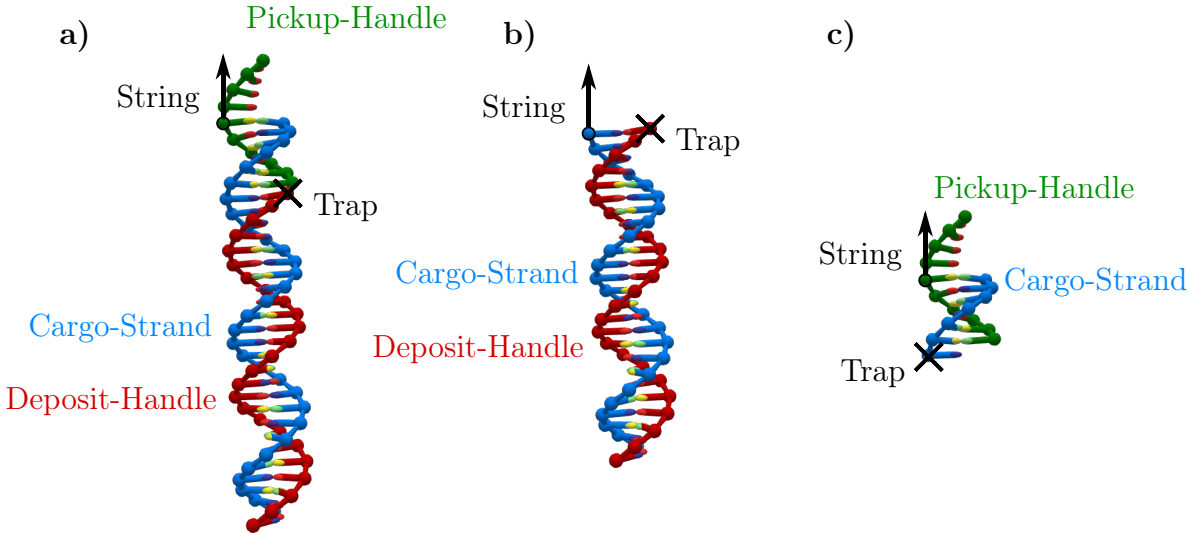


Figure 4.3. | Isolated Rupture Structure. **a**, similar to the parent structure shown in Fig. 4.1. The pickup-handle was extended with 4-polyT bases. **b**, substructure to simulate unzipping-only rupture. For that, a string-force was assigned to the 3'-end of the cargo-strand. **c**, substructure to simulate shearing-only rupture. A trap was assigned to the 5'-end of the cargo-strand. The pickup-handle has 4-polyT bases extended to the 5'-end.

- the **Cargo-Deposit-Substructure** (see Fig. 4.3b)), consisting of the deposit strand bound to the cargo strand. This structure is used for simulating the unzipping process.
- the **Cargo-Pickup-Substructure** (see Fig. 4.3c)), consisting of the pickup strand bound to the cargo strand and is used for simulating shearing. An additional 4-polyT bases were extended from the pickup-strand, adding drag and thus limiting the maximum velocity. This limitation was required, as otherwise the pickup-strand could enter the repulsion plane with a very high velocity, experiencing an unrealistically high resetting force, resulting in the simulation to fail.

For both structures, the length of the cargo-strand was adjusted so no unbound bases would influence the rates.

The isolated rupture was then compared with the competing rupture process of the combined structure shown in Fig. 4.3a).

4.1.2. Parallelization (single/multi class)

Due to the statistical nature of rupture, simulating only one unzipping or shearing event is not enough to study transition rates. Because of that, simulations would need to be repeated many times. However, this would result in much computational overhead and therefore run very slowly.

4. Simulation of the Pickup-Process

The approach in this thesis was to simulate the rupture multiple times simultaneously, in one simulation, running on the CUDA enabled version of oxDNA. This version is optimized for simulating systems with many nucleotides [54].

To implement this, the parent-structure was cloned and placed on a 2-dim grid. All cloned structures were spaced 25.6 nm from each other. The harmonic trap, responsible for fixating the deposit handle of the parent-structure, was moved and redefined for each cloned deposit handle individually. Similarly, the string-force was copied among all pickup-handles.

In single-class parallelization, the string-forces for all pickup-handles were of same magnitude. These simulations were used for high-precision rate analysis at a specific force. However, multi-class parallelized simulations were used for simulating at multiple different forces simultaneously, providing a broader overview of trends at the cost of resolution (see Fig. 4.4).

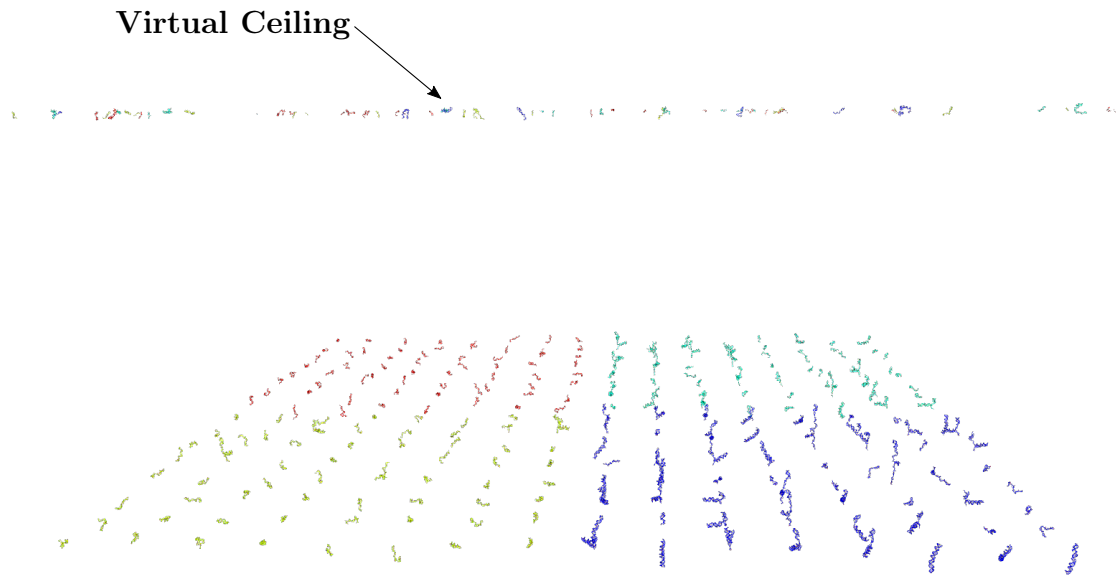


Figure 4.4. | Multi-class parallelization. Snapshot during a simulation based on cloned structures from Fig. 4.1.1. Four different forces were being simulated simultaneously, colored in blue, yellow, red and aqua. Such simulations provided a broader range of force at the cost of fewer datapoints.

4.2. Results

4.2.1. Dynamics of single structure rupture

The dynamics of the unzipping process during pickup of cargo-strands was analyzed in Fig. 4.5. Thereby, the repetitive bond-breaking and rehybridization of a base-pair seven

bases prior the 5'-end of the deposit-handle was examined. The plot shown in Fig. 4.5 suggests the presence of random-walk-like unzipping rupture.

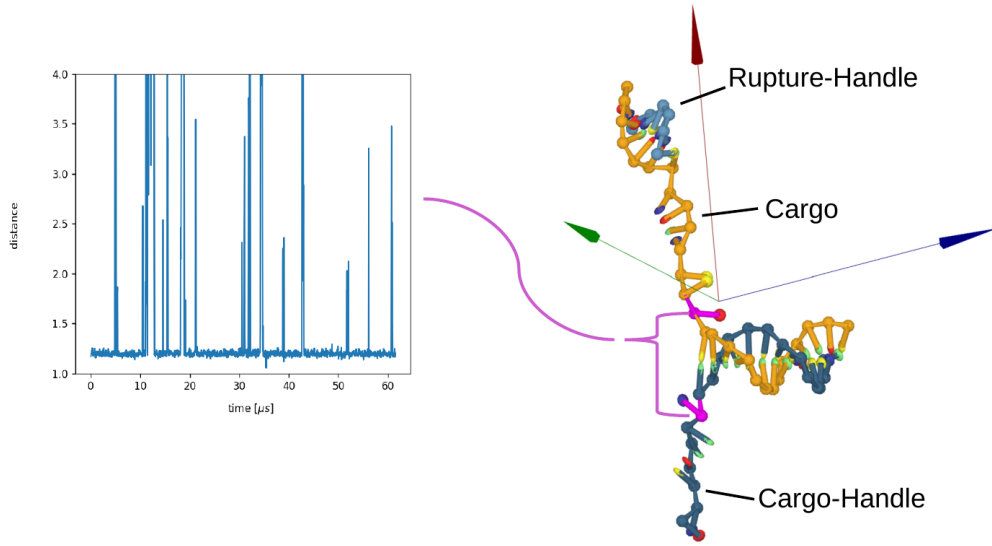


Figure 4.5. | Dynamic inter-nucleotide distances during rupture. Distances plotted between two opposite nucleotides, emphasizing the random-walk behavior of unzipping rupture between the cargo-strand and the cargo-handle.

4.2.2. Force screening

To infer the force dependency on the unzipping rates, up to 256 unzipping rupture events were simulated for forces ranging from 16.5 pN – 20 pN. In these simulations the combined structure including the pickup-handle was used. However, the bonding between the pickup-handle (10 bp, GC-content: 70 %) and the cargo-strand was strong enough so that no unsuccessful rupture occurred in the simulations. The deposit-handle had a sequence length of 25 bases with 36 % GC-content. The fraction $P_{\text{unzip}}(t)$ denotes the relative amount of unzipping events between the cargo-strand and the deposit-handle (defined in Sect. 4.1.1), and can be seen in Fig. 4.6a).

At the start of the simulation, all cargo-strands are bound to the deposit-handle, so that $P_{\text{unzip}}(t = 0) = 0$. Thereafter, $P_{\text{unzip}}(t > 0)$ follows a saturation curve, with maximum value of 1, which happens when all cargo-strands are completely unzipped from the deposit handle. During the simulations, forces at 19 pN, 19.5 pN and 20 pN led to successful unzipping of all cargo-strands from the deposit-handle. Weaker forces showed a similar trend of the unzipping fraction, however, the fraction did not converge to 1 during the simulations.

4. Simulation of the Pickup-Process

The rupture rates from the simulations were fitted with a shifted cumulative exponential distribution, motivated by boltzmann energy distribution [59]

$$P^*(t) = \begin{cases} 1 - \exp\left(-\frac{t-t_{\text{offset}}}{\tau}\right) & t \geq t_{\text{offset}} \\ 0 & t < t_{\text{offset}} \end{cases} \quad (4.1)$$

with $\tau \in \mathbb{R}$ and $t_{\text{offset}} \in \mathbb{R}^+$. This also resembles the case of eq. 2.6 with $k_1 = 0$ and $k_2 = k$. All fits shown in this thesis were fitted with this function.

The force dependency of τ and t_{offset} is shown in Fig. 4.6b-c). From Fig. 4.6b) it follows, that $\tau(f)$ exponentially decreases from $248 \mu\text{s} - 1.6 \mu\text{s}$ with increasing force f from $17.5 \text{ pN} - 20 \text{ pN}$ However, for high forces starting from 19.5 pN , this trend is flattened.

A consistent trend for the offset t_{offset} with respect to the force f cannot be seen. With exception for the weakest force at $f = 17.5 \text{ pN}$ are all $t_{\text{offset}}(f)$ constant at $\approx 1.6 \mu\text{s}$.

4.2.3. Length Dependence

The length dependency of the competing rupture simulation, specifically unzipping of the cargo-strand from the deposit-handle, was investigated for two different cargo-strands:

- 27bp Cargo: Deposit Handle 20 bases with 35 % GC, Pickup Handle 7 bases with 71 % GC
- 35bp Cargo: Deposit Handle 25 bases with 36 % GC, Pickup Handle 10 bases with 70 % GC

The fraction of unzipped and sheared cargo-strands can be seen in Fig. 4.7a-b).

As unzipping of the pickup-handle also occurred for the 27bp cargo-strand, the data-points were fitted separately for both cases, either shearing and unzipping:

$$P_{\text{unzipping}}^*(t) = C_{\text{unzipping}} \cdot P^*(t) \quad (4.2a)$$

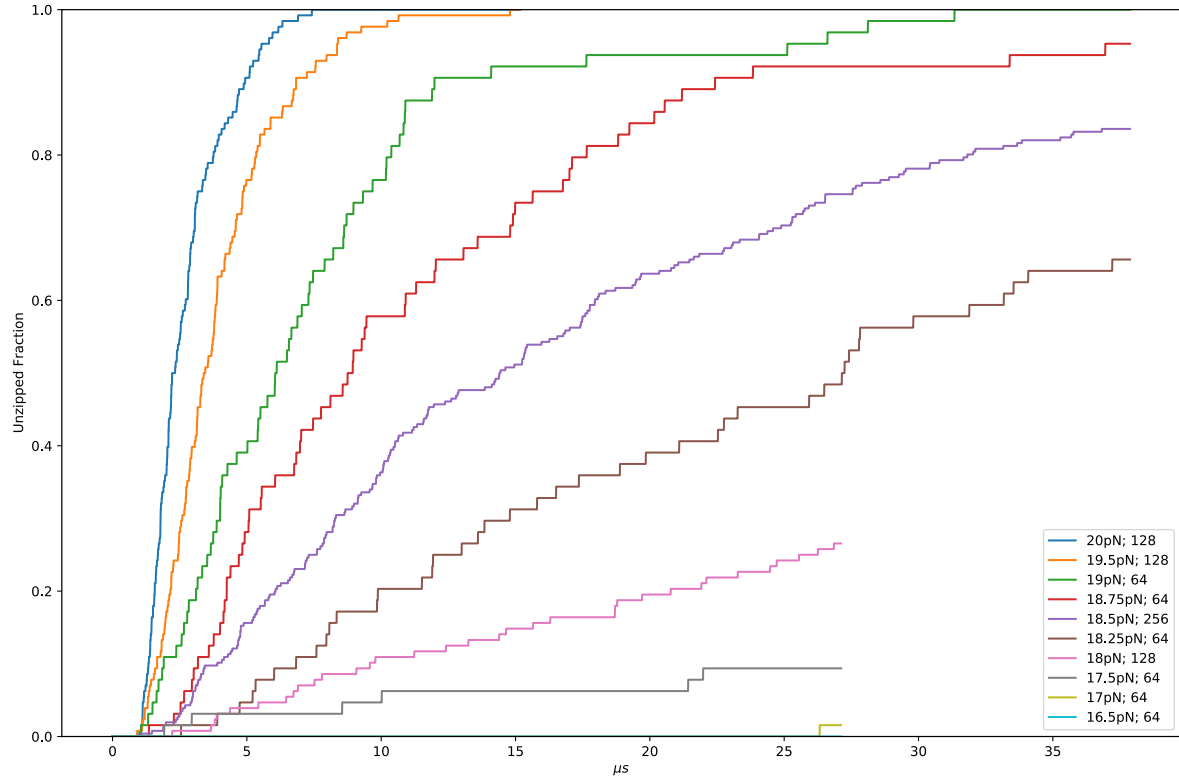
$$P_{\text{shearing}}^*(t) = C_{\text{shearing}} \cdot P^*(t) \quad (4.2b)$$

with $C_{\text{unzipping}} \in [0, 1]$ and $C_{\text{shearing}} \in [0, 1]$ being constant scaling factors, so that $C_{\text{unzipping}} + C_{\text{shearing}} = 1$. The ratio $F = \frac{C_{\text{shearing}}}{C_{\text{shearing}} + C_{\text{unzipping}}}$ indicates the relative frequency of shearing events if any rupture occurred.

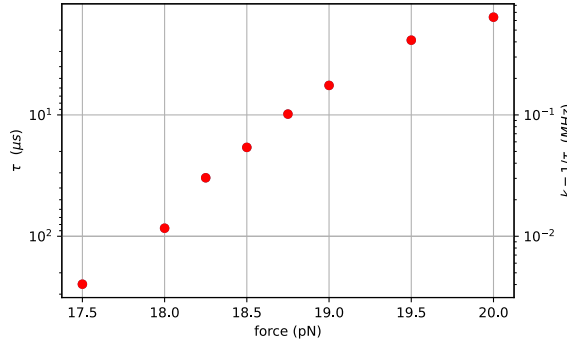
The fit for unzipping events of the 27bp cargo-strand starts inclining at $t_{\text{offset}}^{27} = 1.0 \mu\text{s}$, whereas the 35bp cargo-strand inclines at $t_{\text{offset}}^{35} = 1.8 \mu\text{s}$. Furthermore, the saturation curve for the 27bp cargo-strand is steeper with $\tau^{27} = 18.5 \mu\text{s}$ compared with the 35bp cargo-strand with $\tau^{35} = 10.9 \mu\text{s}$.

Fig. 4.7b) shows the unsuccessful rupture of the cargo-strand shearing away from the pickup-handle, which only happened for the 27bp cargo-strand with a frequency of

a)



b)



c)

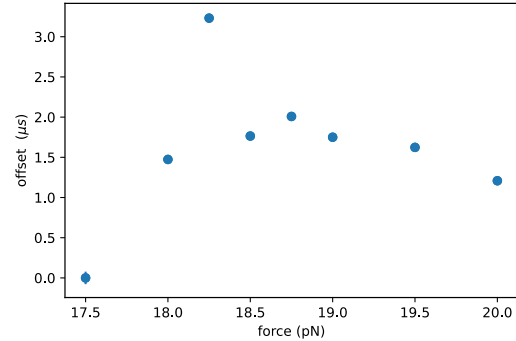


Figure 4.6. | Fit Force Screening. **a**, fraction of successfully picked-up cargo-strands for forces screened between 16.5 pN and 20 pN. The simulations were performed for various number of clones (between 64 and 256), that are specified in the legend. **b**, fitting parameter τ plotted with respect to the corresponding force f . The fitting parameter was evaluated from the fitting-function Eq. 4.1, optimized for all fractions from **a**. The y-scale is given for the mean unzipping time τ and the rate k . **c**, fitting parameter t_{offset} plotted with respect to the corresponding force. The fitting parameters in **b** and **c** are not shown for simulated forces at 17 pN and 16.5 pN, because not enough unzipping events were detected for a meaningful fit.

4. Simulation of the Pickup-Process

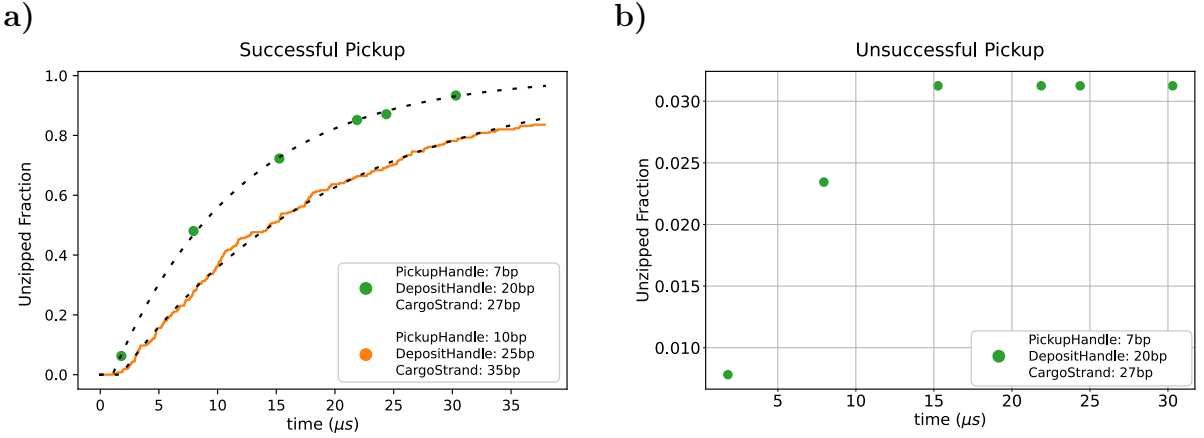


Figure 4.7. | Length Dependence. **a**, unzipping of cargo-strand from deposit-handle. The simulations were performed on two different structures. The dashed lines correspond to fitted functions, according to Eq. 4.1. **b**, shearing of cargo-strand away from pickup-handle. This case only happened for the 7bp-long pickup-handle and is therefore not shown for the structure with the 10bp-long pickup-handle.

$F^{27} \approx 0.03$. As no shearing occurred for the 35bp cargo-strand, the frequency of shearing is thus given by $F^{35} = 0$.

4.2.4. Isolated versus competing rupture comparison

This section presents the difference of competing rupture rates versus the isolated rates obtained for shearing-only and unzipping-only rupture, which were simulated with the Cargo-Pickup-Substructure and the Cargo-Deposit-Substructure respectively. The competing rupture was simulated with the original parent-structure.

For the parent-structure and the substructures, the handles used were

- Cargo-Deposit-Handle: 25bp, 0.36 % GC. Here the string-force was assigned to the cargo-strand.
- Cargo-Pickup-Handle: 6bp + 4-polyT extension, 67 % GC. Here the cargo-strand was fixated using a trap.

The length of the cargo-strand was adjusted for the parent-structure (31bp), the structure for unzipping-only (25bp) and for the structure for shearing-only (6bp).

The rupture rates are compared in Fig. 4.8 and were fitted again with the separated $P^*(t)$ from Eq. 4.1. The unzipping-only and shearing-only rupture of the combined rupture was fitted with the updated fitting functions for $P_{\text{unzipping}}^*(t)$ and $P_{\text{shearing}}^*(t)$ from eq.4.2.

The shortest offset t_{offset} could be seen for isolated shearing at 0.0 μ s, followed the combined rupture at 1.0 μ s. The isolated unzipping was delayed most at 2.4 μ s.

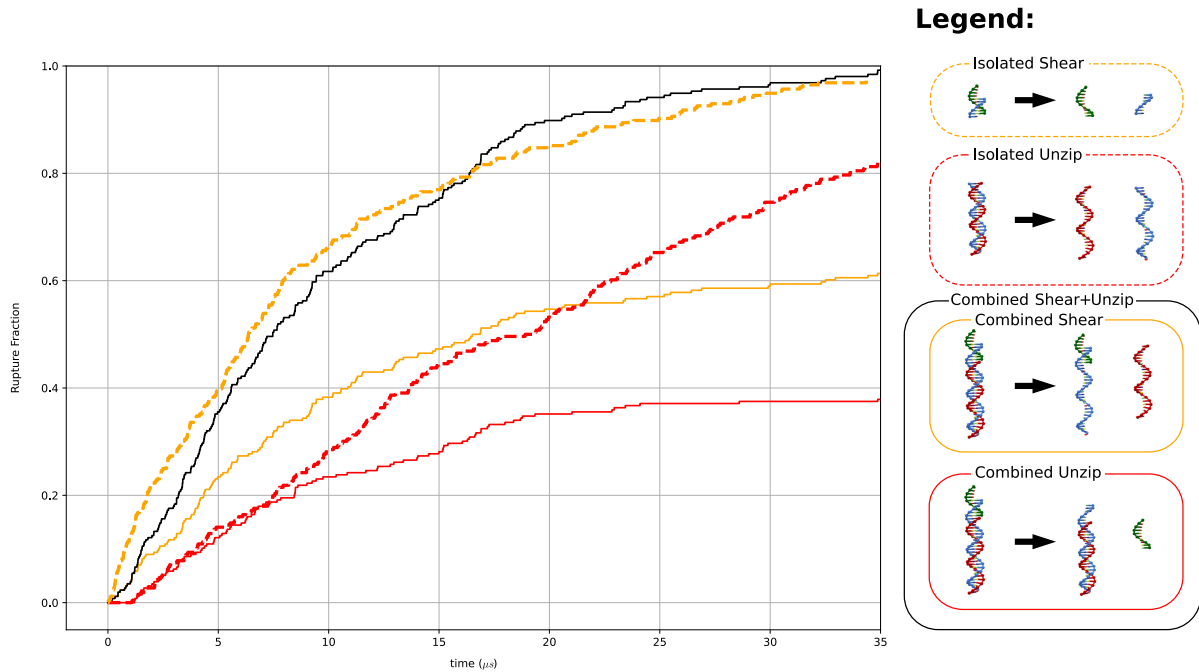


Figure 4.8. | Isolated vs Competing Rupture. Based on parallelized rupture simulations with the parent structure defined as in Fig. 4.3. Rupture fraction of 3 simulations shown: first, the successful and unsuccessful pickup of cargo-strands of the combined structure (solid line), second, the unzipping-only rupture of a substructure (dashed red), and third, the shearing-only rupture of a substructure (dashed orange). Colored in black is the fraction of any rupture event, either shearing or unzipping, of the combined structure.

Isolated unzipping happened with a rupture time of $\tau_{\text{isolated}}^{\text{shear}} = 21 \mu\text{s}$. The shearing in the combined structure happened twice as fast with $\tau_{\text{combined}}^{\text{shear}} = 10.25 \mu\text{s}$.

For the combined rupture, the fraction of isolated unzipped cargo-strands converges to 63 % while on contrary isolated sheared cargo-strands converged to 40 %. This yields a relative shearing frequency of $F = 0.39$.

4.3. Discussion

The simulations show, that oxDNA can be used to investigate competing rupture rates of unzipping and shearing for given sequences. Furthermore, oxDNA proves to be a useful tool for tuning the cargo-strand sequences and thereby optimize the ratio between unzipping and shearing with regard to the deposit- and pickup-handle.

Most importantly, the simulations show that the cargo-strand can successfully be picked up by pulling at the pickup-handle with a force in the order of pico-newton. Successful pickup was seen throughout almost every simulation, despite that the cargo-strand had much less H-bonds with the pickup-handle than with the deposit-handle. This result is not only in full agreement with the theory explaining the difference of shearing versus unzipping (see sect. 2.2), but also shows that very little forces are required when choosing an appropriate sequence. Thus, the pickup-process does not require external instruments like an AFM [28] and can be implemented for applications directly on nanostructures like the roboarm used in this thesis.

4.3.1. Delayed Rupture

The delayed rupture can be seen for all unzipping simulations. The trend of decreasing t_{offset} when pulling with stronger force cannot be clearly seen in the fits for fig. 4.6c). This suggests DNA-stretching contributes more to t_{offset} . However, from fig. 4.5 follows, that the biased random walk plays a significant role during rupture, as base-pairs in the middle of the strand break and rebind throughout the simulation, implying constantly reforming of the duplex.

From the difference in time offset that can be seen for the two different structures in Fig. 4.7, one cannot conclude about which of the two effects contributes more to the delay. The 3bp longer pickup-handle would lead to more stretching, however, the 10bp longer deposit-handle results in more random walk before full rupture.

4.3.2. Rupture Rates

As expected, a higher force applied to the pickup-handle leads to faster rupture (fig. 4.6). Furthermore, an exponential increase of the rupture rate k with respect to the force of the pickup-handle becomes apparent. This trend flattens for high forces. This motivates a regime of forces proven to be practical for simulating the competing rupture of multi-strand systems on microsecond timescale using oxDNA. The regime can be used for a starting point for new simulations used to optimize sequence dependent rupture.

However, the simulations also show, that the pickup-handle requires a certain minimum length to ensure that the pickup-process is successful. This becomes apparent when

looking at the frequency of shearing events F for the 27bp-cargo-strand and the 35bp-cargo-strand. F can be interpreted as the probability of shearing, once the simulation has terminated and many rupture events have been detected. A too short pickup-handle results in the shearing-induced rupture from the cargo-strand, which is primarily caused by thermodynamic instability.

The difference of rupture rates regarding isolated substructures compared with the original parentstructure (fig. 4.8) indicates, that the dynamics of the pickup-handle do influence the unzipping of the deposit-handle. Thus, it is not possible to conclude from other experiments, simulations or theories that investigate shearing- or unzipping-only rupture, to the rate of successful pickup of the cargo-strand.

It should be noted that the additional 4-polyT bases that extend from the pickup-handle to limit the maximum velocity by introducing drag, may contribute to destabilization of the pickup-handle [60] and thus potentially increase the shearing rate. Therefore, it is not possible to directly compare the shearing rates and the probability of unzipping with the previous simulations, which did not have the 4-polyT extension.

4.4. Conclusion

In this chapter, we showed how to perform MD-simulations of dynamic mechanisms in a massively parallelized manner using oxDNA. We used this method to understand how sequence dependency and applied forces to the pickup-handle influence the successful pickup-process of a cargo-strand. Thereby we found, that a longer pickup-handle results in a higher fraction of successfully picked-up cargo-strands, and that a longer deposit-handle results in a slower unzipping rate. Overall the rupture process agrees well with the theoretical proposed rupture rates from eq. 2.6. We found that the MD-simulations resemble the random-walk-like dynamics of rupture, especially for unzipping. This behavior significantly slows down rupture events. Thus, we defined ranges, in which rupture events can be simulated using oxDNA within reasonable simulation times (≈ 7 d for simulating 256 cloned structures for ≈ 35 μ s) with current computing power. Finally, we investigated how the dynamics of competing unzipping- versus shearing-rupture differs from isolated unzipping-only and shearing-only rupture. Thereby we concluded that MD-simulations of the whole three-strand-system are required to infer about rupture rates of sub-systems.

5. Experimental Part

This chapter presents the experimental progress towards the realization of molecular cargo transport using the roboarm that was introduced in Sect. 2.5. The transportation mechanism is based on the difference in force required for unzipping and shearing in order to separate a DNA duplex. The foundation of the mechanics was described in Sect. 2.3 and was simulated in-depth in Sect. 4.

This chapter addresses challenges faced in experiments:

- only loading specific handles with cargo-strands while preserving others
- Visualization of cargo-strands and orientation of the roboarms using high-resolution microscopy during different time points over the course of the experiment.
- Increasing exerted torque on the pointer while preventing overheating by the applied electric field. High temperatures can lead to unsuccessful pickup of cargo or can even result in the melting of the DNA nanostructures.

5.1. Experimental methods

5.1.1. DNA Origami Fabrication

Folding Process

The folding (see Sect. 2.4.2) of the baseplate and the pointer, is performed with an excess of 3 times as many oligonucleotides as there are scaffold-strands they could bind to. This ensures that most structures do not miss any staples.

The folding itself is performed using a thermocycler with a protocol that depends on the structure to be folded:

- **Baseplate and Pointer (separately):** Temperature ramp from 70 °C down to 20 °C with 0.1 °C steps and holding temperature for 2 min in each step. The temperature ramp ensures that the structure-specific cooperative folding temperature will be reached. At this point, the baseplates and the pointers are folded separately, since a similar sequence is being used for both structures. Trying to fold the whole roboarm at once would result in staples designed for the pointer to bind to the scaffold of the baseplate and vice versa.

5. Experimental Part

- **Attaching the pointer to the arm of baseplate:** Since here both the pointer and the baseplate with the arm are already folded, the attachment of both happens in only 30 min at 37 °C.

PEG Purification

Polyethylenglykol (PEG-purification) is an easy and efficient way to remove the excess of staples that did not bind to the scaffold [61]. This method can also be used to change the solvent or increase the concentration of the structure.

PEG is a polymer with chemical formula $\text{HO}(\text{CH}_2\text{CH}_2\text{O})_n\text{H}$ where n specifies the number of repeating units. It is highly soluble in water [62] and forms surfactants [63].

When mixing the precipitation buffer containing PEG with the unpurified sample, the H_2O molecules will associate to the -OH of the PEG molecules, leading to precipitation of the larger folded origami structures. Oligonucleotides are more mobile due to their much smaller size, thus less likely to aggregate and therefore still dissolved in solution.

After centrifugation, the precipitated structures form a pellet. The supernatant containing the unbound staples and the precipitation buffer can now be removed, leaving ideally only the folded origami-structures behind. Finally, the pellet is dissolved in the target buffer. Vortexing the sample ensures that the pellet is again fully dissolved.

Gel-Electrophoresis Purification

Gel-electrophoresis purification is a method to separate different types of DNA-origami or DNA multimeres solved in the same dissolved from each other. Thus, unlike PEG-purification, it can also be used to separate misfolded DNA-origami structures from correctly folded ones. However, downsides of Gel-electrophoresis lie in a lower yield of the target structures and a more time-consuming process compared to PEG-purification. Detailed example protocols of how gel electrophoresis is performed and how this method is employed to purify origami constructs can be found in [64].

Fundamentally, gel-electrophoresis is based on the negative charge of the backbone of DNA. With an externally applied electric field, DNA strands experience a force and thus accelerate towards the anode. When placed in a gel matrix, smaller macromolecules migrate faster through the pores of the gel matrix than larger macromolecules.

In this thesis, a solidified agarose gel matrix was used and was placed in a gel chamber. Unpurified samples were loaded into wells in the gel matrix. The wells were formed using a comb and were placed on a line orthogonal to the electric field. An electric field is generated by applying a voltage (in this thesis: 9 V cm^{-1}) between two electrodes that contact the buffer at opposite sides of the gel-chamber. Higher voltages result in faster migration, thus speeding up the purification process. However, this comes at the cost

of resolution, as higher voltages lead to higher temperatures which can cause the gel to melt.

After applying the voltage for a defined duration (in this thesis: 1 h), equally-sized structures cluster and form distinct bands at size-dependent migration distances in the gel-matrix. To visualize the bands containing the desired structure, a fluorophore labeled staple oligonucleotide was inserted into the structure during the folding process. Finally, the bands are cut out from the gel, squeezed to eliminate the agarose and diluted in the target buffer. Misfolded structures and unbound staples remain in the gel.

5.1.2. Monitoring of molecular transport experiments with single molecular TIRF microscopy

The experimental readout had three main requirements:

- Readout of the current orientation of the roboarm/pointer
- Verify if cargo- or auxiliary-strands are attached to the baseplate.
- Readout should take place in real-time and should only include structures in immediate proximity of the surface of the glassslide.

For that purpose, a total internal reflection fluorescence microscope (TIRFM) was used, which detects the excited fluorophore of the pointer, cargo- and auxiliary-strands.

TIRF-Microscopy

Single molecule interactions that are of interest for this thesis occur near the surface of the glassslide. Fluorescent molecules in bulk contribute to background noise, leading to a lower signal-to-noise ratio. To improve the signal-to-noise ratio, the effect of total internal reflection is used: at a criticle angle, the excitation light does not propagate through the glassslide into the sample, but gets reflected, generating an evanescent wave that has exponentially decreasing intensity with regard to the distance of the surface. Thus, only fluorescent molecules near the surface of the glassslide get excited, resulting in a high signal-to-noise ratio.

A schematic of a TIRF-microscope is shown in Fig. 5.1. A laserbeam is directed parallelly to the optical axis of the camera through the objective towards the glassslide that holds the fluorescent sample. The beam enters the objective off-center of the optical axis, so that it defletcs in the lens and hits the glassslide at a large angle. When the incident angle is equal or above a critical angle, then total internal reflection occurs at the interface between the glassslide and the buffer of the sample, because the glassslide has higher refractive index than the buffer. Thus, the beam does not exit the glassslide into the sample, but rather reflects back into the oil drop. Thereby it generates an evanescent wave at the interface. The amplitude of the evanescent wave drops exponentially with

5. Experimental Part

distance away from the surface, therefore only fluorophore near the surface are excited and emit photons. These photons emitted by the fluorescent dyes are then detected by a camera.

The signal-to-noise ratio decreases when the incident angle is below the critical angle, as fluorophore that are further away also become excited. However, an incident angle well above the critical angle reduces the intensity of the signal, again decreasing the signal-to-noise ratio [65].

The evanescent wave can propagate up to ≈ 100 nm into the sample, depending on the incident angle, the refraction index and the thickness of the glassslide [65, 66]. Furthermore, one can use multiple wavelengths to select only specific type of fluorophore. In this thesis, lasers with wavelength of 480 nm and 532 nm were used.

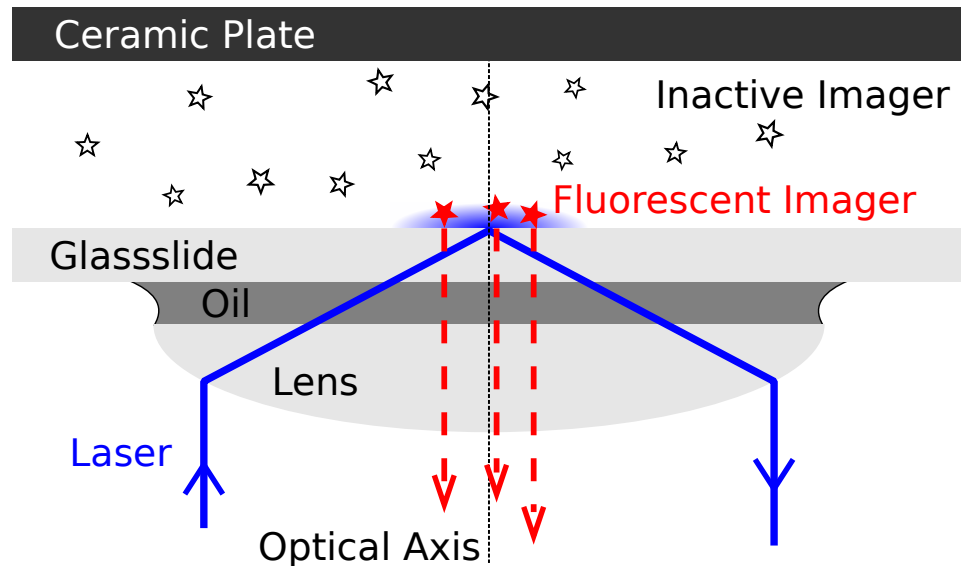


Figure 5.1. | TIRFM. Schematics of TIRFM-setup, shown with fluorescent imager, that only emit photons when excited by the evanescent wave (blue).

Superresolution imaging with DNA-PAINT

Direct labeling of DNA nanostructures with fluorescent dyes, as performed for tracing the tip of the DNA pointers, comes with several drawbacks:

- Long measurements or powerful laserbeams can result in bleaching of the dye, which decreases the signal and consequently increases the signal-to-noise ratio.
- The resolution between two nearby fluorophores is limited by the Abbe diffraction limit [67]. The distribution of detected photons for a single fluorophore is described by a point-spread-function (PSF), with the centroid of the distribution being the position of the fluorophore. When two nearby fluorophores simultaneously emit

5.1. Experimental methods

photons, the two PSFs overlap, resulting in combined distribution that approximates a single PSF. This is demonstrated for the case of gaussian beams in see Fig. 5.2. Both fluorophores can only be distinguished with elaborate measurement techniques whereby one of the two dyes can be deactivated temporarily (STORM, STED [68, 69]).

- Multiplexing can only be achieved by using various types of fluorophores that have different excitation wavelengths. Every type of fluorophore would require its own laser leading to an expensive and more complex optical setup. Furthermore, fluorophores can even get excited with photons of lower wavelength than intended, thus the channels can mix up.

DNA-PAINT (Points Accumulation for Imaging in Nanoscale Topography) is a promising alternative that solves these problems [70, 71]. This imaging method builds upon prior methods of PAINT [72]. In DNA-PAINT, fluorophores are not attached to the structures directly. Instead, the structures have oligonucleotide extensions, the docking-handle, to which the imager can transiently bind to. Imager strands are dye modified oligonucleotides with complementary sequences to the docking-handle, which temporarily bind to these handles. The stability of the bond can be varied by the sequence used for the imager and the docking-handle. The on-time t_{bright} , which is the average time an imager is bond to the docking-handle, is then given by the dissociation rate k_{off} of the imager, by the relation

$$t_{\text{bright}} = \frac{1}{k_{\text{off}}}. \quad (5.1)$$

The off-time t_{dark} , depends on the salt concentration, the concentration of the imager c and the association rate k_{on} , by the relation

$$t_{\text{dark}} = \frac{1}{c \cdot k_{\text{on}}}. \quad (5.2)$$

With appropriate parameter choice, the imager will constantly bind to and dissociate from the docking-handles, which will be perceived as blinking. The concentration of the imager should be chosen low enough, so that two simultaneous blinking events of neighboring docking-handles at the same time are highly improbable. However, a high concentration of imager strands reduces recording time due to more frequent binding events. A 2D-PSF is fitted to each blink-event. Afterwards, the centroids of all 2D-PSF localizations are visualized in a 2D-histogram. With this method, a much higher resolution (sub 5 nm spatial resolution [71]) compared to direct labeling of DNA nanostructures can be achieved, as the PSF-distributions of the docking-handles do not interfere with each other.

Furthermore, bleaching is no longer problematic, as the imager near the surface that become excited by the evanescent wave are constantly being replaced by diffusive imager in the buffer.

5. Experimental Part

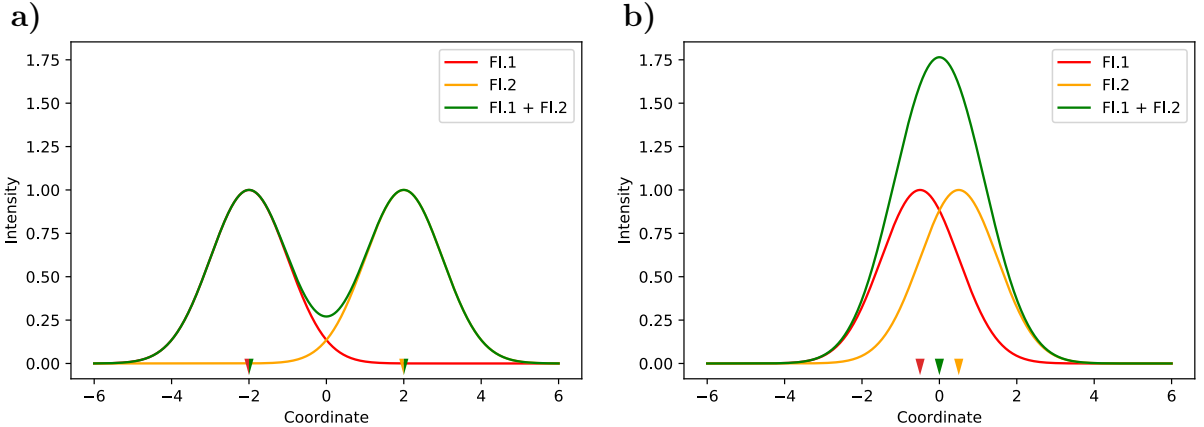


Figure 5.2. | Paint Distribution Comparison. Shows PSF of two fluorescent sites, fluorophore_1 (Fl.1) and fluorophore_2 (Fl.2). The combined PSF Fl.1+Fl.2 provides the intensity distribution for direct labeling. In **a**, both fluorescent sites are far apart from another, so that the maxima are found at the same positions for direct labeling or PAINT-measurements. In **b**, the fluorescent sites are close together, so that only one maximum can be seen for the combined channel Fl.1+Fl.2 and thus both sites cannot be distinguished from another. PAINT-techniques are required.

Exchange-PAINT

Exchange-PAINT is used for multiplexing and is based on DNA-PAINT [71]. Here, various types of docking-handles with orthogonal DNA sequences are used. The imager only bind to their corresponding docking-handle. For each type of docking-handle, a separate buffer is used that contains the corresponding imager. All buffers are then exchanged and measured separately. When exchanging the imager-buffer, the sample is washed thoroughly with a clean buffer, to ensure that no imager of the previous buffer is left, before adding the new imager-buffer. Finally, all localizations are visualized in a 2D-histogram, color-coded with the type of imager-buffer they were measured with.

In conclusion, Exchange-PAINT provides the benefits of DNA-PAINT, plus the flexibility that comes with multiplexing while using only one fluorescence channel.

Speed-PAINT

Speed-optimized DNA-PAINT (Speed-Paint) is based on the principles of DNA-PAINT, but is optimized for shorter recording times. Shorter imaging is useful to reduce drifting-related artifacts.

Using multiple docking-handles increases the on-rate k_{on} , which speeds up the measurement. These docking-handles can be combined to one single strand, that consists of several repetitions of the original docking sequence. However, both methods lower the spatial resolution of the localizations.

Speed-PAINT also uses a single docking-handle with multiple repetitions, however, here the repetitions overlap with each other. With this approach, the docking-handle can be

shorter, which generally implies a higher spatial resolution, while still having the same number of repetitions [73].

The on-rate k_{on} scales linearly with the number of repeats of the docking-handle up to 5x repeats, independently of the chosen sequence for imager and docking-handle. Using more repeats, can lead to a decreased accessibility so that k_{on} stagnates [73].

Naming convention

The naming-convention for the buffers used in this thesis is analog to [71, 73]. Conventional PAINT-imager are denoted as P1, P2, ..., P6 and SpeedPAINT-imager are denoted with R1, R2, ..., R6. The sequences for all imager are orthogonal to each other, enabling the ability of multiplexing.

The sequences for docking-sites for SpeedPAINT begin with the number of repetitions. For example the docking-site with sequence 5xR2 corresponds to the R2-imager with 5 repetitions implemented.

PAINT-Buffer

For all SpeedPAINT-measurements, the BufferC from [73] was used, which is defined in the Appendix A.3. In addition to the BufferC, TWEEN in was used to obtain a more reproducible bright time.

5.1.3. PAINT image processing routine

The microscopy videos obtained from PAINT, SpeedPAINT or by single particle tracking fluorescence microscopy measurements using TIRFM are processed, analyzed and visualized with the software package `picasso` [71]. First the blink events are localized, using `picasso: localize`. One can adjust the sensitivity and specificity with parameters like *Box side length* or *Min. net gradient* in `picasso: localize`. The program then proceeds in two steps:

- **Identify:** Here `picasso: localize` searches for any blinking event with a spot-size smaller than provided *Box side length* in each frame of the movie. A positive blink-event is identified when the contrast-gradient exceeds a certain threshold.
- **Fit:** For the fit, every identified blink-event is fitted with a 2D multivariate Gaussian distribution [74].

5. Experimental Part

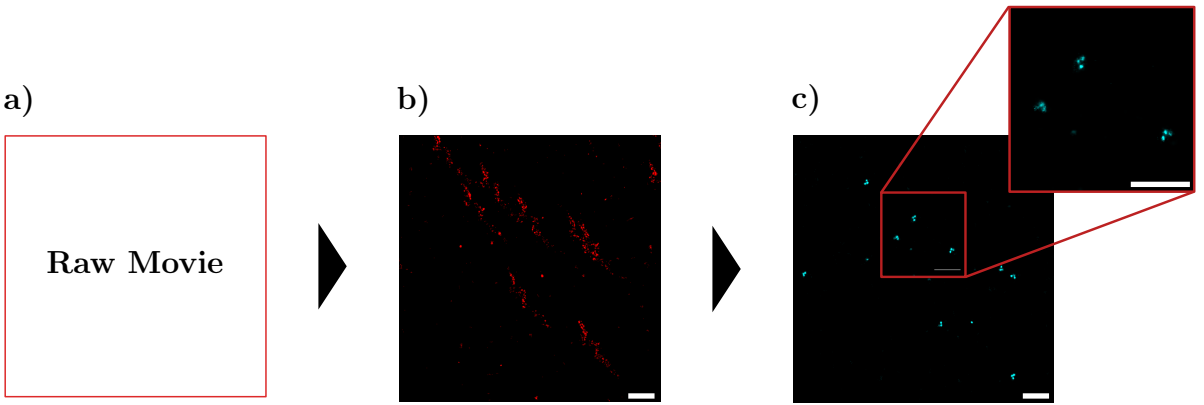


Figure 5.3. | Workflow DNA-PAINT analysis. **a**, raw movie recorded using an TIRFM. **b**, histogram of all blink-event-localizations from **a**, using `picasso: localize`. **c**, post-process of localizations using `picasso: render`. Three corners of the baseplate become clearly visible. Scalebar: 500 nm

When using Exchange-PAINT, this localization step must be repeated for each measurement separately.

The fitted blink-events can then be visualized using `picasso: render`. Besides providing various representations for the fits, `picasso: render` also allows post-processing, for example to correct for the drift. Furthermore, localizations of multiple separate measurements can be combined, aligned and color-coded. This is especially useful when multiplexing with multiple different imagers.

The typical workflow used in this thesis is summarized in Fig. 5.3 on the basis of a baseplate with 3 corners containing 3 adjoined 5xR1 docking-handles.

5.2. Structural Design of the Cargo Transport System

All structures used in this thesis were based on the CQO baseplate introduced in Sect. 2.5. These baseplates were further equipped with functional staple extensions, for example handles to position and store the molecular cargo. This section also describes changes performed on the pointer, so that the pickup of cargo-strands could be realized.

5.2.1. Deposit- and Target-Handles

The deposit-handle and the target-handle are staple extensions on the baseplate, to which cargo-strands can bind to. The goal of the cargo loading procedure is to generate a starting configuration in which all deposit-handles have a cargo-strand hybridized to while simultaneously preserving the target-handles.

5.2. Structural Design of the Cargo Transport System

Multiple variations of deposit-handle and target-handle were designed and tested. All variations had in common, that all deposit-handles and target-handles were bundled on one side respectively. This maximized the distance between deposit-handle and target-handle, simplifying PAINT-imaging. In the variations, the number of deposit-handles and target-handles varied from 1 to 3, increasing the density of cargo-strands to be loaded and transported.

In the cargo loading process, only the deposit-handles should be loaded with cargo-strands. Methods to minimize the fraction of target handles with cargo oligonucleotides falsely attached are described in Sect. 5.3.

The two most promising design-approaches are:

- **Triple-cargo-site:**

Here, three deposit-handles and target-handles are placed with radius of ≈ 22 nm from the joint and ≈ 9.5 nm apart from each other. This equals an average angular difference of $\approx 26.0^\circ$ between neighboring deposit- and target-handles. This approach is shown schematically in Fig. 5.4a). Implementing three deposit- and target-handles provides redundancy for cargo-loading.

- **Single-cargo-site:**

Here only one deposit-handle and one target-handle is implemented at opposite sides of the baseplates, both ≈ 22 nm distant from the joint. This approach is shown in Fig. 5.4b).

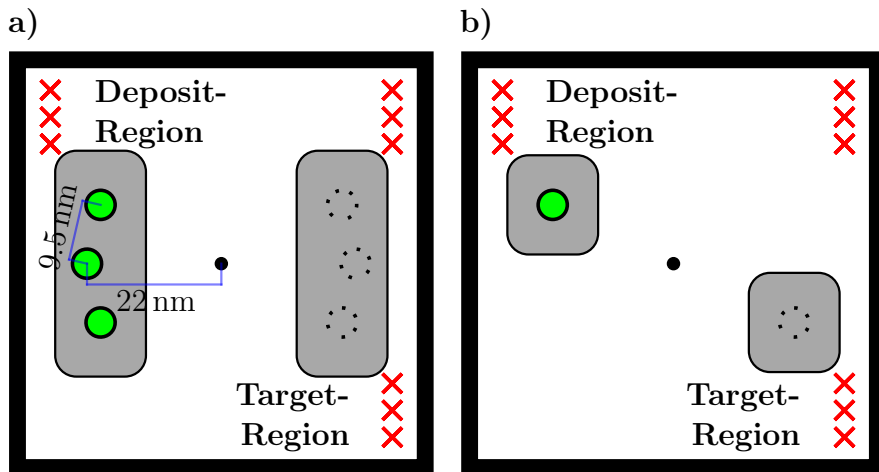


Figure 5.4. | Deposit- and Target-Handle. Overview of the baseplate on which cargo-strands were stored. The pointer is not drawn. The cargo-strands were initially placed at the deposit-region and should be transported to the target-region. The corners labeled via PAINT-handles are shown by red "X". The cargo-strands are shown in green. Here, all deposit-sites were loaded with cargo-strands, while all target-sites had no cargo-strands attached to. Solid-line circles represent deposit-handle, dotted-line circles represent target-handle. **a** shows the triple-cargo-site design. **b** shows the single-cargo-site design.

5. Experimental Part

5.2.2. Pickup-Handle

A staple extension on the nanorobotic arm acts as a pickup-handle to transport the cargo-strand. When no cargo-strands are present, the arm with the pickup-handle can freely rotate. Applying an electric field can manipulate the pointer and therefore also apply forces to the pickup-handle.

For the experiments, the pickup-handle was tested on two pointer constructs: The longer High-Aspect-Ratio-Pointer and the shorter, cone-like shaped Tapered-Pointer, who was also thicker and thus stiffer near the pivot (see Fig. 2.10). Which pointer exerts more torque under given electric field is still subject of current research.

When the deposit-handles are loaded and the pickup-handle reaches the a cargo-strand, either via diffusion or by electroactuation, the pickup-handle hybridizes with the cargo-strand. Once hybridization has taken place, the arm is connected to the baseplate via pickup-handle \leftrightarrow cargo-strand \leftrightarrow deposit-handle and thus cannot freely rotate anymore. The diffusive motion of the pointer is therefore a good indicator of whether the pickup-strand is bond to a loaded cargo-strand.

To pick up the cargo-strand, an electric field must be applied at an angle, inducing a pulling-force on the pickup-handle via the arm. When rupture occurs, the pointer immediately tries to align to the electric field.

At this point, it is not clear whether the cargo-strand unzipped from the deposit-handle, or the pickup-handle sheared away from the cargo-strand. The latter case is indicated when the pointer snaps back to the deposit-position after eliminating the electric field. However, if the pointer remains aligned pointing towards the target-handles, a successful transport is not guaranteed. This could for example be the case when the pickup-handle shears away from the cargo-strand at the deposit-handle and hybridizes with a falsely occupied target-handle. Thus the cargo-strands was visualized independently, using Speed-PAINT.

The process of pickup and transportation with all possible cases is depicted in Fig. 5.5.

5.2.3. Marker

Marker-structures (MCQO) were used to improve drift-correction and the alignment of the different Exchange-PAINT channels, as thees markers are visible in both Exchange-PAINT channels and for single molecule pointer tracking. To construct marker-structures, two approaches were tested.

The first approach used the already existing PAINT-corners of the roboarm (see Fig. 5.6a)). PAINT handles in the three corners create a distinguishable pattern for drift-correction and alignment. This marker did not include the pointer and arm, and therefore required PAINT-imager to be visible. The docking-handle at the corners could either be R1, R2

5.2. Structural Design of the Cargo Transport System

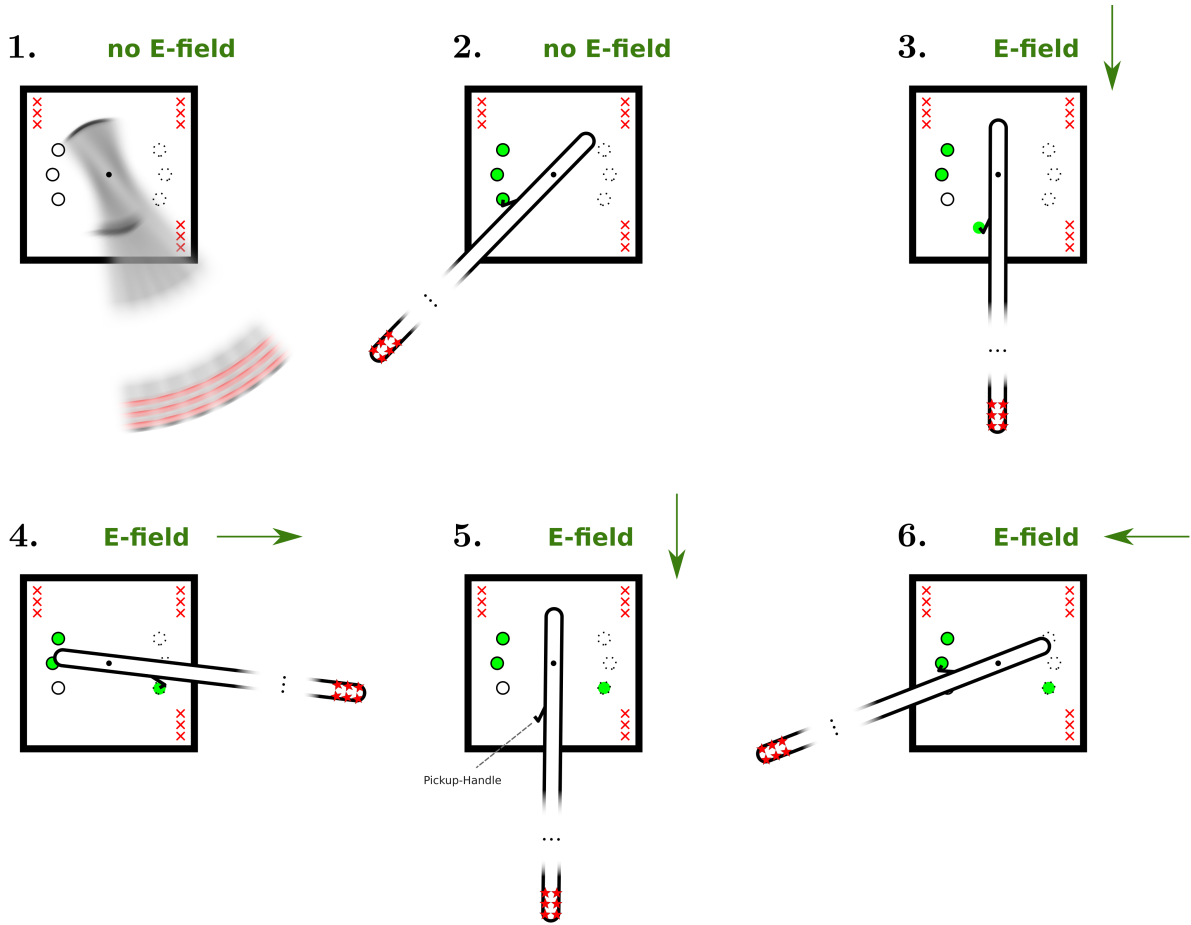


Figure 5.5. | Pickup and Transportation. The dynamics of the pointer is shown for an exemplary protocol to transport cargo-strands from the deposit-region to the target-region. Initially, no cargo-strands are present and the pointer fluctuates without an electric field (1). After loading the deposit-handles with cargo-strands, the pickup-handle binds to the cargo-strands, resulting in the pointer to stay localized (2). When applying an electric field, the cargo-strand is picked-up by the pickup-handle, as the electric field exerts torque on the arm (3). The field is then rotated so that the arm points towards the target-region, where the cargo-strand hybridizes to a target-handle (4). The cargo-strand is then dropped off at a target-handle, as the electric field again exerts torque on the arm (5). To pickup more cargo-strands, the electric field must be rotated in opposite direction, so that the arm points towards the deposit-region (6). Steps 3 – 6 can be repeated until all cargo-strands are transported from the deposit-region to the target-region.

5. Experimental Part

or both combined. If the marker is utilized for drift-correction only, then 3 docking-handles for each corners of either R1 or R2 were implemented. However, when using the marker for alignment as well, both types of docking-handles R1 and R2 were used simultaneously. To obtain equal contrast independent of the imager species, only one docking-handle per corners and imager-type was implemented.

Overall this marker-structure containing only one docking-handle per corner and imager type was not reliable and showed low brightness compared to other structures of the sample. This becomes even more apparent when comparing it to the CQO in Fig. 5.3, which has 3 docking-handles per corner. There the signal-to-noise ratio is lower and all 3 corners can be seen for all structures.

Furthermore, when using this marker together with roboarm, it could easily be confused with the roboarm, which also partially used R1 imager for the corners.

For these reasons, an improved marker was designed (see Fig. 5.6b)), that could be used for drift-correction and the alignment for the fluorophore A655 and for both R1- and R2-imager. This marker uses the same baseplate as the roboarm, but does not utilize the docking-handles at the corners. The R1- and R2-docking-handles were placed in a checkerboard pattern, containing in total 44 docking-handles. The A655-fluorophore, was placed on the bottom-side of the marker. This marker had the advantage of being much brighter compared to the previous marker, because it contained more than seven times as many docking-handles. However, because the docking-handles were too closely together, blinking events could not be assigned to the corresponding docking-site, which thus led to lower resolution. A practical solution is to use more of the marker.

Throughout all measurements shown here, the improved version of the marker was used.

5.3. Cargo Loading- and Transporting-Protocol

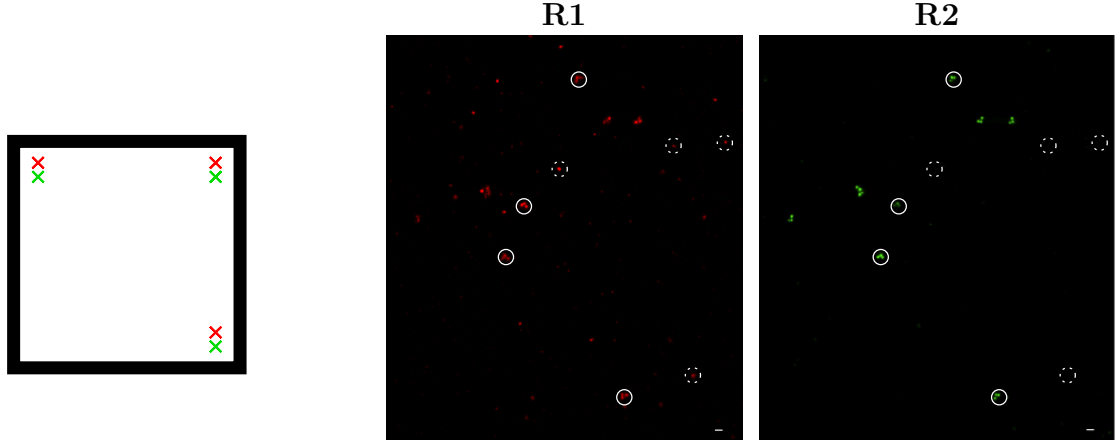
A reliable cargo-loading procedure is critically for the setup of transporting cargo-strands from the deposit-handle to the target-handle. The roboarm is successfully loaded when cargo-strands are attached to the deposit-handles only but not to the target-handles. This chapter introduces three cargo-loading protocols:

- the *simple protocol*
- the *Post-Blocking-Cargo-Loading* protocol
- the *Pre-Blocking-Cargo-Loading* protocol

The starting point is given by a sample, in which roboarms are bond to the PEG-coated glassslide. The loading procedure consisted of sequential buffer exchange steps, that contain cargo-strands or other auxiliary strands. Between each buffer exchange, the

5.3. Cargo Loading- and Transporting-Protocol

a)



b)

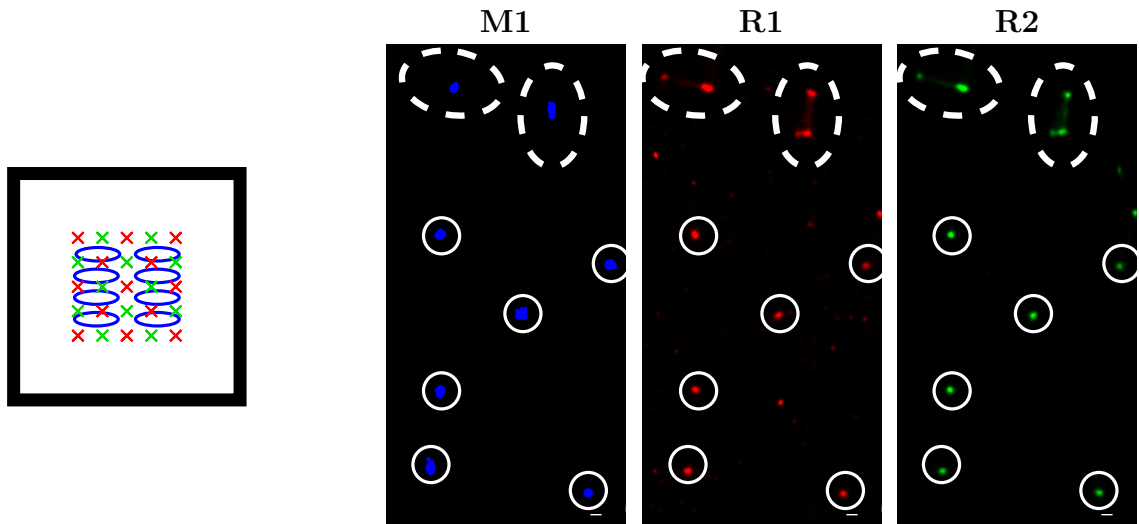


Figure 5.6. | Marker Comparison. Shows two types of marker-structures tested in the scope of this thesis. **a**, only 3 PAINT-handles for both, R1 and R2, were used for three corners of the baseplate. The white solid-line circles show correctly identified markers. The white dashed-line circles show markers, that were only identified in R1 but not in R2. **b**, different marker that uses more PAINT-handles for M1, R1 and R2, that are all localized in the middle of the baseplate. M1 is a direct label with A655-fluorophore. Here, the white dashed-line ellipses show marker, that are too close together to be distinguishable without PAINT-techniques. The white solid-line circles show markers, that were correctly identified for M1, R1 and R2. Overall, a much higher signal-to-noise ratio and fewer unidentifiable markers were seen in **b** compared to **a**, as more PAINT-handles were implemented. Scalebar: 100 nm

5. Experimental Part

sample is thoroughly flushed with a neutralizing buffer that does not contain any DNA-strands, to remove any unbound strands. Finally, when the roboarms are supposedly loaded, the sample is flushed with an imaging buffer.

For simplicity, let us define domains of sequences that are similarly used on all involved strands. Domains are denoted by a capital letter **A** and their reverse-complement $\overline{\mathbf{A}}^*$. Different naming of multiple domains suggest, that they are orthogonal to each other. They are read from 5' to 3'.

The *simple protocol* consists in exchanging the buffer of the chamber for a short period of time. The exchanging-buffer contains cargo-strands in low concentration, that contain a domain **C** that can bind to the deposit-handles, the target-handles or both. In addition, the cargo-strands have a domain **PH**, which can hybridize with the pickup-handles (see Fig. 5.8a)). However, as only roboarm-structures with just the deposit-handles loaded are of interest, this protocol would yield in the best case scenario only 25 % of correctly loaded roboarms. Furthermore, the yield depends on a multitude of parameters, like the cargo-strand concentration, the temperature or the duration of the cargo-strands being exposed to the deposit-handles , making reproducible cargo-loading very difficult.

The *post-blocking-cargo-loading* protocol and the *pre-blocking-cargo-loading* protocol try to solve these challenges. Both protocols are more robust against external parameters and allow nearly perfect yield for correctly loaded roboarms. They are based on the principle of toehold mediated strand displacement (see Section 2.4.1). For that, the deposit-handles and target-handles have different sequences, enabling the insertion of toeholds only for specific handles.

5.3.1. Post-Blocking-Cargo-Loading

In the *post-blocking-cargo-loading* protocol, all deposit-handles and target-handles are first blocked using blocker-strands with sequence $\overline{\mathbf{D2}}^* \overline{\mathbf{C2}}^*$, which hybridizes to the common domain **C2** of the handles. The blocker-strands are first flushed into the chamber. The deposit-handles have additionally a toehold **B2**. Once all deposit- and target-handles are blocked, the sample is flushed with an exchange buffer containing cargo-strands, that will only hybridize to the **B2** domain of the deposit-handles. After hybridization, toehold mediated strand displacement takes place between the invading cargo-strand and the protecting blocker-strand on the deposit-handles. Thus the blocker-strands, that were previously attached the deposit-handles, will dissociate, while simultaneously the cargo-strand hybridize with the deposit-handles. After all deposit-handles are loaded with cargo-strands, the sample is flushed with activator-strands. The activator-strands are consisting of the entire complementary sequence to the remaining blocker-strands at the target-handles. In a second toehold mediated strand displacement (TMSD) reaction employing the toehold **D2**, the activator strands invade and remove the blocker-strands from the target-handles. As a result, only the deposit-handles are loaded with cargo-strands while the target-handles remain single-stranded.

5.3. Cargo Loading- and Transporting-Protocol

An overview the secondary structure and the domains of all strands involved is given in Fig. 5.8b). This protocol has the advantage that it is much less time-dependent, as long as TMSD can take place. The displacement rates and stability of all involved strands mostly depend on their sequence. Therefore, this loading protocol provides a highly reproducible method for cargo-loading.

However, this protocol also comes with several drawbacks:

- When adding the cargo-strands with a too highly concentrated buffer, or for a too long exchange time, the cargo-strands can even displace the blocker-strands at the target-handles.
- The cargo-strand is strongly bound to the deposit-handle, because of the added base-pairs of the toehold formed at **B2**. Optimizing the sequence to favor the unzipping from the deposit-handle **B2C2** versus the shearing from the pickup-handle **PH** is therefore more difficult.
- Once the deposit-handle is loaded and the target-handle is activated, diffusive cargo-strands that remain in the sample chamber despite extended flushing can bind to the target-handle.

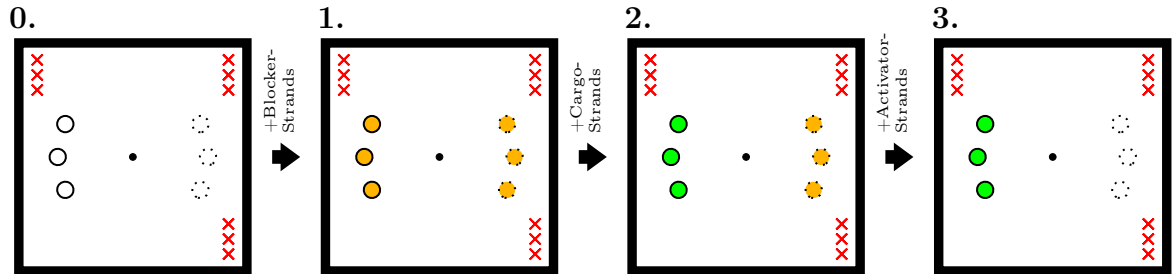
5.3.2. Pre-Blocking-Cargo-Loading

The *pre-blocking-cargo-loading* protocol is an attempt to further improve the cargo loading process. An overview of all strands involved is given in Fig. 5.8c). In this protocol, the cargo-strands are added in the first step, before the target-handles are protected with blocker-strands. Thereby the cargo-strands bond to the **C3** region of both deposit- and target-handle. Subsequently, the sample is flushed with a buffer containing blocker-strands $\overline{\mathbf{D3}}^* \overline{\mathbf{B3}}^* \overline{\mathbf{C3}}^*$. Thereby cargo attached to the target-handle are displaced while cargo attached to the deposit-handle remain. In the last step, activator-strands are added to remove the blocker strands again from the target-handle via TMSD.

Similarly to the *post-blocking-cargo-loading* protocol, cargo-strands are now only attached to the deposit-handle, while the target-handle is single-stranded. However, this protocol is much less sensitive to an upper limit of buffer exchange timings. If exceeding optimum buffer-exchange-times, blocker-strands could start spontaneously displacing the cargo-strand from the deposit-strand. This is less problematic than cargo-strands hybridizing to the target-handle, which would happen when exceeding buffer-exchange-times in the *Post-Blocking-Cargo-Loading* protocol. Another advantage of this protocol is, that it can be repeated multiple times, for example after (partially) successful transportation of cargo-strands from deposit-handle to the target-handle.

5. Experimental Part

a) Post-Blocking-Cargo-Loading Protocol



b) Pre-Blocking-Cargo-Loading Protocol

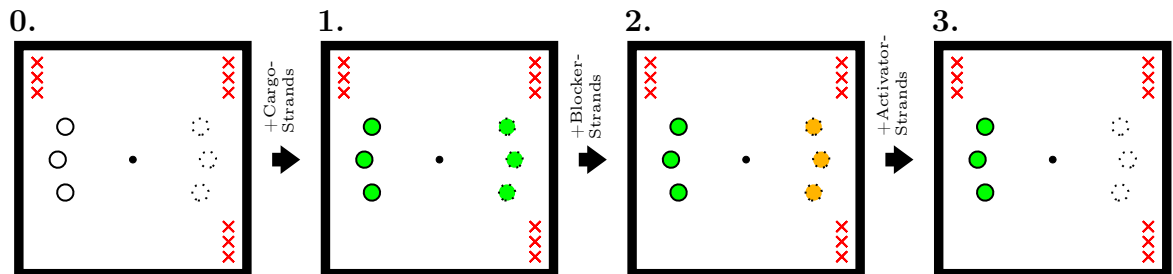


Figure 5.7. | Loading Procedure Strand Overview. The sequence of strands visualized for both loading procedures. PAINT-handles at the corners are shown as red "X". Deposit-handles have a solid-line edge, target-handles have a dashed-line edge. Deposit- or target-handles that have cargo-strands attached to are solid green. Deposit- or target-handles that have blocker-strands attached to are solid orange. In **a**, the blocker-strands are added in the first step (**1**). Cargo-strands displace the blocker-strands at the deposit-handles (**2**). Activator-strands bind to remaining blocker-strands. In **b**, the cargo-strands are added in the first step (**1**) and bind to both, the deposit- and the target-handle. Blocker-strands remove the cargo-strands from the target-handle (**2**) and are eliminated via activator-strands (**3**).

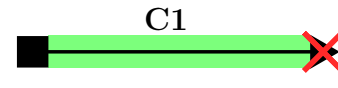
5.3. Cargo Loading- and Transporting-Protocol

a) Simple Protocol

Deposit-Handle



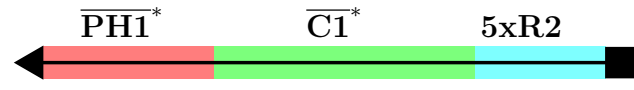
Target-Handle



Pickup-Handle



1. Cargo-Strand

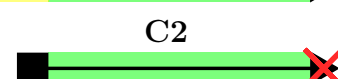


b) Post-Blocking-Cargo-Loading

Deposit-Handle



Target-Handle



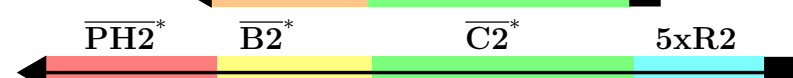
Pickup-Handle



1. Blocker-Strand



2. Cargo-Strand



3. Activator-Strand



c) Pre-Blocking-Cargo-Loading

Deposit-Handle



Target-Handle



Pickup-Handle



1. Cargo-Strand



2. Blocker-Strand



3. Activator-Strand

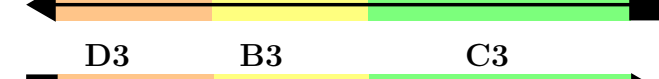


Figure 5.8. | Loading Procedure Strand Overview. All domains that are required for loading the cargo-strands to the deposit- or target-handle are visualized and color-coded accordingly. The red "X" represents the fixation to the baseplate. The blue "X" represents the fixation to the arm of the roboarm-structure. The blue domain is used for PAINT-measurements with R2-imager.

5. Experimental Part

5.3.3. Bulk loading

The loading procedure in bulk requires PEG or gel purification between each step. Bulk cargo-loading has the advantage to prepare activated roboarm structures for multiple experiments. However, it is unknown with what rate the cargo-strands dissociates from the deposit-handle. Furthermore, if any unbound cargo-strands remain in the sample despite purifications, they can bind to the target-handles. Thus, bulk cargo-loading does not provide a reproducible method loading cargo-strands on the roboarm. Thus, we chose to perform the loading procedure on the slide.

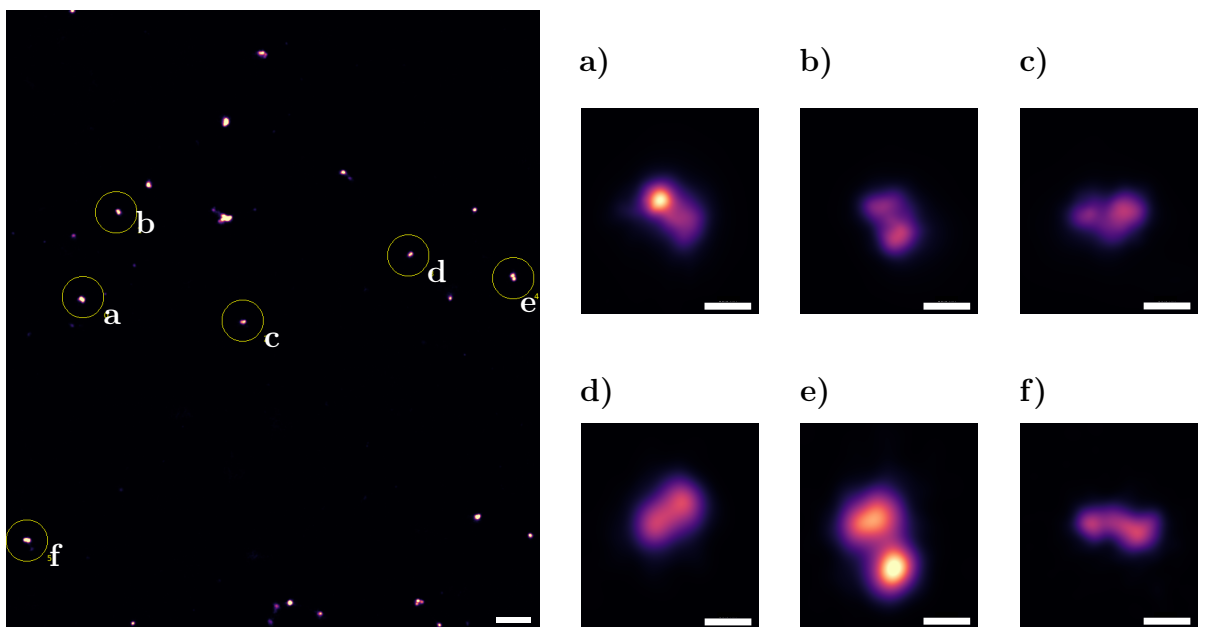


Figure 5.9. | Bulk Cargo Loading. Bulk Cargo Loading with the triple-cargo-stites implemented and loaded with the *Post-Blocking-Cargo-Loading* protocol. At this point, it is not activated. Scalebar left side: 500 nm. Scalebar in **a – f**: 50 nm

5.3.4. Visualization Domains

Regardless of the protocol used, the cargo-strands and the blocker-strands also included domains for PAINT that could be used for visualization in the transport experiments. For the cargo-strands, this was the **5xR2** domain, used for SpeedPAINT with R2-imager. For the blocker-strands, **D2*** or **D3*** could simultaneously incorporate a PAINT docking sequence. In this thesis, often the sequence for P1-docking handle was used for this purpose, as R1 was already used for the corners and R2 was utilized for the cargo-strands.

5.3.5. Cargo Transporting Protocol

The transport of the cargo-strand was tried out using electric fields that control the roboarm. The electric field was generated by applying voltages to 4 symmetrical electrodes in the chamber [20]. By varying the voltages $\vec{V}(t) = (V_x(t), V_y(t))^\top$, one could vary the alignment and magnitude of the electric field. The electric field was primarily used to apply a torque on the pointer of the roboarm, that should lead to the unzipping of the cargo-strand from the deposit-handle. The cargo-transporting-protocol provides a time-dependent function $\vec{V}(t)$ that should increase the probability of successful pickup (see Sect. 4.1.1). For defining such a protocol, it is assumed that all roboarms on the slide are loaded and activated. Moreover, the pickup-handle has hybridized with the cargo-strand at the deposit-handle, thereby fixing the pointer as well.

With an electric field also comes a current caused by the ions in the buffer. This current heats up the sample, eventually leading to structural damage of the DNA nanostructures due to melting of individual staples [75]. Thus, the temperature increase was the limiting factor restricting the maximal power performed by the arm.

A constantly rotating electric field is an intuitive protocol that could be used for cargo-transportation. However, the induced torque is maximized when the electric field is aligned perpendicular to the pointer of the roboarm (see eq. 3.4). Using a constantly rotating electric field, the time duration where a high torque is exerted is very confined.

For that reason, the electric-field was aligned in 1-dimension only. Since the roboarm-structures are aligned randomly on the slide, only few pointers were oriented perpendicular to the electric field. However, even if not perfectly aligned, the pointers experience the torque for a longer duration, compared to a constantly rotating electric field. This should increase the probability of the cargo-strand to successfully unzip from the deposit-handle.

To prevent excessive heating, the 1-dimensional electric field was driven using a pulse-width-modulated (PWM) signal.

$$\begin{aligned} V_x(t) &= 0 \\ V_y(t) &= \begin{cases} V_0 & , n \cdot T < t < n \cdot T + PW_{\text{on}} \mid n \in \mathbb{N} \\ 0 & , \text{else} \end{cases} \end{aligned} \quad (5.3)$$

with the periodic time $T = PW_{\text{on}} + PW_{\text{off}}$ where PW_{on} and PW_{off} are the duty cycles of the on- and off-time respectively. In the off-time, no electric field is present so the sample can cool down. This phase is called the *cool-down phase*. An example of this function is shown in Fig. 5.10.

Finally, the buffer composition can be varied. For example, the valency of ions in the buffer can influence the shielding of the negatively charged backbone of the pointer, reducing the effective torque applied by the electric field [44].

5. Experimental Part

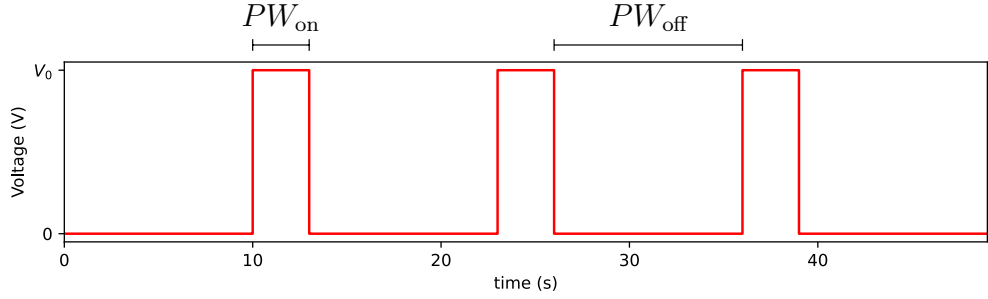


Figure 5.10. | PWM Example.

5.4. Attempts of Cargo-Transport

When attempting to perform cargo-transportation in experiments, one could either follow the process by tracing the fluorescent tip of the pointer or one could determine the cargo position using DNA-PAINT. Measuring the pointer gives instant feedback of the position of the pointer, giving insights into the dynamics of cargo-transportation. However, interpreting the position of the pointer gives only implicit interpretation of the cargo-strand. On the other hand, measuring the cargo-strands via SpeedPAINT provides explicit information about the position and thus is a straightforward approach to verify potential cargo-transportation. In the current experimental design, the same fluorescence channel was employed for both tracking and PAINT imaging. Therefore it was not possible to perform both types of measurements within the same experiment.

This section presents some promising examples of two attempted cargo-transportation experiments, using both analysis methods: observing the pointer only or detecting the cargo-strands via SpeedPAINT. The data shown in Fig. 5.11 and Fig. 5.12 provide an excerpt of the data collected in a TIRFM measurement.

5.4.1. Cargo transport experiments (pointer tracking)

Fig. 5.11 shows an attempt to transport cargo-strands in which the fluorophore of the High-Aspect-Ratio-Pointer was detected while applying an electric PWM voltage in y-direction. The *cargo-transporting-protocol* consisted of 5 PWM pulses with $PW_{on} = 2$ s in negative y-direction ($\hat{=} \frac{3\pi}{2} \text{rad} = 270^\circ$), followed by 5 PWM pulses with $PW_{on} = 2$ s in positive y-direction ($\hat{=} \frac{\pi}{2} \text{rad} = 90^\circ$). In between the pulses, the sample could cool down for $PW_{off} = 3$ s. The voltage in y-direction is plotted in Fig. 5.11c).

In the experiment shown in Fig. 5.11, the triple-cargo-site was implemented and loaded via the *post-blocking-cargo-loading* protocol. For both picked roboarms, the angle is plotted with respect to time in Fig. 5.11a-b). Angles of interest are visualized with colored, horizontal lines in the plots. At these angles, the assumed alignment of the pointer is sketched in the localization histogram in Fig. 5.11a-b), using the corresponding color from the horizontal lines in the plots.

5.4. Attempts of Cargo-Transport

The angle of the High-Aspect-Ratio-Pointer during the first 2 s in fig. 5.11a-b) shows the position of the pointer, before any external force was exerted. In the case of the two picked examples, the pointers appear fixated at absolute angles of 248° for a) and 208° for b). This suggests that the pickup-handle of the pointer did hybridize with a cargo-strand which in turn is attached to a deposit- or target-handle on the baseplate.

When applying the first 5 PWM pulses in negative y-direction, both pointers in fig. 5.11a-b) instantly align towards the electric field. In the cool-down phases in between the PWM pulses, the pointer immediately snaps back to the steady state, resting position. This indicates, that a rupture from the cargo-strand has not occurred yet. Instead, the change of the pointer angle is very likely the result of pointer-bending. This is supported by the fact that the pointer in Fig. 5.11b) was aligning less to the electric field than Fig. 5.11a) (248° for b) and 262° for a)), as b) was starting from a more horizontal angle and thus experienced more bending, compared to a).

When applying the electric field in positive y-direction, the two selected particles behave differently, indicating two slightly different transport processes.

For Fig. 5.11a), the pointer orients at 180° during the first PWM pulse in positive y-direction, but then snaps back again to the initial position during the cooldown-phase. This again indicates possible pointer-bending. In the second PWM pulse in positive y-direction, the pointer stays only shortly at 180°, before abruptly increasing the angle to 115°. This event suggests a rupture from the cargo-strand. From this point on, the pointer alternates between 115° and 138°, depending on whether a PWM pulse or a cool-down phase is present. The new resting position at 138° indicates, that the pickup-handle of the pointer has hybridized again to a cargo-strand. Thus, it could be speculated, that a cargo-strand was transported from the deposit-area to the target-area. The difference of angle between the initial position and the final position is 111° and therefore well in agreement with the theoretical proposed angle of $\approx 130^\circ$. The pictogram in Fig. 5.11a) summarizes this interpretation. The pictogram is rotated so that the pointer is aligned above a deposit- or target-handle when the pickup-handle is hybridized to a cargo-strand. For this interpretation, it was assumed that cargo-strands only bound to the deposit-handles and were blocked successfully from the target-handles.

In Fig. 5.11b), the pointer is first localized at 155°, as soon as the first PWM pulse in positive y-direction is applied. Towards the end of the first PWM-pulse in positive y-direction, the angle of the pointer abruptly increases to 105°. This suggests, that the localizations at 155° were caused by pointer-bending, before eventually rupture occurred. In the cool-down phase that follows the first PWM pulse in positive y-direction, the pointer remains at 155°. This suggests, that the pickup-handle of the pointer is now hybridized to a cargo-strand at another position. However, the angular difference of 53° between the initial resting position and the newer resting position after applying PWM pulses in positive y-direction is too small for a transportation from the deposit-area to the target-area. This could be explained by a cargo-strand being transported from one deposit-handle to the outer deposit-handle at the other side, as visualized in the

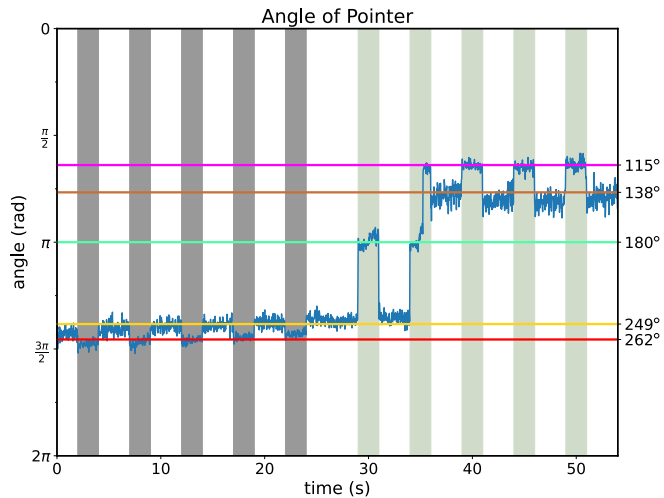
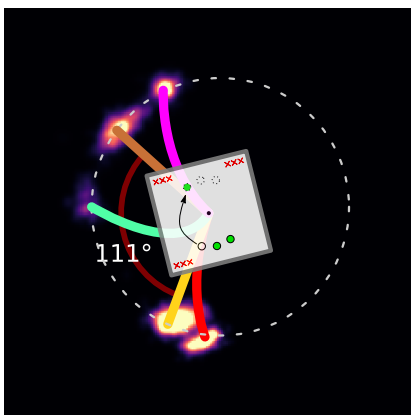
5. Experimental Part

pictogram in Fig. 5.11b). This could for example happen, when the not all deposit-handles were correctly loaded and thus a cargo-strand could potentially bind to a free deposit-handle during transportation.

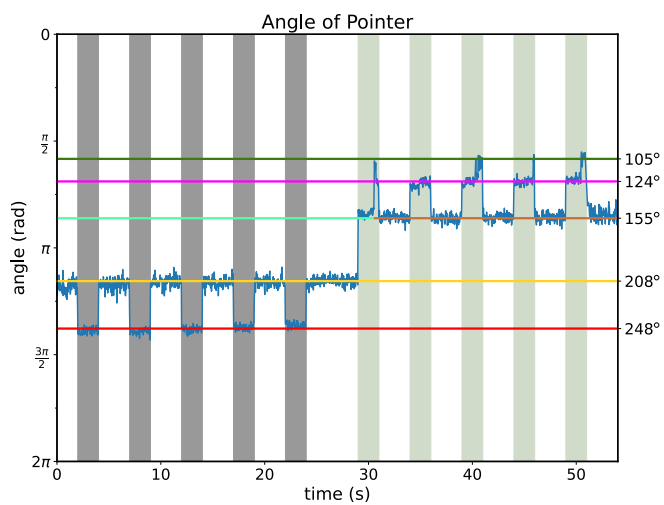
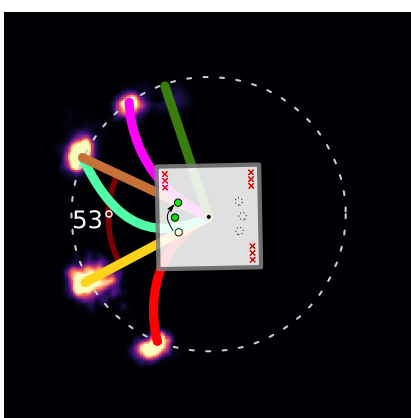
Furthermore, the pointer in Fig. 5.11b) alternates between 124° and 105° during the PWM pulses in positive y-direction. This could be explained by two phenomena. Since the alignment at 124° is not delayed with a PWM pulse, it is thought to be the result of pointer-bending, while the pickup-handle stays hybridized to a cargo-strand. Towards the end of the PWM pulses in positive y-direction, the pointer further aligns to the electric field up to 105° . As this consistently occurred towards the end of pulses, it could be speculated to be result of rupture from the pickup-handle away from the cargo-strand, for example due to heating.

The two picked examples in Fig. 5.11a-b) suggest, that a rupture of the cargo-strand does occur. This is important to show that the applied electric field is strong enough to rupture cargo-strands placed on the baseplates. Whether the cargo-strands thereby unzip from the deposit-handles, or the pickup-handle shears away from the cargo-strands can only be speculated at this point. The experiment in Sect. 5.4.2 tries to give a better insight into the transportation-mechanism.

a)



b)



c)

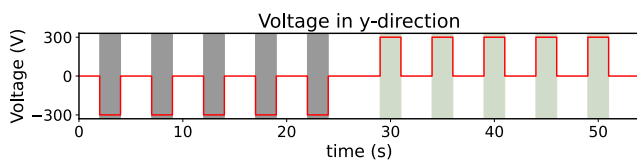
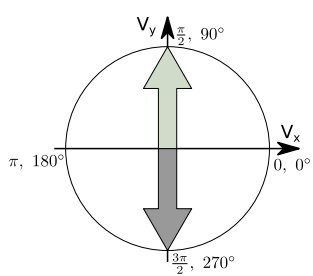


Figure 5.11. | Cargo transport experiment (pointer tracking). Localizations of the High-Aspect-Ratio-Pointer during the *cargo-transporting-protocol* for two selected roboarm-structures are shown in **a** and **b**. Pictograms of the roboarm-structure are shown in the localization-images. The pictograms are positioned in the origin of the fitted dashed circles. The rotation of the baseplate, the position of cargo-strands, the alignment and deformation of the High-Aspect-Ratio-Pointer are result of the interpretation given in Sect. 5.4.1. The colors of the pictogram correspond to the states in the trajectories on the right side. In **c**, the PWM-signal for the *cargo-transporting-protocol* is shown. On the left side of **c**, the direction of the PWM-pulses is shown as well as the convention for the coordinate system. The pictograms drawn are not to scale.

5.4.2. Cargo transport experiments (cargo tracking)

Fig. 5.12 shows two selected proximate roboarms in another attempt of cargo/transport. The starting point was based on loaded roboarms via *post-blocking-cargo-loading* with triple-cargo-sites for deposit- and target-handles. Like in previous experiments, the deposit- and target-handles were activated on-slide. However, a different *cargo-transporting-protocol* was used compared to the previous transportation attempt in sect. 5.4.1. In the experiments shown here, 15 PWM-pulses ($PW_{on} = 4\text{ s}$ and $PW_{off} = 2\text{ s}$) only in positive y-direction were applied, as plotted in Fig. 5.12b). Furthermore, the fluorophores of the pointer was bleached before the transport protocol was applied to allow DNA PAINT-imaging. Instead, the cargo-strand was measured using SpeedPAINT before and after performing the *transportation-protocol*. To obtain the orientation of the structures, the corners of the baseplate were measured additionally.

Fig. 5.12a) shows the drift-corrected super-resolved image of the three PAINT measurements taken. The measurements were aligned and overlayed with each other. High-precision alignment was only possible by utilizing MCQO-structures. These structures, as well as other roboarms, are not visible in the magnified views shown in Fig. 5.12.

To better understand whether cargo-strands are attached to the deposit- or the target-handles, the cargo-strand measurements are individually shown for both picked roboarms separately in Fig. 5.11c-d). The shown measurements are split into 3 categories:

- Activated: showing the cargo-strands after being activated via TMSD using activator-strands, prior to applying any electric field.
- Transported: showing the positions of the cargo-strands after applying the *transportation-protocol*. The *transportation-protocol* was performed using the EB-buffer.
- Combined View: showing an overlay of the cargo-strands from the activated- and transported-measurements. It should help tracing the cargo-strand from the deposit-handle to the target-handle.

The pictograms in Fig. 5.12c-d) should visualize a possible explanation for the observations from the activated- and transported-measurements. The orientations are roughly aligned to the corners that can be seen in Fig. 5.12a).

In the measurement for the activated structures, both picked structures have all cargo-strands localized in a single region. This suggests, that the activation was successful for these structures. The activated cargo-strands in Fig. 5.12c) are elliptically shaped, which could indicate, that all 3 deposit-sites of this structure are loaded with cargo-strands. In contrast, the localizations for the activated cargo-strands in Fig. 5.12d) are more densely packed together compared to Fig. 5.12c), which could be a sign of a missing cargo-strand one of the deposit-handles.

After applying the *transportation-protocol*, the cargo-strands for both picked roboarms are clearly visible in two separate regions (Transported View of Fig. 5.12c-d)). Based

5.4. Attempts of Cargo-Transport

on the orientation of the structure shown in c), a cargo-strand is likely to have attached to a target-site. It could be speculated, that the pointer did successfully transport a cargo-strand from the deposit-site to the target-site.

However, for the structure shown in d), the orientation does not indicate that a cargo-strand is bound to a target-site. Still at least two separate cargo-strands are visible. This could be explained by a cargo-strand switched from the middle deposit-site to the other outer deposit-site. If both outer deposit-sites are occupied by cargo-strands, they are 18.6 nm distant from each other and could then theoretically be distinguished from another using SpeedPAINT. The switching from the middle deposit-site to the outer deposit-site could as well be the result of transportation via the pointer. However, this would not explain why the cargo-strand would not unzip again from the outer deposit-site and be transported to a target-site. It could be speculated that the pickup-handle that was bound to the cargo-strand was ruptured due to the heating that was caused by the electric current.

The orientation of both structures has as a result, that the cargo-strands that are assumed to be transported by the pointer, are roughly perpendicular at the deposit-sites with respect to the direction of the electric field (77° for c) and 111° for d)). This would result in a maximal torque exerted by the pointer as a consequence of the electric field which would make a successful pickup of cargo-strands more reasonable.

This experiment yields very promising results that do indicate that cargo-transportation could be possible. Furthermore, this experiment shows the importance of a reliable cargo-loading-protocol and also confirms the validity the *pre-blocking-cargo-loading* protocol. Finally, it was also one of the reasons for the redesign of the deposit-handles from triple-cargo-site to single-cargo-site, as latter yields a more discrete signal regarding the position of the cargo-strand.

However, it must be stressed, that such structures indicating potential cargo-transportation were the exception throughout all experiments performed.

5. Experimental Part

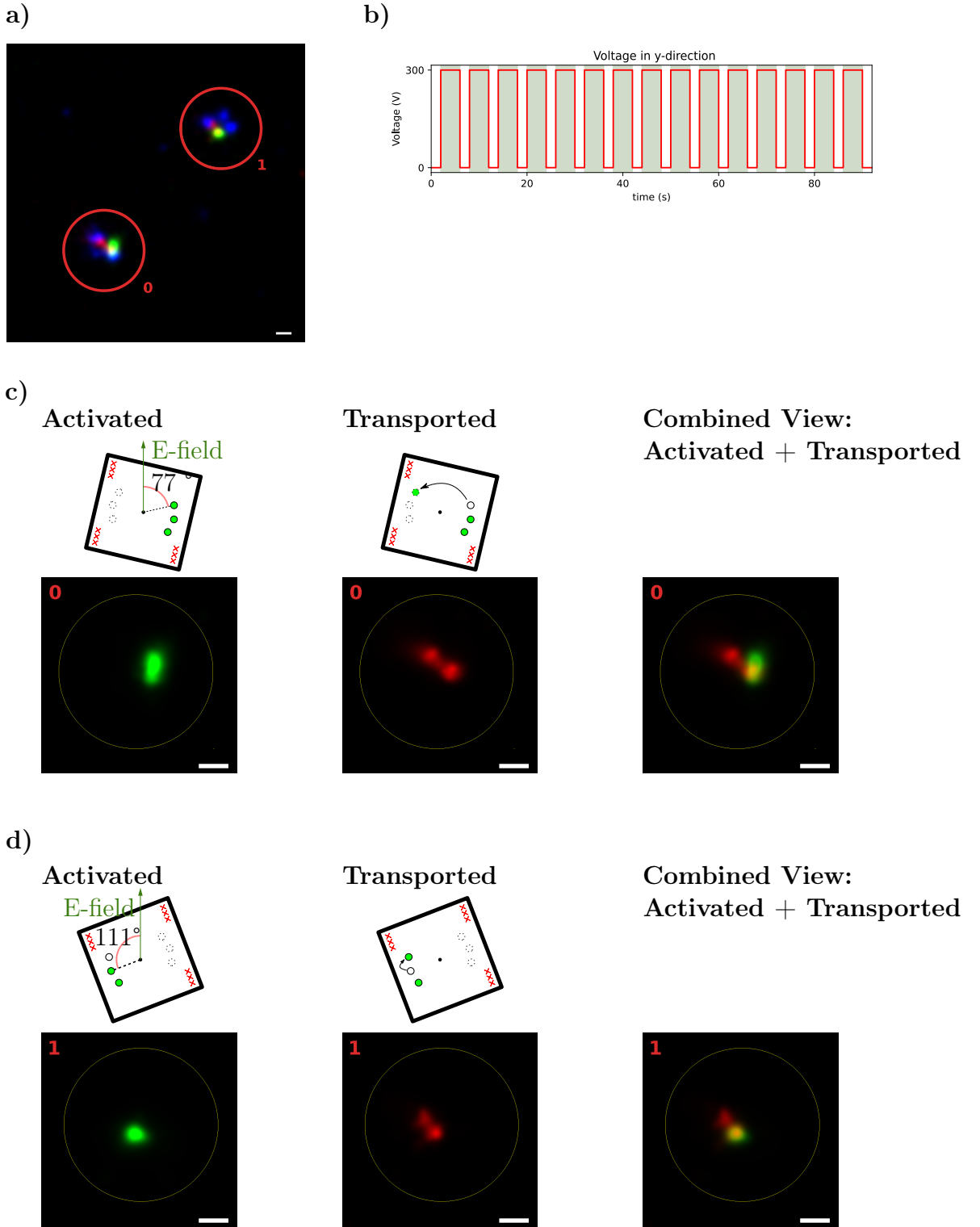


Figure 5.12. | Cargo transport experiment (cargo tracking). Overlay of all SpeedPAINT-measurements is shown in **a**. Visualized are the corners of the baseplate (blue) and for the cargo-strands before (green) and after (red) performing the *cargo-transporting-protocol*. In **b**, the PWM-signal for the *cargo-transporting-protocol* is shown. **c** and **d** shows an isolated view of the SpeedPAINT-measurements of the cargo-strands for the selected particles 0 and 1 respectively. The pictograms in **c** and **d** are rotated to approximately align to the measured corners. Here, the High-Aspect-Ratio-Pointer that was used in the experiments was not drawn in the pictograms. The combined view presents an overlay of the cargo-strand measurements. Scalebar: 50 nm

5.5. Conclusion

In this chapter, we developed DNA nanorobots that are able to transport cargo DNA. Despite being unreliable and returning only a low yield of transported cargo, we showed that the transportation mechanism does in principle work.

In this chapter, we developed DNA nanorobots for the transport of a DNA cargo. Experimental data of individual nanorobots suggests a successful transport. However, this successful transport was only observed for a small fraction of the observed nanorobots. To mitigate these low yields, we introduced multiple variations of these nanorobots, storing up to 3 cargo-strands. The cargo-strands were stored on designated deposit-handles and were picked up by the arm. We formulated voltage protocols that would control an electric field and thereby exert torque on the arm, transporting the picked-up cargo-strands to designated target-handles.

We developed methods to assemble the starting configuration, where only the deposit-handles are loaded with cargo-strands, while preserving the target-handles. In order to locate the cargo-strands, we adapted and optimized DNA-PAINT-methods to our nanorobots.

For that purpose, we developed auxiliary nanostructures, that improved the post-processing of recorded PAINT localizations and thus increase spatial resolution.

5.6. Outlook

This section lists possible improvements for further research and development using the roboarm to transport DNA cargo.

Single- or Dual-Cargo-Handles

Triple-cargo-sites provides redundancy for the cargo-transportation process, as successful transportation of any one of the three stored cargo-strands will result in two distinguishable spots. However, implementing three deposit-handles as well as three target-handles makes reproducible cargo-loading more challenging for two reasons:

- If any cargo-strands are attached to the target-handle after activation, then these structures become invalid for potential transportation since a picked-up cargo-strand cannot bind to an already occupied target-handle. With more target-handles, the probability of cargo-strands being wrongfully hybridized to a target-handle after activation increases.

5. Experimental Part

- Implementing more deposit-handles also increases the chance that not all deposit-handles will be loaded with cargo-strands. This can result in cargo-strands being transported from one deposit-handle to another deposit-handle, as was the case in Fig. 5.12d).

Thus, decreasing the number of cargo-sites should make the cargo-loading procedure easier and also provide a more robust output-signal to identify successfully transported cargo-strands.

A single-cargo-site variation was already developed in the scope of this thesis (see Sect. 5.2.1), but further studies are required to evaluate the quality compared to triple-cargo-sites. Unfortunately, the release of the cargo-strand at the target-handle is more difficult to assess, since only one cargo-strand can be transported.

Dual-cargo-sites were not developed yet, but could potentially be an efficient compromise between the single-cargo-site and the triple-cargo-site.

Visualization of Deposit-Handles

Implementing a SpeedPAINT-handle adjacent to the deposit-handles could be useful to verify cargo-transportation more easily. Using another orthogonal PAINT-sequence (e.g. the **R3**-sequence were not yet used) provides more flexibility.

Cargo-Transporting-Protocol

All cargo-transporting-protocols used voltage curves based on PWM-signals introduced in Sect. 5.3.5. The PWM-signals did solve the problem of overheating, however, they were only applied in y-direction of the sample. It is thought that an updated voltage protocol could return a better yield for successfully transported cargo-strands. For example, the PW_{on} signal could be extended with a rotating, low-power electric field, transporting the cargo-strand to the dedicated target-handles. An updated voltage protocol could also incorporate repetitions at different angles, so that more of the randomly orientated nanorobots will be addressed.

Multiple Fluorophore Channels

When utilizing multiple fluorescence channels, the pointer could be measured independently of PAINT-imager. Therefore, it would not be required to bleach the pointer anymore, when measuring activated cargo-strands prior applying the cargo-transporting-protocol. This was briefly tested during this thesis and provided promising results.

Torque Optimized Pointer

Developing and implementing pointers that exert more torque on the pickup-handle increases the probability of successful pickup of cargo-strands from the deposit-handle. This is motivated by three reasons:

- A weaker electric field is required, thus a lower voltage is applied and less heating occurs.
- Since the unzipping probability is expected to scale exponentially with pulling force, (as was observed in the simulations in Fig. 4.6b)), small increase in torque would probably lead to a much higher rate of successful pick-ups.
- When more force is available, then the deposit-, target- and pickup-handle can be designed with a longer sequence and thus more base-pairs, compared to the design-choice used in this thesis. With more base-pairs, the difference of force required for shearing versus unzipping a duplex increases (before the difference converges starting from $\approx 20\text{bp}$ as simulated in [27]).

6. Conclusion

In this thesis, we investigated the physical and mechanical properties of the nanorobotic structure by performing coarse-grained molecular dynamic simulations with oxDNA. Thereby we found, that the joint of the nanorobot acts similar to a torsional spring that follows Hooke's law. We found, that mechanical energy can be stored in the joint when winding up the arm. We showed how variations of the joint influence the torsional spring coefficient and the range of motion of the joint. The simulations provided insights into internucleotide interactions during wind-up.

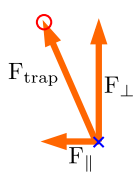
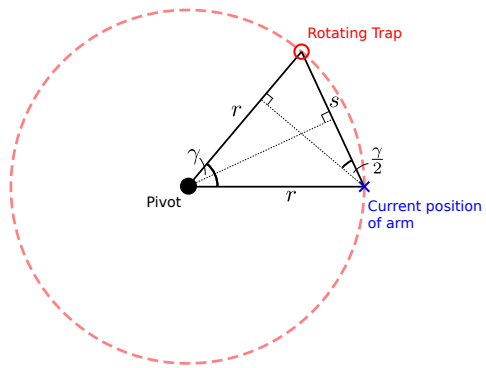
Furthermore, we designed and experimentally tested a nanorobot that is able to transport single-molecular cargo. The nanorobot was controlled using an electric field. Auxiliary nanostructures based on the baseplate of the nanorobotic structure were designed to improve imaging resolution. Several implementations for the deposit-, target- and pickup-handle were tested to increase the probability of a successful cargo-transport. The sequences for these handles were tuned using massively parallelized simulations in oxDNA. The experiments suggest, that single-molecular cargo is transported. However, at the current stage, successful cargo-transport is still unreliable and happens at a low yield.

The parallelized simulations that were used for sequence tuning provided insights into the dynamics cargo-pickup-process. The simulations showed under which conditions a successful cargo-pickup is more likely. We found that the dynamics of competing rupture of a three-strand-system cannot be treated as the combined rupture of two isolated sub-systems together.

In this thesis, we have set the foundations for a cargo-transporting nanorobot. We expect, that the yield for successfully transported cargo can be vastly increased by tuning the sequences using the parallelized simulations as well as by implementing the suggestions listed in Sect. 5.6.

A. Appendix

A.1. Radial- and tangential component of rotating harmonic traps



$$\begin{aligned} F_{\text{trap}} &:= F = ks & \} \\ \frac{s}{2r} &= \sin\left(\frac{\gamma}{2}\right) & F = 2kr \sin\left(\frac{\gamma}{2}\right) \end{aligned}$$

$$F_{\parallel} = F \sin\left(\frac{\gamma}{2}\right) = 2kr \sin^2\left(\frac{\gamma}{2}\right) = kr(1 - \cos\gamma)$$

$$F_{\perp} = F \cos\left(\frac{\gamma}{2}\right) = 2kr \sin\left(\frac{\gamma}{2}\right) \cos\left(\frac{\gamma}{2}\right) = kr \sin\gamma$$

A. Appendix

A.2. Sample oxDNA Input File

```
#####
##### PROGRAM PARAMETERS #####
#####
interaction_type=DNA2
salt_concentration=1.0
sim_type = MD
backend = CUDA
backend_precision = mixed
max_density_multiplier = 10
#debug = 1
seed = 42
fix_diffusion = 0
#####
##### SIM PARAMETERS #####
#####
steps = 1e10
ensemble = nvt
thermostat = john
T = 20C
dt = 0.005
verlet_skin = 0.5
diff_coeff = 2.5
newtonian_steps = 103
CUDA_list = verlet
CUDA_sort_every = 0
use_edge = 1
edge_n_forces = 1
#####
##### INPUT / OUTPUT #####
#####
topology = ...
conf_file = ...
lastconf_file = ...
trajectory_file = trajectory_out.dat
refresh_vel = 1
#log_file = log_trap.dat
no_stdout_energy = 0
restart_step_counter = 1
energy_file = energy_out.dat
print_conf_interval = 100000
print_energy_every = 10000
time_scale = linear
external_forces = 1
external_forces_file = ...
```

A.3. **Buffers**

- NaB: 1 M NaCl, 1xTAE
- NaB + PEG: 1 M NaCl, 1xTAE, 11% (W/V) PEG 8000
- FOB20: 10xTE, 0.2 M MgCl₂, 0.05 M NaCl
- FB20: 10xTAE, 0.2 M MgCl₂
- EB: 6 mM MgCl₂, 0.5xTBE
- BufferC (PAINT-buffer): 500 mM NaCl, 1xPBS, [1 mM EDTA], 0.07% Tween20
- Anti-Bleach Buffer: 2 mM Trolox, target buffer, 50 nM PCD, 2.5 mM PCA

A.4. **Sequences**

All sequences used in this thesis are available at

<https://github.com/gouderm/MSc-DNA-Nanorobots-Directed-Molecular-Transport-and-In-Silico-Studies-of-a-Molecular-Torsion-Spring>.

Bibliography

- [1] Wiktionary, “robot — wiktionary, the free dictionary,” 2021. [Online; accessed 22-October-2021].
- [2] M. Karásek, F. T. Muijres, C. De Wagter, B. D. W. Remes, and G. C. H. E. de Croon, “A tailless aerial robotic flapper reveals that flies use torque coupling in rapid banked turns,” *Science*, vol. 361, pp. 1089–1094, 9 2018.
- [3] K. Y. Ma, P. Chirarattananon, S. B. Fuller, and R. J. Wood, “Controlled flight of a biologically inspired, insect-scale robot,” *Science*, vol. 340, no. 6132, pp. 603–607, 2013.
- [4] G. M. Whitesides, J. P. Mathias, and C. T. Seto, “Molecular self-assembly and nanochemistry: a chemical strategy for the synthesis of nanostructures,” *Science*, vol. 254, pp. 1312–1319, 11 1991.
- [5] A. C. Mendes, E. T. Baran, R. L. Reis, and H. S. Azevedo, “Self-assembly in nature: using the principles of nature to create complex nanobiomaterials,” *Wiley Interdisciplinary Reviews: Nanomedicine and Nanobiotechnology*, vol. 5, pp. 582–612, 11 2013.
- [6] B. Alberts, A. Johnson, J. Lewis, M. Raff, K. Roberts, and P. Walter, “Protein function,” in *Molecular Biology of the Cell. 4th edition*, Garland Science, 2002.
- [7] P. Nelson, *Biological physics*. WH Freeman New York, 2004.
- [8] N. C. Seeman, “Dna in a material world,” *Nature*, vol. 421, 2003.
- [9] N. C. Seeman, “Nanomaterials based on dna,” *Annual Review of Biochemistry*, vol. 79, pp. 65–87, 6 2010.
- [10] P. W. K. Rothemund, “Folding dna to create nanoscale shapes and patterns,” *Nature*, vol. 440, no. 7082, pp. 297–302, 2006.
- [11] S. M. Douglas, I. Bachelet, and G. M. Church, “A logic-gated nanorobot for targeted transport of molecular payloads,” *Science (New York, N.Y.)*, vol. 335, p. 831—834, February 2012.
- [12] J. J. Funke, P. Ketterer, C. Lieleg, S. Schunter, P. Korber, and H. Dietz, “Uncovering the forces between nucleosomes using dna origami,” *Science Advances*, vol. 2, p. e1600974, 11 2016.

Bibliography

- [13] D. Lei, A. E. Marras, J. Liu, C.-M. Huang, L. Zhou, C. E. Castro, H.-J. Su, and G. Ren, “Three-dimensional structural dynamics of dna origami bennett linkages using individual-particle electron tomography,” *Nature Communications*, vol. 9, 12 2018.
- [14] J. J. Funke and H. Dietz, “Placing molecules with bohr radius resolution using dna origami,” *Nature Nanotechnology*, vol. 11, pp. 47–52, 1 2016.
- [15] J. List, E. Falgenhauer, E. Kopperger, G. Pardatscher, and F. C. Simmel, “Long-range movement of large mechanically interlocked dna nanostructures,” *Nature Communications*, vol. 7, 11 2016.
- [16] A. E. Marras, L. Zhou, H.-J. Su, and C. E. Castro, “Programmable motion of dna origami mechanisms,” *Proceedings of the National Academy of Sciences*, vol. 112, pp. 713–718, 1 2015.
- [17] P. Ketterer, E. M. Willner, and H. Dietz, “Nanoscale rotary apparatus formed from tight-fitting 3d dna components,” *Science advances*, vol. 2, p. e1501209, February 2016.
- [18] H. R. Singh, E. Kopperger, and F. C. Simmel, “A dna nanorobot uprises against cancer,” *Trends in Molecular Medicine*, vol. 24, pp. 591–593, 7 2018.
- [19] S. Li, Q. Jiang, S. Liu, Y. Zhang, Y. Tian, C. Song, J. Wang, Y. Zou, G. J. Anderson, J.-Y. Han, Y. Chang, Y. Liu, C. Zhang, L. Chen, G. Zhou, G. Nie, H. Yan, B. Ding, and Y. Zhao, “A dna nanorobot functions as a cancer therapeutic in response to a molecular trigger in vivo,” *Nature Biotechnology*, vol. 36, pp. 258–264, 3 2018.
- [20] E. Kopperger, J. List, S. Madhira, F. Rothfischer, D. C. Lamb, and F. C. Simmel, “A self-assembled nanoscale robotic arm controlled by electric fields,” *Science*, vol. 359, no. 6373, p. 296, 2018.
- [21] P. Šulc, F. Romano, T. E. Ouldridge, L. Rovigatti, J. P. K. Doye, and A. A. Louis, “Sequence-dependent thermodynamics of a coarse-grained dna model,” *The Journal of Chemical Physics*, vol. 137, no. 13, p. 135101, 2012.
- [22] M. Vogt, M. Langecker, M. Gouder, E. Kopperger, J. List, F. Rothfischer, and F. C. Simmel, “Storing mechanical energy in dna nanorobotics using torsion molecular spring elements.” submitted on 23rd Sep 21 to Nature Physics.
- [23] J. L. Leroy, M. Kochoyan, T. Huynh-Dinh, and M. Guérón, “Characterization of base-pair opening in deoxynucleotide duplexes using catalyzed exchange of the imino proton,” *Journal of Molecular Biology*, vol. 200, pp. 223–238, 3 1988.
- [24] M. Kulkarni and A. Mukherjee, “Understanding b-dna to a-dna transition in the right-handed dna helix: Perspective from a local to global transition,” *Progress in biophysics and molecular biology*, vol. 128, pp. 63–73, 2017.

- [25] J. N. Zadeh, C. D. Steenberg, J. S. Bois, B. R. Wolfe, M. B. Pierce, A. R. Khan, R. M. Dirks, and N. A. Pierce, “Nupack: Analysis and design of nucleic acid systems,” *Journal of Computational Chemistry*, vol. 32, no. 1, pp. 170–173, 2011.
- [26] P. Yakovchuk, E. Protozanova, and M. D. Frank-Kamenetskii, “Base-stacking and base-pairing contributions into thermal stability of the DNA double helix,” *Nucleic Acids Research*, vol. 34, pp. 564–574, 01 2006.
- [27] M. Mosayebi, A. A. Louis, J. P. Doye, and T. E. Ouldridge, “Force-induced rupture of a dna duplex: from fundamentals to force sensors,” *ACS nano*, vol. 9, no. 12, pp. 11993–12003, 2015.
- [28] S. Kufer, E. Puchner, H. Gumpf, T. Liedl, and H. Gaub, “Single-molecule cut-and-paste surface assembly,” *Science*, vol. 319, no. 5863, pp. 594–596, 2008.
- [29] N. C. Seeman, “Nucleic acid junctions and lattices,” *Journal of Theoretical Biology*, vol. 99, pp. 237–247, 1982.
- [30] B. Yurke, A. J. Turberfield, A. P. Mills, F. C. Simmel, and J. L. Neumann, “A dna-fuelled molecular machine made of dna,” *Nature*, vol. 406, no. 6796, pp. 605–608, 2000.
- [31] Y. Guo, B. Wei, S. Xiao, D. Yao, H. Li, H. Xu, T. Song, X. Li, and H. Liang, “Recent advances in molecular machines based on toehold-mediated strand displacement reaction,” *Quantitative Biology*, vol. 5, no. 1, p. 25, 2017.
- [32] D. Y. Zhang and E. Winfree, “Control of dna strand displacement kinetics using toehold exchange,” *Journal of the American Chemical Society*, vol. 131, no. 47, pp. 17303–17314, 2009. PMID: 19894722.
- [33] D. M. J. Lilley, “Structures of helical junctions in nucleic acids,” *Quarterly Reviews of Biophysics*, vol. 33, no. 2, p. 109–159, 2000.
- [34] S. Christian, W. Elena M., E. Wouter, K. Jessica A., S. Ken, L. Anna, K. Fenna, W. Florian, A. S. Ali, P. Ulrike, H. Michael F., F. Seth, and D. Hendrik, “Programmable icosahedral shell system for virus trapping,” *Nature Materials*, vol. 20, pp. 1281–1289, 9 2021.
- [35] C. E. Castro, F. Kilchherr, D.-N. Kim, E. L. Shiao, T. Wauer, P. Wortmann, M. Bathe, and H. Dietz, “A primer to scaffolded dna origami,” *Nature Methods*, vol. 8, pp. 221–229, Mar 2011.
- [36] S. M. Douglas, H. Dietz, T. Liedl, B. Höglberg, F. Graf, and W. M. Shih, “Self-assembly of dna into nanoscale three-dimensional shapes,” *Nature*, vol. 459, pp. 414–418, May 2009.
- [37] T. J. Fu and N. C. Seeman, “Dna double-crossover molecules,” *Biochemistry*, vol. 32, pp. 3211–3220, Apr 1993.

Bibliography

- [38] S. M. Douglas, A. H. Marblestone, S. Teerapittayanon, A. Vazquez, G. M. Church, and W. M. Shih, “Rapid prototyping of 3D DNA-origami shapes with caDNAno,” *Nucleic Acids Research*, vol. 37, pp. 5001–5006, 06 2009.
- [39] H. Tadakuma, T. Masubuchi, and T. Ueda, “Chapter five - rna study using dna nanotechnology,” in *Nanotechnology Tools for the Study of RNA* (S. Yoshizawa, ed.), vol. 139 of *Progress in Molecular Biology and Translational Science*, pp. 121–163, Academic Press, 2016.
- [40] J. C. Wang, “Helical repeat of dna in solution,” *Proceedings of the National Academy of Sciences*, vol. 76, no. 1, pp. 200–203, 1979.
- [41] S. Woo and P. W. K. Rothemund, “Programmable molecular recognition based on the geometry of dna nanostructures,” *Nature Chemistry*, vol. 3, pp. 620–627, 8 2011.
- [42] J.-M. Arbona, J.-P. Aimé, and J. Elezgaray, “Folding of dna origamis,” *Frontiers in Life Science*, vol. 6, no. 1-2, pp. 11–18, 2012.
- [43] K. E. Dunn, F. Dannenberg, T. E. Ouldridge, M. Kwiatkowska, A. J. Turberfield, and J. Bath, “Guiding the folding pathway of dna origami,” *Nature*, vol. 525, pp. 82–86, Sep 2015.
- [44] M. Vogt, E. Kopperger, J. List, M. Langecker, I. Santiago, and F. C. Simmel, “Electrical actuation of a dna-based nanoroboticsystem,” in preparation.
- [45] S. C. Moldoveanu and V. David, “Chapter 1 - basic information about hplc,” in *Essentials in Modern HPLC Separations* (S. C. Moldoveanu and V. David, eds.), pp. 1–51, Elsevier, 2013.
- [46] J. R. Lakowicz, *Principles of Fluorescence Spectroscopy*. Springer US, 2006.
- [47] C. Hübner, A. Renn, I. Renge, and U. Wild, “Direct observation of the triplet lifetime quenching of single dye molecules by molecular oxygen,” *Journal of Chemical Physics*, vol. 115, no. 21, pp. 9619–9622, 2001. cited By 81.
- [48] T. E. Ouldridge, A. A. Louis, and J. P. K. Doye, “Structural, mechanical, and thermodynamic properties of a coarse-grained dna model,” *The Journal of Chemical Physics*, vol. 134, no. 8, p. 085101, 2011.
- [49] T. E. Ouldridge, *Coarse-grained modelling of DNA and DNA self-assembly*. PhD thesis, Oxford University, UK, 2011.
- [50] G. Bussi, D. Donadio, and M. Parrinello, “Canonical sampling through velocity rescaling,” *The Journal of Chemical Physics*, vol. 126, no. 1, p. 014101, 2007.
- [51] “Documentation - oxdna.”
- [52] J. P. K. Doye, H. Fowler, D. Prevsern, J. Bohlin, L. Rovigatti, F. Romano, P. vSulc, C. K. Wong, A. A. Louis, J. S. Schreck, M. C. Engel, M. Matthies, E. Benson, E. Poppleton, and B. E. K. Snodin, “The oxdna coarse-grained model as a tool to simulate dna origami,” 2020.

[53] E. Poppleton, J. Bohlin, M. Matthies, S. Sharma, F. Zhang, and P. Šulc, “Design, optimization and analysis of large dna and rna nanostructures through interactive visualization, editing and molecular simulation,” *Nucleic Acids Research*, vol. 48, pp. e72–e72, 05 2020.

[54] L. Rovigatti, P. Šulc, I. Z. Reguly, and F. Romano, “A comparison between parallelization approaches in molecular dynamics simulations on gpus,” *Journal of Computational Chemistry*, vol. 36, no. 1, pp. 1–8, 2015.

[55] S. Cocco, R. Monasson, and J. F. Marko, “Force and kinetic barriers to unzipping of the dna double helix,” *Proceedings of the National Academy of Sciences*, vol. 98, pp. 8608–8613, 7 2001.

[56] H. E. Gaub, M. Rief, and H. Clausen-Schaumann, “Sequence-dependent mechanics of single dna molecules,” *Nature Structural Biology*, vol. 6, pp. 346–349, 4 1999.

[57] C. Danilowicz, K. Hatch, A. Conover, T. Ducas, R. Gunaratne, V. Coljee, and M. Prentiss, “Study of force induced melting of dsdna as a function of length and conformation,” *Journal of Physics: Condensed Matter*, vol. 22, p. 414106, 10 2010.

[58] N. Srinivas, T. E. Ouldridge, P. Šulc, J. M. Schaeffer, B. Yurke, A. A. Louis, J. P. K. Doye, and E. Winfree, “On the biophysics and kinetics of toehold-mediated DNA strand displacement,” *Nucleic Acids Research*, vol. 41, pp. 10641–10658, 09 2013.

[59] L. Boltzmann, *Studien über das Gleichgewicht der lebendigen Kraft zwischen bewegten materiellen Punkten*, pp. 49–96. 1868.

[60] R. Dickman, F. Manyanga, G. P. Brewood, D. J. Fish, C. A. Fish, C. Summers, M. T. Horne, A. S. Benight, *et al.*, “Thermodynamic contributions of 5'-and 3'-single strand dangling-ends to the stability of short duplex dnas,” *Journal of Biophysical Chemistry*, vol. 3, no. 01, p. 1, 2012.

[61] E. Stahl, T. G. Martin, F. Praetorius, and H. Dietz, “Facile and scalable preparation of pure and dense dna origami solutions,” *Angewandte Chemie International Edition*, vol. 53, no. 47, pp. 12735–12740, 2014.

[62] K. Devanand and J. C. Selser, “Polyethylene oxide does not necessarily aggregate in water,” *Nature*, vol. 343, pp. 739–741, 2 1990.

[63] M. Winger, A. H. de Vries, and W. F. van Gunsteren, “Force-field dependence of the conformational properties of α,ω -dimethoxypolyethylene glycol,” *Molecular Physics*, vol. 107, no. 13, pp. 1313–1321, 2009.

[64] P. Y. Lee, J. Costumbrado, C.-Y. Hsu, and Y. H. Kim, “Agarose gel electrophoresis for the separation of dna fragments,” *Journal of Visualized Experiments*, 4 2012.

[65] D. S. Johnson, J. K. Jaiswal, and S. Simon, “Total internal reflection fluorescence (tirf) microscopy illuminator for improved imaging of cell surface events,” *Current Protocols in Cytometry*, vol. 61, 7 2012.

Bibliography

- [66] D. Axelrod, “Total internal reflection fluorescence microscopy in cell biology,” *Trafic*, vol. 2, pp. 764–774, 11 2001.
- [67] E. Abbe, “Beiträge zur theorie des mikroskops und der mikroskopischen wahrnehmung,” *Archiv für Mikroskopische Anatomie*, vol. 9, pp. 413–468, Dec 1873.
- [68] M. J. Rust, M. Bates, and X. Zhuang, “Sub-diffraction-limit imaging by stochastic optical reconstruction microscopy (STORM),” vol. 3, pp. 793–796, Aug. 2006.
- [69] S. W. Hell, “Toward fluorescence nanoscopy,” vol. 21, pp. 1347–1355, Oct. 2003.
- [70] R. Jungmann, C. Steinhauer, M. Scheible, A. Kuzyk, P. Tinnefeld, and F. C. Simmel, “Single-molecule kinetics and super-resolution microscopy by fluorescence imaging of transient binding on dna origami,” *Nano Letters*, vol. 10, no. 11, pp. 4756–4761, 2010. PMID: 20957983.
- [71] J. Schnitzbauer, M. T. Strauss, T. Schlichthaerle, F. Schueder, and R. Jungmann, “Super-resolution microscopy with dna-paint,” *Nature Protocols*, vol. 12, 2017.
- [72] A. Sharonov and R. M. Hochstrasser, “Wide-field subdiffraction imaging by accumulated binding of diffusing probes,” *Proceedings of the National Academy of Sciences*, vol. 103, 2006.
- [73] S. Strauss and R. Jungmann, “Up to 100-fold speed-up and multiplexing in optimized dna-paint,” *Nature Methods*, vol. 17, 2020.
- [74] C. S. Smith, N. Joseph, B. Rieger, and K. A. Lidke, “Fast, single-molecule localization that achieves theoretically minimum uncertainty,” *Nature methods*, vol. 7, 2010.
- [75] X. Wei, J. Nangreave, S. Jiang, H. Yan, and Y. Liu, “Mapping the thermal behavior of dna origami nanostructures,” *Journal of the American Chemical Society*, vol. 135, no. 16, pp. 6165–6176, 2013. PMID: 23537246.

Acknowledgments

First, I want to thank Prof. Friedrich Simmel for giving me the opportunity to do my master thesis in his group and work on such fascinating projects.

Thank you Prof. Joachim Rädler, for agreeing to become internal supervisor on LMU side and helping me to resolve administrative obstacles.

Thank you Matthias V, Jonathan and Enzo for teaching me the biophysical methods and helping me out in planning and executing the experiments.

Thank you Enzo, for providing the miniCQO that was practically ready to be simulated. Thank you also for the beautiful 3D-renderings that were used in Chapter 3.

Thank you Martin, for introducing me to molecular-dynamics simulations. It was a lot of fun to work together on the wind-up simulations. Thank you also for all the on- and off-topic discussions we had, they were very entertaining.

Thank you Jonathan, for keeping me motivated with visionary ideas when experiments didn't work out as expected. Thank you also for introducing me to the workbench of the lab. That was inspiring for many new projects to come.

Thank you Martin, Jonathan and my father Thomas, for proofreading this thesis and giving me tips to improve my writing skills. Thank you also, for all the support during the stressful last couple of weeks before the deadline of this thesis.

Thank you to every member of this group, Jonathan, Martin, Enzo, Matthias V, Florian and Adrian, for this warm and friendly working-atmosphere. I really appreciate how much freedom you gave me regarding my work, so I could pursue what interested me most. I would also like to thank you for the fun time we had outside of work.

Last but not least, I want to express my sincere thanks to my parents Thomas and Eva for supporting me in every way possible in the course of this master thesis.

Hiermit erkläre ich, die vorliegende Arbeit selbständig verfasst zu haben und keine anderen als die in der Arbeit angegebenen Quellen und Hilfsmittel benutzt zu haben.

München, 25.10.21